Analytical Methods for the Study and Design of Integrated Switched Oscillators and Antennas for Mesoband Radiation

THÈSE N^{O} 5775 (2013)

PRÉSENTÉE LE 21 JUIN 2013

À LA FACULTÉ DES SCIENCES ET TECHNIQUES DE L'INGÉNIEUR
LABORATOIRE DE RÉSEAUX ÉLECTRIQUES
PROGRAMME DOCTORAL EN GÉNIE ÉLECTRIQUE

ÉCOLE POLYTECHNIQUE FÉDÉRALE DE LAUSANNE

POUR L'OBTENTION DU GRADE DE DOCTEUR ÈS SCIENCES

PAR

Jose Felix VEGA STAVRO

acceptée sur proposition du jury:

Prof. M. Paolone, président du jury
Prof. F. Rachidi-Haeri, directeur de thèse
Prof. J. R. Mosig, rapporteur
Prof. M. Rubinstein, rapporteur
Prof. R. Thottappillil, rapporteur

ÉCOLE POLYTECHNIQUE
FÉDÉRALE DE LAUSANNE

Suisse
2013

Résumé

Cette thèse a été réalisée dans le cadre d'un projet de coopération scientifique intitulé “Application of High Power Electromagnetics to Human Safety” développé par l'EPFL, l'Université Nationale de la Colombie et l’Université des Andes, Colombie. Le projet a été financé par l'Agence Suisse pour le Développement et la coopération (SDC) et par le Centre Coopération & Développement (CODEV) de l'EPFL.

La coopération scientifique visait l'étude et le développement des techniques pour la génération de signaux électromagnétiques à haute puissance, capables de perturber ou activer préventivement des engins explosifs improvisés (en anglais IEDs, Improvised Explosive Devices) lors des activités de déminage humanitaire.

Les résultats de la thèse seront appliqués à la construction d'un système rayonnant de type résonant, qui peut être utilisé pour sécuriser des opérations de déminage humanitaire en Colombie.

La thèse est dédiée à l’analyse des oscillateurs à commutation (en anglais, Switched Oscillators – SWO). Un SWO est un système rayonnant constitué par un circuit de charge à haute tension qui alimente un résonateur formé par une ligne de transmission quart d'onde, connecté à une antenne. Un SWO peut produire des champs électromagnétiques de forte amplitude et de courte durée, avec une largeur de bande modérée par rapport à la fréquence de résonance principale.

Les résultats de la thèse peuvent également être utilisés pour la production de champs électromagnétiques résonants de haute puissance dans des applications de compatibilité électromagnétique, avec le but de tester l'immunité des systèmes électroniques contre les interférences électromagnétiques intentionnelles (IEMI).

La thèse est divisée en trois parties. La première partie traite de la conception électrostatique du SWO. Une méthode pour une conception optimisée des électrodes constituant l’éclateur du SWO a été proposée. La méthode est basée sur la génération d'un espace de coordonnées curvilignes dans lequel les électrodes sont conformes à l'un des axes de coordonnées de l'espace. L'équation de Laplace est résolue dans l'espace interelectrodique et une solution analytique pour la distribution électrostatique est obtenue. En utilisant des procédures mathématiques, une expression analytique de l'impédance de la ligne de transmission formée par les électrodes a été développée.

La deuxième partie de la thèse est consacrée à l'analyse des SWO dans le domaine fréquentiel. Une approche originale d'analyse, basée sur la technique de paramètres de chaîne est proposée. Le SWO et l'antenne connectée y sont décrits à l'aide d'un quadripôle, grâce auquel une fonction de transfert entre la tension d'entrée et le champ rayonné est établie. Une expression analytique de la fréquence de résonance du SWO est également obtenue. La technique développée permet d'étudier la réponse d'un SWO lorsqu'il est connecté à une antenne arbitraire avec une impédance d'entrée dépendante de la fréquence.

La dernière partie de la thèse présente la construction et le test d'un prototype de SWO. La conception du prototype est basée sur les développements théoriques présentés dans les deux premières parties de la thèse. Le prototype a été conçu

pour être résonant à 433 MHz, avec une tension d'entrée de 30 kV. Les mesures des champs rayonnés par le prototype indiquent des amplitudes de l’ordre de 10 kV/m à une distance de 1.5 m.

Le prototype est utilisé pour tester la validité du modèle électrodynamique pour l'analyse des SWO. Les champs rayonnés par le SWO connecté à différentes antennes monopoles sont mesurés et comparés avec les calculs théoriques.

Il a été montré que le modèle théorique développé est capable de reproduire avec une bonne précision le comportement du SWO connecté à une antenne en tenant compte de la dépendence fréquentielle de son impédance d’entrée.

Liste de mots-clés:

Champs électromagnétique d’haute puissance, résonateurs, Equation de Laplace dans de coordonnées curvilinéaires, Interférence Electromagnétique Intentionnel (IEMI), systèmes de test de compatibilité électromagnétique.

Abstract

This thesis was carried out within the framework of a scientific cooperation project entitled “Application of High Power Electromagnetics to Human Safety” developed by the EPFL, the National University of Colombia and Los Andes University, Colombia. The project was funded by the Swiss Agency for Development and Cooperation (SDC) through the EPFL Centre Coopération & Développement (CODEV).

The Scientific Cooperation aimed at the study and development of techniques for the generation of high power electromagnetic signals for the disruption or preemptive activation of Improvised Explosive Devices (IEDs) during humanitarian clearance activities.

The results and conclusions of the thesis will be applied to the construction of a resonant radiator, which can be used for securing humanitarian demining operations in Colombia.

The thesis is devoted to the analysis of a specific type of resonant radiators known as Switched Oscillators (SWO). An SWO is a radiator constituted by a high voltage charging circuit that drives a quarter-wave transmission line resonator connected to an antenna. An SWO can produce high-amplitude, short duration, electromagnetic fields, with a moderate bandwidth, when compared to the main resonance frequency.

The outcome of the thesis can be also be used in electromagnetic compatibility applications, for the production of resonant, high power electromagnetic fields, with the aim of testing the immunity of electronic systems against Intentional Electromagnetic Interference (IEMI) attacks.

The thesis is divided in three parts. The first part deals with the electrostatic design of an SWO. A method for producing an optimized design of the electrodes forming the spark gap of the SWO is presented. The method is based on the generation of a curvilinear coordinate space on which the electrodes are conformal to one of the coordinate axis of the space. Laplace equation is solved in the interelectrodic space, obtaining an analytical solution for the electrostatic distribution. Furthermore, using appropriate mathematical manipulations, we derive an analytical expression for the impedance of the transmission line formed by the proposed electrodes.

The second part of the thesis is devoted to the analysis of SWOs in the frequency domain. An original analysis approach, based on the chain-parameter technique, is proposed in which the SWO and the connected antenna are described using a two-port network using which a transfer function between the input voltage and the radiated field is established. A closed form expression of the resonance frequency of the SWO is also obtained. The developed technique makes it possible to study the response of an SWO when connected to an arbitrary antenna with a frequency-dependent input impedance.

The final part of the thesis presents the construction and test of an SWO prototype. The prototype design is based on the theoretical developments presented in the first two parts of the thesis. The realized SWO is experimentally characterized

using different antennas. It is characterized by an input voltage of 30 kV and a resonance frequency of 433 MHz. Radiated electric fields using monopole antennas were in the order of 10 kV/m at a distance of 1.5 m.

The prototype is used for testing the validity of the electrodynamic model for the analysis of SWOs connected to frequency dependent antennas. Different monopole antennas connected to the SWO are considered and the radiated fields are measured and compared with theoretical calculations.

It is shown that the developed theoretical model is able to reproduce with a good accuracy the behavior of the SWO connected to a frequency dependent antenna.

List of Keywords:

High power electromagnetic fields, resonators, Laplace equation in curvilinear coordinates, Intentional electromagnetic interference (IEMI), tests systems for electromagnetic compatibility.

Acknowledgements

I would like to thank Professor Farhad Rachidi, my Thesis advisor, for his scientific guidance and support. A few years back he warmly welcomed me at his laboratory and gave me the opportunity of developing this research project. The time spent at his laboratory helped me to grow as a researcher and taught me many beautiful lessons of life.

I am deeply grateful to my dear colleagues and friends Mr. Nicolas Mora, and Dr. Carlos Romero from EPFL, for the long hours of discussion, arguments and debates on many theoretical and practical aspects of this project. I can't say thank you enough for their tremendous support and help.

Special thanks are due to Mr. Bertrand Daout from Montenna Technology, Switzerland. His valuable advices helped me to improve the design of the system. Thanks are also due to Montenna Technology for providing valuable instrumentation for the measurements.

I appreciate very much the collaboration of Mr. Markus Nyffeler and Mr. Pierre Bertholet from Armasuisse, Switzerland, for supporting this project and providing valuable equipment.

Special thanks are due to Dr. Pierre Zweiacker from EPFL, Switzerland, who assisted me during the first experiments of this thesis.

I would like to thank Mr. André Fattet and Mr. Cédric Mora, from the ISIC mechanical workshop at EPFL, for their valuable collaboration on the realization of the prototype.

Thanks are also due to Dr. Akiyoshi Tatematsu and Dr. Damir Cavka, from the EMC Lab at EPFL, for their valuable and enthusiastic support during the measurements.

I would like to express my sincere thanks to Professor Francisco Roman from National University of Colombia and Professor Nestor Peña, from Los Andes University, Colombia, for their support during the development of this work.

During these four years I have had the pleasure of working with the colleagues of the EMC Group at EPFL Switzerland, thank you very much guys for all the support.

Last but not least, I would like to express my deepest thanks to the supporting organizations of this project: the Swiss Agency for Development and Cooperation (SDC), cooperation@epfl, the Swiss Federal Commission for Scholarships for Foreign Students (FCS), The Cattleya project, and the National University of Colombia.

I dedicate this thesis to Paola, my wife,
who crossed the world (and back) for supporting me,
without her love this project would not have been possible.

Dedicated to my parents, my sister and my brothers,
whose love and guidance made me who I am

Table of Contents

	Résumé	i
	Abstract	iii
	Acknowledgments	v
	Table of contents	ix
	Chapter 1. Introduction	1
1.1.	Thesis framework	2
1.2.	Background	3
1.2.1.	Classification of radiating systems	3
1.2.2.	The switched oscillator	3
1.3.	Research questions	5
1.4.	Outline and original contributions	6
	References	6
	Chapter 2. Electrostatic design of switched oscillators	9
2.1.	Introduction	10
2.2.	Background	11
2.3.	Conditions for optimal electrostatic distribution in a co-axial SWO	11
2.4.	A method for generating a curvilinear coordinate space from conformal transformations	12
2.5.	The inverse prolate spheroidal coordinate system	13
2.6.	Differential operators in curvilinear coordinates	19
2.6.1.	Orthogonal coordinate system	19
2.6.2.	Constant-coordinate curves	20
2.6.3.	Distance along constant-coordinate curves	20
2.6.4.	Differential operators	21
2.7.	Solution of Laplace equation	21
2.8.	Electrostatic field calculation	24
2.9.	Electrostatic simulation	28

2.10.	Limitations of the theoretical model	31
2.11.	Conclusions	37
	References	37
3	**CHAPTER 3. CHARACTERISTIC IMPEDANCE OF THE INVERSE PROLATE SPHEROIDAL - RADIAL TRANSMISSION LINE OF THE SWO**	39
3.1.	Introduction	40
3.2.	Review of the IPS coordinate system	41
3.3.	Impedance of the RTL at the coaxial end	42
3.4.	Electric field distribution	44
3.5.	One-dimensional simplification	46
3.6.	Magnetic field distribution	48
3.7.	Characteristic impedance	50
3.8.	Example	51
3.9.	Conclusions	52
	References	52
4	**CHAPTER 4. ELECTRODYNAMIC ANALYSIS OF A SWITCHED OSCILLATOR CONNECTED TO A FREQUENCY DEPENDENT LOAD**	55
4.1.	Introduction	56
4.2.	Background	56
4.3.	Chain (ABCD) matrix representation of the SWO	58
4.3.1.	ABCD parameters of the coaxial transmission line	59
4.3.2.	ABCD parameters of the RTL	59
4.4.	Voltage transfer function of the SWO	60
4.5.	Eigenfrequencies of the SWO	61
4.6.	Source representation	63
4.7.	Antenna modeling	64
4.8.	Application example	65
4.8.1.	ABCD parameters	65
4.8.2.	Monopole antenna	68
4.8.3.	Energy balance	71
4.8.4.	Radiated field	73

4.9.	Conclusions	75
	References	76
5	**CHAPTER 5. DESIGN, REALIZATION AND EXPERIMENTAL CHARACTERIZATION OF A COAXIAL SWITCHED OSCILLATOR**	77
5.1.	Introduction	78
5.2.	Mechanical design	78
5.3.	Gas type	83
5.4.	Experimental setup	84
5.4.1.	Measurements	85
5.4.2.	Breakdown voltage	85
5.4.3.	Ultem gasket section	86
5.4.3.1.	Monopole antennas	88
5.4.3.2.	Field radiated by antenna I	89
5.5.	Field radiated by antenna II	91
5.6.	Time-frequency analysis of the radiated signal	93
5.7	Conclusions	97
	References	97
	CHAPTER 6. CONCLUSIONS	99
6.1	Electrostatic design of SWOs	100
6.2	Electrodynamic design of SWOs	100
6.3	Application of the proposed design methodology	101
	Appendix 1. A time domain model of the SWO	103
	Singularities introduced by capacitive loads	107
	References	110
	Curriculum vitae	111

CHAPTER 1
INTRODUCTION

1.1. THESIS FRAMEWORK

This thesis was carried out within the framework of a scientific cooperation project entitled “Application of High Power Electromagnetics to Human Safety” involving EPFL, the National University of Colombia and Los Andes University, Colombia. The project was funded by the Swiss Agency for Development and Cooperation (SDC) through the EPFL Centre Coopération & Développement (CODEV) [1] .

The project aimed at the study and development of techniques for the generation of high power electromagnetic signals for the disruption or preemptive activation of Improvised Explosive Devices (IEDs) during humanitarian clearance activities.

IEDs, also known as improvised landmines, produce an increasing number of victims among civilians and militaries in Colombia [2]. Several campaigns of clearance in rural territories have been initiated by the Colombian government, using detection techniques such as metal detectors, dogs and manual detection. These techniques are effective only in part, due to the low metal content of the IEDs.

The approach proposed by the scientific cooperation project can reduce the cost and duration of the demining activities and can increase the safety of the operations.

The project was divided in two main work packages. The first one considered the modeling of the IEDs and its triggering mechanisms as electromagnetic targets susceptible of interference, see for example [3].

The second work package dealt with the design and construction of high power electromagnetic radiators, able to couple electromagnetic energy into the IED, perturbing its normal functioning. The theory and experimental validation for analyzing, studying and optimizing the design of an electromagnetic radiator able to fulfill this task are presented in this thesis.

The results and conclusions of the thesis will be applied to the construction of a resonant radiator, which can be used for securing humanitarian demining operations in Colombia.

The results of the scientific cooperation project can also be applied in a developed country as Switzerland. The EPFL EMC-Laboratory participates in a European project on the evaluation of vulnerabilities of critical infrastructures against Intentional Electromagnetic Interference (IEMI) [4]. The source developed in this thesis will be used in this project as a source of electromagnetic disturbances for system immunity testing.

IEMI attacks are a matter of increasing interests in both, civilian and military contexts. This topic have been the subject of numerous studies sponsored by governmental institutions of several countries (e.g. [5, 6]). International organisms such as URSI [7], and IEC [8] recognize IEMI as a risk for the civilian society.

The effects of IEMI on electronic systems depend on the level of voltages and currents coupled into the system: they can range from noise coupling causing malfunctioning, to physical destruction of the components of the system.

The validation of studies on the effects of radiated IEMI on systems and the test of the relevant countermeasures require the use of high power electromagnetic radiators, capable of producing high power illuminating fields. The amplitude, bandwidth and beam width of the fields are determined by the type of the required tests.

1.2. BACKGROUND

1.2.1. Classification of radiating systems

Giri [9] proposed a classification of radiating systems based on the percent bandwidth (*pbw*) and the bandratio (*br*) of the radiated signal, defined respectively as

$$pbw = \frac{2(f_h - f_l)}{f_h + f_l} 100\% \tag{1.1}$$

$$br = \frac{f_h}{f_l} \tag{1.2}$$

where f_l and f_h are the cut-off frequencies of the spectrum of the radiated signal, defined as the limits of the band containing the 90% of the radiated energy [9, 10].

Table I shows the classification of the radiating systems based on the values *pbw* and *br* [9].

Table I. Definitions for bandwidth classification.

Band type	Percent bandwidth (*pbw*)	Bandratio (*br*)
Hypoband or Narrowband	< 1%	<1.010
Mesoband	1% < *pbw* ≤100%	1.010 < *br* ≤3
Sub-hyperband	100%<*pbw*≤163.4%	3 < *br* ≤10
Hyperband	163.4%<*pbw*≤200%	*br* >10

High power sub-hyperband and hyperband fields, for instance, are required when the susceptibility of the Device Under Test (DUT) or target is tested over a large frequency band. On the other hand, resonant or mesoband sources are required when the DUT is tested at a higher level of signal at a particular frequency. A more specific classification of the radiators was established in [11].

1.2.2.The Switched Oscillator

In this study, we investigate a type of mesoband radiator called Switched Oscillator (SWO), proposed by Carl Baum in 2000 [12]. An SWO consists of a low-impedance transmission line initially charged at high voltage and connected to a high-impedance antenna at one end. The other end of the transmission line is connected to a self-breaking gas switch that short-circuits the line once the breakdown threshold is reached. The equivalent circuit representing an SWO system is presented in Figure 1.

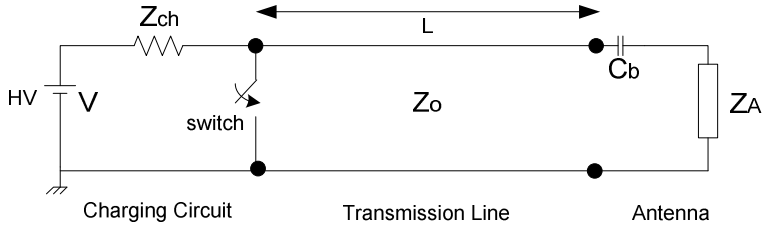

Figure 1.1 Schematic representation of a Switched Oscillator (SWO). A low impedance (Zo) charged line is short-circuited at one end and discharged on a high impedance antenna (Z_A). The line is charged through a high impedance element Z_{ch}, preventing the interaction of the impulse and the charging source (HV). Eventually a blocking capacitor C_b is used in order to prevent DC charges on the antenna.

The closing of the switch produces a fast transient that propagates through the line and reaches the antenna. Due to the mismatch between the antenna and the transmission line, only part of this signal is radiated. The rest of the pulse is reflected and propagates back to the switch. If we assume that the switch is still closed when the reflected wave arrives, a second reflection with inversed sign will be sent back towards the antenna.

At the terminals of the antenna this will appear as a series of pulses, of positive and negative amplitudes and with a decreasing magnitude, separated by a time delay corresponding to the round trip time of the transmission line. Thus, it can be said that the SWO is a quarter-wave oscillator, with a fundamental frequency (f_o) given by:

$$f_0 = \frac{v_p}{4L} \tag{1.3}$$

where: v_p is the wave propagation velocity and L is the length of the line.

The idea presented by Baum in his seminal publication is appealing due to its simplicity and feasibility by using existing technology from ultrawideband applications. Several successful implementations of this concept have been reported in the past years. In [13], Baum proposed the construction of a coaxial SWO connected to a Half Impulse Radiating Antenna (HIRA). The construction of a similar system, called the MATRIX was reported in [14]. The coaxial structure forming the MATRIX was pressurized with hydrogen at 110 bars, permitting a charging

voltage of 300 kV. The reported resonance frequency of this system was 180 MHz. Giri [15] presented the design and operation of SWOs connected to helical antennas. Two different coaxial SWOs, pressurized with Nitrogen at 40 bars and operating at 200 MHz and 500 MHz with a charging voltage of 30 kV were reported. In [16], Armanious et. al. presented the design of a coaxial SWO with variable resonance frequency. This SWO was connected to a conical antenna and its reported central frequency was about 1.5 GHz. Santamaría *et al*. proposed in [17] a study on the influence of the parameters of the SWO on the produced signal.

In parallel with these contributions and reports on practical implementations, several theoretical aspects of the SWO have been considered. In [18], Baum presented the concept of differential SWO. In [15], Giri proposed to model the coaxial SWO as a cascade of two transmission lines: a radial transmission line (RTL), formed by the electrodes of the switch, followed by a second transmission line corresponding to the main body of the coaxial line. The RTL has a non-uniform impedance affecting the nominal resonance frequency and the quality factor (Q) of the SWO. The measured resonance frequency of the radiated wave corresponds to a length L that appears to be longer than the actual physical length of the SWO. This has been clearly demonstrated in [19]. In order to accurately estimate the resulting resonance frequency and quality factor of the SWO, different numerical methods have been used (e.g. [15]). However, to the best of the author's knowledge, no closed-form expressions have been derived for this purpose.

Another important theoretical aspect is the design of the electrodes of the SWO. Armanious et. al. presented in [19] an iterative method for the design of electrodes that results in a given distribution of the electric field. The design methodology reduces the effects of the non-uniformities of the RTL on the Q of the radiated signal.

1.3. RESEARCH QUESTIONS

Despite all the efforts mentioned in the previous section, there are still some open questions that deserve to be addressed.

The first one of these questions deals with the electrostatic design of the SWO. Presently, the profile of the electrodes is generated either using some trial and error scheme or using an iterative method, as the one proposed in [19]. In both cases, electrostatic simulations are needed in order to validate the obtained solution. Although a single electrostatic simulation is not an issue in terms of computational effort, the actual process of the development of an SWO requires several simulations in order to test intermediate solutions and alternatives. This process can be extremely simplified if the electrodes are generated using a pre-defined profile with a known, analytical electrostatic field distribution. Naturally, the produced electrostatic distribution should fulfill some constraints, such as the field amplitude should be maximum at the spot where the discharge is desired to occur.

As discussed in [15], the variation of the impedance along the RTL results in a shift on the expected resonance frequency of the SWO. However, this influence can only be estimated by numerically solving the system formed by the RTL and the connected coaxial line. The second open challenge consists in finding a closed

form expression relating the parameters of the radial transmission line to the resonance frequency of the SWO. This question is related to the previous one, in the sense that an analytical expression for the characteristic impedance of the RTL can be obtained from the electrostatic field distribution. The solution of this question will also result in an improvement on the design process of SWOs.

The third open question is related to the integration of frequency dependent antennas to SWOs. Existing publications consider the response of SWOs connected to HIRAs, discones or helical antennas, which have nearly constant impedance over a considerable bandwidth. Therefore, the development of a technique allowing the analysis of the response of an SWO connected to an antenna with arbitrary frequency response for its input impedance would be of great interest.

The aim of this thesis is to address these three questions.

1.4. OUTLINE AND ORIGINAL CONTRIBUTIONS

This work is organized as follows.

Chapter 2 considers the electrostatic design of the SWO, corresponding to the first of the stated questions. In this chapter, the design of a new profile for the electrodes of SWOs is derived. The adopted approach to solve this problem consists in generating the shape of the electrodes conformal to the axis of a curvilinear orthogonal space of coordinates. The profiles of the electrodes are based on the Inverse of Prolate Spheroid (IPS) coordinate system, derived from a conformal transformation proposed by Moon and Spencer in [20]. The Laplace equation is solved in this space and an analytical expression for the electrostatic field distribution is obtained. Numerical simulations confirming the analytical solutions are also presented in this same chapter.

In Chapter 3, the results of the solution of the Laplace equation, obtained in Chapter II, are applied to the derivation of an analytical expression for the impedance of the radial transmission line formed by the IPS electrodes.

Chapter 4 addresses questions 2 and 3 and presents the electrodynamic analysis of SWOs in the frequency domain. A novel analysis, based on the chain-parameter technique, permitting the extraction of the resonance frequency of an SWO is presented. This technique describes the SWO and the connected antenna using a two-port network from which a transfer function between the input voltage and the radiated field is established. A closed form expression of the resonance frequency of the SWO is also obtained. The developed technique makes it possible to study the response of an SWO when connected to an arbitrary antenna with a frequency dependent input impedance.

Chapter 5 reports on the design of an SWO prototype using the proposed IPS profile. The realized SWO is experimentally characterized when connected to a frequency dependent antenna. The intended frequency of operation is f_0=433 MHz, which corresponds to one of the open Industrial Scientific and Medical bands. Measurements of signals radiated by the prototype are presented and discussed.

Finally, Chapter 6 presents the general conclusions of the work, as well as an outlook for future studies.

REFERENCES

[1] F. Rachidi, *et al.*, "Application of high power electromagnetics to human safety. ," ed. Lausanne, Switzerland / Bogotá, Colombia: Swiss Agency for Development and Cooperation (SDC) 2009.

[2] (2013). *Situación Víctimas de Minas Antipersonal en Colombia*. Available: http://www.accioncontraminas.gov.co/Situacion/Paginas/SituacionVictimasMinasAntipersonal.aspx

[3] J. J. Pantoja, *et al.*, "On the Electromagnetic Susceptibility of Hot Wire-Based Electroexplosive Devices to RF Sources," *Electromagnetic Compatibility, IEEE Transactions on*, vol. PP, pp. 1-10, 2012.

[4] A. Bonsignore, *et al.*, "STRUCTURES, Strategies for The impRovement of critical infrastrUCTUres Resilience to Electromagnetic attackS ", ed. Rome: FP 7 Program, 2012.

[5] W. A. Radasky and E. Savage, "Intentional Electromagnetic Interference (IEMI) and Its Impact on the U.S. Power Grid (Meta-R-323),," Metatech Corporation for Oak Ridge National Laboratory, Goleta, California2012.

[6] Lugrin G, *et al.*, "Impact of intentional electromagnetic interference on electric power systems," Electromagnetic Compatibility Laboratory, Swiss Federal Institute of Technology (EPFL), Lausanne, Switzerland2012.

[7] "URSI Resolution of criminal activities using electromagnetic tools," in *International Radio Scientific Union, General Assembly, Toronto, Canada*, 1999.

[8] IEC, "61000-4-35. Electromagnetic compatibility (EMC) " in *Part 1-5: General –High power electromagnetic (HPEM) effects on civil systems Reference*, ed, 2004.

[9] D. Giri and F. M. Tesche, "Classification of Intentional Electromagnetic Enviroments," *IEEE, Transactions on electromagnetic compatibility*, vol. 46, p. 7, 2004.

[10] W. A. Radasky and D. Giri, "The standardization of uwb waveform characteristics by the International electrotechnical commission," presented at the URSI General Assembly, 2005.

[11] D. V. Giri and F. M. Tesche, "Classification of intentional electromagnetic environments (IEME)," *Electromagnetic Compatibility, IEEE Transactions on*, vol. 46, pp. 322-328, 2004.

[12] Baum.C.E, "Switched Oscillators," *Circuit and Electromagnetic System Design Notes*, vol. 45, pp. -, September 2000.

[13] Baum.C.E, "The Dispatcher: A New Mesoband High Power Radiator," *URSI General Assembly 2002*, pp. -, 2002.

[14] J. W. Burger, *et al.*, "Modular Low Frequency High Power Microwave Generator," presented at the AMEREM, Annapolis M.D, USA, 2002.

[15] D. V. Giri, *et al.*, "Switched Oscillators and Their Integration Into Helical Antennas," *Plasma Science, IEEE Transactions on*, vol. 38, pp. 1411-1426, 2010.

[16] M. Armanious, *et al.*, "Interaction Between Geometric Parameters and Output Waveforms in High-Power Quarter-Wave Oscillators," *Plasma Science, IEEE Transactions on*, vol. 38, pp. 1124-1131, 2010.

[17] F. Santamaria, *et al.*, "Switched Oscillator: Parameter Effects on the Generated Signals," *Plasma Science, IEEE Transactions on*, vol. 40, pp. 3433-3441, 2012.

[18] Baum.C.E, "Differential Switched Oscillators and Associated Antennas," *Sensor and Simulation Notes*, vol. 457, pp. -, June 2001.

[19] M. Armanious, *et al.*, "Electrostatic field management and electrodynamic modeling of switched quarter-wave oscillators," *Dielectrics and Electrical Insulation, IEEE Transactions on*, vol. 18, pp. 1054-1065, 2011.

[20] P. Moon and D. E. Spencer, *Field Theory Handbook: Including Coordinate Systems, Differential Equations and Their Solutions* 2ed.: Springer-Verlag, 1971.

CHAPTER 2

ELECTROSTATIC DESIGN OF SWITCHED OSCILLATORS

2.1. INTRODUCTION

The overall geometry of a coaxial SWO is depicted in Figure 2.1. As described in the introduction, the SWO is composed of a charged transmission line (coaxial in this case) connected to a higher impedance antenna at one end and to a closing, self-breaking switch gas at the opposite end.

The electrodes of the spark gap form a radial transmission line (RTL) that progressively becomes coaxial.

As it can be inferred from the figure, on the axis of symmetry the electric field in the gap is parallel to the *z* axis, whereas in the coaxial region it points in the direction of the coordinate *r*. The electrostatic field distribution of the structure (previous to the discharge) should guarantee the occurrence of a fast discharge between the electrodes, on the symmetry axis of the SWO. The geometry of the electrodes must maximize the electric field at the discharge point and prevent field enhancements or distortions that could lead to the occurrence of unwanted discharges in other points of the geometry.

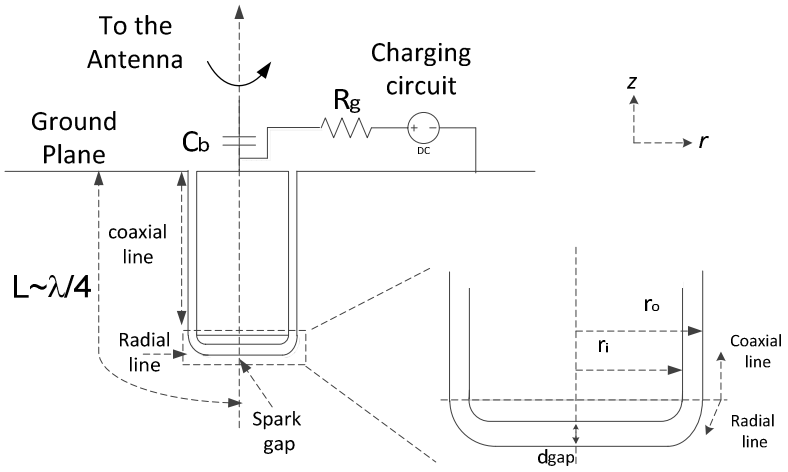

Figure 2.1 Quarter wave coaxial switched oscillator (SWO). Notice the presence of the RTL at the low impedance end of the SWO. Any type of antenna can be connected to the SWO. The one showed here is only for illustrative purposes.

We propose in this chapter a new profile for the electrodes forming the RTL of the SWO. The profile is formed using a curvilinear orthogonal space, generated from a 2-D transformation, called Inverse Prolate Spheroid (IPS), proposed by Moon and Spencer in [1] (page 115).

The advantage of using the IPS profile is that it ensures that the maximum amplitude of the electric field occurs on the axis of symmetry, while the field intensity decreases as we move away from the discharge point towards the coaxial transmission line.

On the other hand, the Laplace Equation is *r*-separable in this coordinate system. This implies that an analytical expression for the electrostatic potential can be derived from which a closed form solution for the electrostatic field can be calculated.

2.2. BACKGROUND

Assuming isotropic and time invariant conditions, the electrostatic field distribution between the electrodes of a gas spark gap depends mainly on the shape of the metallic surface of the electrodes. The occurrence of dielectric breakdown depends on many factors such as gas density, distance between the electrodes and electric field intensity. An optimal choice on the profile of the electrodes permits, for example, to control the occurrence of field enhancements in specific regions.

The design of electrodes for spark gaps used in applications such as Marx generators and Ultra Wide Band (UWB) pulsers rely mostly on the profiles proposed by Rogowski [2], Ernst [3] and Bruce [4], which are intended to produce an uniform field distribution in a defined volume of the interelectrodic space. These profiles improve the repeatability of the discharge and distribute the point of origin of the arc homogeneously on the surface of the electrodes, assuring a uniform wearing of the metallic surface. In general, in such applications the size of the electrodes is much smaller than the smallest wavelength of the discharge pulse; therefore, propagation effects can be neglected.

In the case of a coaxial SWO, the situation is quite different. In order to prevent distortion of the signal transmitted to the antenna, the discharge should be produced on the axis of symmetry of the SWO so that all the points on the wavefront originated at the discharge point would get simultaneously to the antenna.

The problem of the distribution of the electrostatic field in an SWO has been discussed by Giri et al. in [5]. A more detailed discussion and a design technique was proposed by Armanious et al. in [6], where an iterative method, based on the equivalent charge distribution principle, permitted the generation of two exponential profiles forming the electrodes. The formed geometry produces an electric field that is maximum on the axis of symmetry. However, the resulting electric field is not monotonically decreasing as we move away from the axis.

In [7], an equation was proposed for the generation of a new set of electrodes producing an electric field which is maximum on the axis of symmetry and monotonically decreasing along the RTL. However, the proposed approach did not make it possible to obtain an analytical expression for the field between the electrodes, as we intent to do in the present chapter.

2.3. CONDITIONS FOR OPTIMAL ELECTROSTATIC DISTRIBUTION IN A COAXIAL SWO

The probability of producing breakdown on the axis of symmetry maximizes if the magnitude of the electrostatic field at the time of occurrence of the discharge is maximum on the axis of symmetry of the SWO, between the electrodes. We could

summarize the conditions necessary to produce the desired field distribution as follows:

i) The distance between the electrodes should be minimum at the axis of symmetry.
ii) The distance between the electrodes should monotonically increase as we move towards the coaxial line.
iii) The profile of the electrodes as well as its first space derivative should be continuous.

On the other hand, the profile of the electrodes must fulfill the geometric constraints of the design, which are the interlectrodic distance at the axis (d_{gap}) and the cross section of the coaxial transmission line r_i, r_o (as defined in Figure 2.1). This can be included in the analysis as two additional conditions:

iv) The distance between the electrodes at the axis of symmetry should be d_{gap}
v) The distance between the electrodes at the junction with the coaxial line should be $\Delta r = r_o - r_i$, coinciding with the dimensions of the coaxial transmission line.

A set of curves fulfilling these conditions can be formed using an orthogonal curvilinear space, based on the conformal Inverse Prolate Spheroid (IPS) transformation proposed by Moon and Spencer in [1].

The electrodes are generated by two parallel surfaces, conformal to one of the axis of the curvilinear coordinates. This idea is analogous to the one used by Rogowski in [2], with the difference that he used the Maxwell transformation instead.

2.4. A METHOD FOR GENERATING A CURVILINEAR COORDINATE SPACE FROM CONFORMAL TRANSFORMATIONS

The method of generating a curvilinear space starting from a conformal transformation was proposed by Moon and Spencer in [8]. They started by performing a conformal transformation from the W to the Z plane. The orthogonal curved lines produced on the Z plane can be regarded as a 2-D curvilinear coordinate system, which can be either translated or rotated, in order to generate a 3-D coordinate system. The procedure can be summarized as follows:

The transformation from the W to the Z complex planes is;

$$Z = f(W) \tag{2.1}$$

where:

f is an analytical function, W and Z are complex planes:

$$\begin{aligned} W &= u + iv \\ Z &= x + iy \end{aligned} \tag{2.2}$$

As the angles are preserved by the transformation, the function *f* maps the rectangular grid defined by the lines *u=const* and *v=const* in the *W* plane, into an orthogonal curvilinear grid in the *Z* plane.

The parametric form of this new set of orthogonal curves can be obtained from the real and imaginary parts of Equation (2.1) as:

$$\begin{aligned} x &= f_1(u,v) = \mathrm{Re}[\, f(W)] \\ y &= f_2(u,v) = \mathrm{Im}[\, f(W)] \end{aligned} \tag{2.3}$$

The resulting curvilinear grid can be used to generate a new coordinate systems. For example, if the *Z* plane is extruded in a perpendicular direction, a cylindrical coordinate system (*u, v, w*) can be obtained, where the relationship with the Cartesian coordinates is:

$$\begin{aligned} x &= f_1(u,v) \\ y &= f_2(u,v) \\ z &= w \end{aligned} \tag{2.4}$$

If, on the other hand, the *Z* map is rotated around the original *y* axis, we obtain a rotational coordinate system (*u, v, w*). The new relationships with the Cartesian coordinates will be given by:

$$\begin{aligned} x &= f_1(u,v)sin(w) \\ y &= f_1(u,v)cos(w) \\ z &= f_2(u,v) \end{aligned} \tag{2.5}$$

A similar procedure can be applied if the map is rotated around the *x* axis.

2.5. THE INVERSE PROLATE SPHEROIDAL COORDINATE SYSTEM

The Inverse Prolate Spheroidal (IPS) coordinate system is generated by rotating the IPS transformation around one of the axis of the *Z* space. The procedure is as follows.

The starting point is the IPS conformal transformation (also called inverse ellipse transformation) defined as:

$$Z = a\ \mathrm{sech}(W) \tag{2.6}$$

where *sech*( ) is the hyperbolic secant, and:

$$W = u + iv$$
$$Z = x' + iy' \tag{2.7}$$

$a>0$ is a constant,

(x', y') are auxiliary variables (and not the final x, y coordinates of the Cartesian space) and (u,v) are defined in the range:

$$0 \le u < +\infty$$
$$0 \le v \le \pi \tag{2.8}$$

The IPS name comes from the fact that the IPS is the multiplicative inverse of the transformation $Z=cosh(W)$, which represents a prolate spheroid.

The real and imaginary parts of Equation (2.6) can be separated and the space coordinates can be calculated in terms of u, v and a:

$$x' = a\frac{\cosh(u)\cos(u)}{\cosh^2(u) - \sin^2(v)} \tag{2.9}$$

$$y' = a\frac{\sinh(u)\sin(v)}{\cosh^2(u) - \sin^2(v)} \tag{2.10}$$

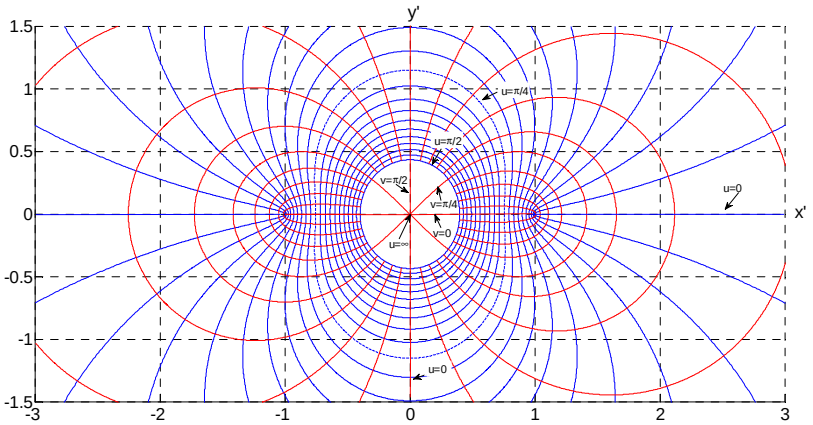

Figure 2.2 Inverse Prolate Spheroid (IPS) map in the *(x', y')* plane. The parametric family of curves in red corresponds to the *v-set*. The *u-set* is represented in blue. For the example here presented a=1.

Equations (2.9) and (2.10) form two sets of orthogonal, parametric curves on the *(x', y')* plane. If *u=constant*, the curves on the (x', y') plane are inverted prolate spheroids. When v is held constant, the curves on the (x', y') form inverted double sheet hyperboloids. The set of curves when *u=constant* is called here the *u-set*. Consequently, we call *v*-set the set of curves when *v=constant*. Figure 2.2 shows the base transformation.

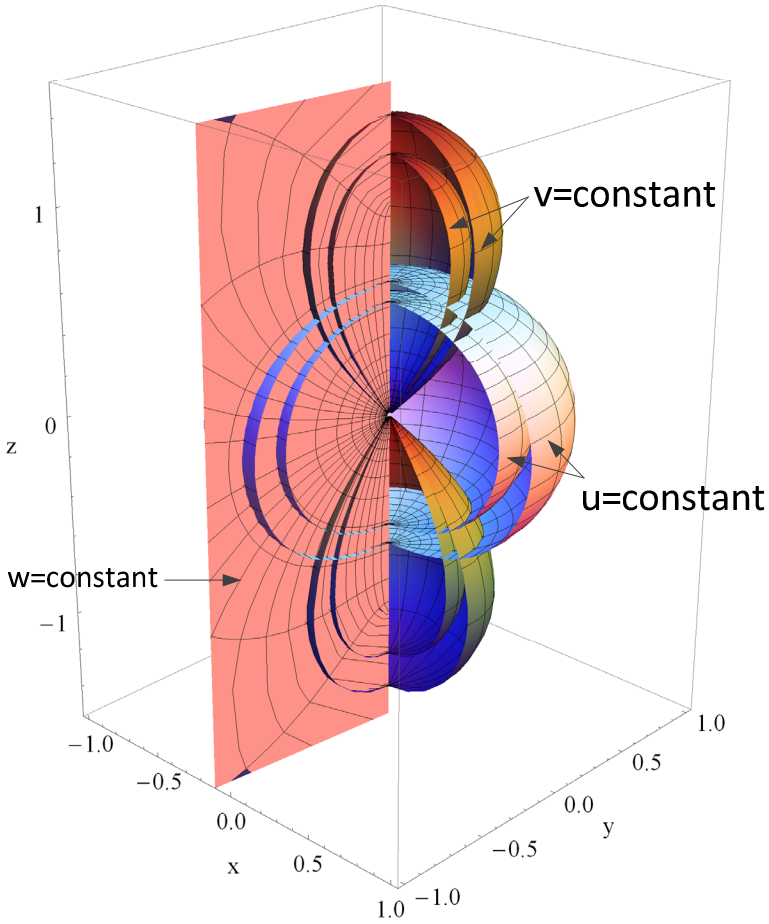

Figure 2.3 Constant surfaces in the Inverse Prolate Spheroidal coordinate system. The surfaces were generated with parameter a=1. Notice the surfaces corresponding to *u-set* and *v-set*.

The 3D curvilinear system (u, v, w) can be generated by rotating the (x', y') plane around the x' axis. Applying Equation (2.5) to Equations (2.9) and (2.10), we can find the relationships between (u, v, w) and (x, y, z), the coordinates of the Cartesian space:

$$x = a\frac{\sinh(u)\sin(v)\cos(w)}{\cosh^2(u)-\sin^2(v)} \quad y = a\frac{\sinh(u)\sin(v)\sin(w)}{\cosh^2(u)-\sin^2(v)} \quad z = a\frac{\cosh(u)\cos(v)}{\cosh^2(u)-\sin^2(v)} \tag{2.11}$$

where the range of (u, v, w) is defined as:

$$\begin{aligned} 0 \le u < +\infty \\ 0 \le v \le \pi \\ 0 \le w \le 2\pi \end{aligned} \tag{2.12}$$

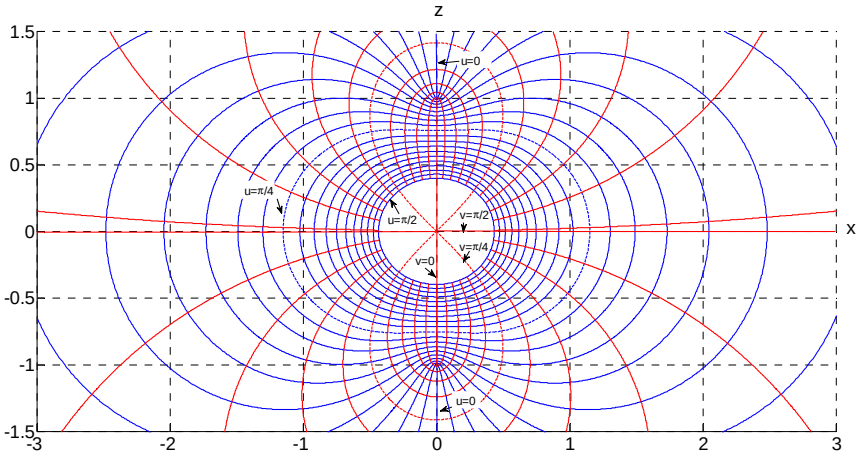

Figure 2.4 2D cut of the IPS coordinates at *w=0*. The *u-set* is colored in blue, the *v-set* is colored in red, for the case of this example *a=1*. The electrodes can be formed by rotating two curves belonging to bottom half of the *u-set* around the *z* axis. In order to respect the geometric constraints of the problem, the distance of the curves at the axis *x=0* should be d_{gap}. The intersection of the surfaces with the axis *z=0*, should correspond to the radii of the coaxial line r_o, r_i.

A 3D representation of the curvilinear system is shown in Figure 2.3. It can be seen that the surface *u=constant* forms an inverted prolate spheroid of revolution, while the surface *v=constant* forms an inverted double sheet hyperboloid of revolution and the surface *w=constant* forms a plane.

Figure 2.4 presents a 2-D cut of the IPS coordinate system, obtained at *w=0*. The figure suggests that the distance between the curves belonging to the *u-set* is minimum at the axis of symmetry, and maximum at the horizontal axis.

We propose to form the electrodes of the SWO taking a pair of surfaces belonging to the bottom half of the *u-set*, defined between v=0, v=π/2. The coaxial line section can be connected at the extremities of the curves (which corresponds to the horizontal plane z=0).

By doing so, the isopotential lines will be conformal to the *u-set*, and the electric field lines will be conformal to the *v-lines*. Notice that the direction of the electric field will be smoothly changed from its vertical *(z)* direction on the axis of symmetry to a radial direction at plane *z=0*, coinciding with the electric field distribution within the coaxial line.

The surface of the outer and inner electrodes, connected to the outer and inner conductors of the coaxial, are defined by the constants u_2 and u_1 respectively.

The internal and external surfaces, called here surfaces u_1 and u_2 respectively, are defined by the following parametric expression:

$$\begin{pmatrix} x_1 \\ y_1 \\ z_1 \end{pmatrix} = \begin{pmatrix} a\dfrac{\sinh(u_1)\sin(v)\cos(w)}{\cosh^2(u_1)-\sin^2(v)} \\ a\dfrac{\sinh(u_1)\sin(v)\sin(w)}{\cosh^2(u_1)-\sin^2(v)} \\ a\dfrac{\cosh(u_1)\cos(v)}{\cosh^2(u_1)-\sin^2(v)} \end{pmatrix} \qquad \begin{pmatrix} x_2 \\ y_2 \\ z_2 \end{pmatrix} = \begin{pmatrix} a\dfrac{\sinh(u_2)\sin(v)\cos(w)}{\cosh^2(u_2)-\sin^2(v)} \\ a\dfrac{\sinh(u_2)\sin(v)\sin(w)}{\cosh^2(u_2)-\sin^2(v)} \\ a\dfrac{\cosh(u_2)\cos(v)}{\cosh^2(u_2)-\sin^2(v)} \end{pmatrix} \tag{2.13}$$

where:

$$\frac{\pi}{2} \le v \le \frac{3\pi}{2}$$
$$0 \le w \le 2\pi$$

The constants u_1, u_2 and the scaling parameter a are calculated taking into account the conditions *iv* and *v* defined in Section 2.3.

Condition *iv* specifies that at the axis of symmetry ($v=0$) the absolute distance between the curves must correspond to the gap distance (d_{gap}).

At the axis of symmetry $v=0$, we have:

$$\begin{pmatrix} x_1 \\ y_1 \\ z_1 \end{pmatrix} = \begin{pmatrix} 0 \\ 0 \\ \dfrac{a}{\cosh(u_1)} \end{pmatrix} \qquad \begin{pmatrix} x_2 \\ y_2 \\ z_2 \end{pmatrix} = \begin{pmatrix} 0 \\ 0 \\ \dfrac{a}{\cosh(u_2)} \end{pmatrix} \tag{2.14}$$

Therefore:

$$d_{gap} = \frac{a}{\cosh(u_2)} - \frac{a}{\cosh(u_1)} \tag{2.15}$$

Condition *v* specifies that at the horizontal plane ($v= \pi/2$), the radial distance between the curves u_1, u_2 and the axis of symmetry must be equal to the coaxial line inner and outer radii r_i, r_o, respectively.

$$\begin{pmatrix} x_1 \\ y_1 \\ z_1 \end{pmatrix} = \begin{pmatrix} \frac{a}{\sinh(u_1)} \\ 0 \\ 0 \end{pmatrix} \qquad \begin{pmatrix} x_2 \\ y_2 \\ z_2 \end{pmatrix} = \begin{pmatrix} \frac{a}{\sinh(u_2)} \\ 0 \\ 0 \end{pmatrix} \tag{2.16}$$

Therefore:

$$x_1 = r_i = a \ \operatorname{csch}(u_1) \tag{2.17}$$

$$x_2 = r_o = a \ \operatorname{csch}(u_2) \tag{2.18}$$

Equation (2.15) can be rearranged as:

$$d_{gap} = \frac{a}{\cosh\left(arc\operatorname{csch}\left(\frac{r_o}{a}\right)\right)} - \frac{a}{\cosh\left(arc\operatorname{csch}\left(\frac{r_i}{a}\right)\right)} \tag{2.19}$$

leading to:

$$\frac{a}{\sqrt{1+\frac{a^2}{r_o^2}}} - \frac{a}{\sqrt{1+\frac{a^2}{r_i^2}}} = d_{gap} \tag{2.20}$$

The constant a, obtained from this equation can be replaced in equations (2.17), (2.18) and the values u_1, u_2 can be calculated.

We present as an example the design of the electrodes of an SWO. This geometry will also be used in the following chapters. The experimental part of the present work, presented in Chapter 5 is based on this design.

The inter-electrodic space of the SWO is d_{gap}=0.5 mm and the dimensions of the coaxial transmission line are r_o =16.5 mm and r_i=17.5 mm, which correspond to an impedance of the coaxial line Z_{coax}=3.5 Ω.

The constants defining the profiles are:

$$u_1 = 1.10507, u_2 = 1.05837, a = 22.1783e-3$$

The resulting geometry is shown in Figure 2.5.

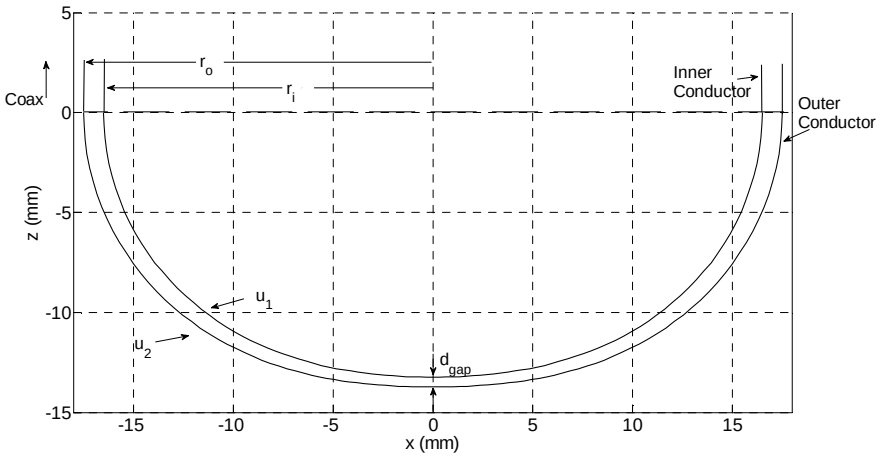

Figure 2.5 Profile of the electrodes proposed as example

2.6. DIFFERENTIAL OPERATORS IN CURVILINEAR COORDINATES

The solution of the Laplace equation in the IPS system will be derived in order to obtain the potential distribution between the electrodes, from which the electric field will be determined. It is therefore necessary to introduce the differential operators in arbitrary curvilinear coordinates. We borrow here the notation and procedure used by Moon and Spencer in [1]. Similar approaches, with different notations, can be found in [9].

2.6.1. ORTHOGONAL COORDINATE SYSTEM

A set of orthogonal curvilinear coordinates (u, v, w), can be defined based on the Cartesian coordinate system by the relationship:

$$\begin{aligned} x &= f_1(u,v,w) \\ y &= f_2(u,v,w) \\ z &= f_3(u,v,w) \end{aligned} \tag{2.21}$$

The metric coefficients (g_{ii}) of the coordinate system are defined by:

$$\begin{aligned} g_{11} &= \left(\frac{\partial x}{\partial u}\right)^2 + \left(\frac{\partial y}{\partial u}\right)^2 + \left(\frac{\partial z}{\partial u}\right)^2 \\ g_{22} &= \left(\frac{\partial x}{\partial v}\right)^2 + \left(\frac{\partial y}{\partial v}\right)^2 + \left(\frac{\partial z}{\partial v}\right)^2 \\ g_{33} &= \left(\frac{\partial x}{\partial w}\right)^2 + \left(\frac{\partial y}{\partial w}\right)^2 + \left(\frac{\partial z}{\partial w}\right)^2 \end{aligned} \tag{2.22}$$

In a rotational coordinate system the metric coefficients are of the form [8]:

$$g_{11}(u_1,u_2) = g_{22}(u_1,u_2)$$
$$g_{33} = g_{33}(u_1,u_2) \tag{2.23}$$

2.6.2.CONSTANT-COORDINATE CURVES

Curves of constant coordinates are formed when two of the three components of the coordinate space are held constant and the third component is considered as a variable parameter. In this work, we call these curves C_u , C_v , C_w as follows:

$$C_u(u,k_1,k_2) = \begin{cases} x = f_1(u,k_1,k_2) \\ y = f_2(u,k_1,k_2) \\ z = f_3(u,k_1,k_2) \end{cases} \tag{2.24}$$

$$C_v(k_1,v,k_2) = \begin{cases} x = f_1(k_1,v,k_2) \\ y = f_2(k_1,v,k_2) \\ z = f_3(k_1,v,k_2) \end{cases} \tag{2.25}$$

$$C_w(k_1,k_2,w) = \begin{cases} x = f_1(k_1,k_2,w) \\ y = f_2(k_1,k_2,w) \\ z = f_3(k_1,k_2,w) \end{cases} \tag{2.26}$$

Notice that if the system has rotational symmetry, the curve C_w corresponds to a circle.

2.6.3.DISTANCE ALONG CONSTANT-COORDINATE CURVES

The infinitesimal length element (dl) of a curve can be expressed as:

$$dl = \sqrt{g_{11}du^2 + g_{22}dv^2 + g_{33}dw^2} \tag{2.27}$$

The infinitesimal lengths of constant-coordinate curves (C_u , C_v , C_w) are, respectively:

$$\begin{aligned} dl_u &= \sqrt{g_{11}}du \\ dl_v &= \sqrt{g_{22}}dv \\ dl_w &= \sqrt{g_{33}}dw \end{aligned} \tag{2.28}$$

Consequently, the distance between two points (p_1, p_2) along C_u , C_v , or C_w can be calculated as:

$$R_u[u_1,u_2]=\int_{u_1}^{u_2}\sqrt{g_{11}}du \tag{2.29}$$

$$R_v[v_1,v_2]=\int_{v_1}^{v_2}\sqrt{g_{22}}dv \tag{2.30}$$

$$R_v[w_1,w_2]=\int_{w_1}^{w_2}\sqrt{g_{33}}dw \tag{2.31}$$

In a rotational coordinate system the distance between two points w_1, w_2 is:

$$R_v[w_1,w_2]=\sqrt{g_{33}}(w_2-w_1) \tag{2.32}$$

where w_1, w_2 are in radians.

2.6.4. DIFFERENTIAL OPERATORS

In curvilinear coordinate system the gradient operator is defined as:

$$\nabla V(u,v,w)=\frac{1}{\sqrt{g_{11}}}\frac{\partial}{\partial u}V(u,v,w)\hat{u}+\frac{1}{\sqrt{g_{22}}}\frac{\partial}{\partial v}V(u,v,w)\hat{v}+\frac{1}{\sqrt{g_{33}}}\frac{\partial}{\partial w}V(u,v,w)\hat{w} \tag{2.33}$$

The Laplacian operator is defined as:

$$\nabla^2 V(u,v,w)=\frac{1}{\sqrt{g_{11}g_{22}g_{33}}}\left(\frac{\partial}{\partial u}\left(\sqrt{\frac{g_{22}g_{33}}{g_{11}}}\frac{\partial V(u,v,w)}{\partial u}\right)+\frac{\partial}{\partial v}\left(\sqrt{\frac{g_{11}g_{33}}{g_{22}}}\frac{\partial V(u,v,w)}{\partial w}\right)+\frac{\partial}{\partial w}\left(\sqrt{\frac{g_{11}g_{22}}{g_{33}}}\frac{\partial V(u,v,w)}{\partial w}\right)\right) \tag{2.34}$$

The CURL operator is defined as:

$$\nabla\times E=\begin{bmatrix}\dfrac{\hat{u}}{\sqrt{g_{22}g_{33}}} & \dfrac{\hat{v}}{\sqrt{g_{11}g_{33}}} & \dfrac{\hat{w}}{\sqrt{g_{11}g_{22}}}\\ \dfrac{\partial}{\partial u} & \dfrac{\partial}{\partial v} & \dfrac{\partial}{\partial w}\\ \sqrt{g_{11}}E_u(u,v,w) & \sqrt{g_{22}}E_V(u,v,w) & \sqrt{g_{33}}E_w(u,v,w)\end{bmatrix} \tag{2.35}$$

Divergence and vector Laplacian operators are not used in this particular example and are not presented here.

2.7. SOLUTION OF LAPLACE EQUATION

As we explained in the introduction, one of the reasons for choosing the ISP system is that the Laplace equation is r-separable, as will be shown in the following development.

Let us start from the Laplace equation,

$$\nabla^2 V(u,v,w) = 0 \tag{2.36}$$

This equation is said to be *R-Separable* if the assumption of a potential function of the form:

$$V(u,v,w) = \frac{H(u)\Theta(v)\Psi(w)}{R(u,v,w)} \tag{2.37}$$

leads to separate equation (2.36) into three ordinary differential equations [1].

If the function *R(u, v, w)*, is a constant, the equation is called simple separable, see [1].

The metric coefficients for the ISP system can be obtained by replacing equations (2.11) into Equation (2.22):

$$g_{11} = g_{22} = \frac{a^2\left(\sinh(u)^2 + \sin(v)^2\right)}{\cosh(u)^2 - \sin(v)^2} \tag{2.38}$$

$$g_{33} = a^2 \frac{\sinh(u)^2 \sin(v)^2}{\left(\cosh(u)^2 - \sin(v)^2\right)^2} \tag{2.39}$$

Notice that the metric coefficients in this space are independent from the angular variable (*w*).

The Laplace equation on this system can be obtained by replacing equations (2.38) and (2.39) into Equation (2.34):

$$\begin{aligned}&\nabla^2 V(u,v,w) = 0 = \\ &\frac{\Omega^3}{a^2 \Pi \sinh(u)\sinh(v)}\left(\sinh(v)\frac{\partial}{\partial u}\left(\frac{\sinh(u)}{\Omega}\frac{\partial}{\partial u}V(u,v,w)\right) + \sinh(u)\frac{\partial}{\partial v}\left(\frac{\sinh(v)}{\Omega}\frac{\partial}{\partial v}V(u,v,w)\right)\right) + \\ &\frac{\Omega^2}{a^2 \Pi \sinh^2(v)\sinh^2(u)}\frac{\partial^2}{\partial w^2}V(u,v,w)\end{aligned} \tag{2.40}$$

where:

$$\begin{aligned}\Pi &= \sinh^2(u) + \sin^2(v) \\ \Omega &= \frac{1}{R^2(u,v)} = \cosh^2(u) - \sin^2(v)\end{aligned} \tag{2.41}$$

and *V*(*u*, *v*, *w*) is the potential function.

As the boundary conditions are imposed on the surface of the electrodes (*u=constant*) and the problem has rotational symmetry, the potential *V* is independent from the functions Θ(*v*) and Ψ(*w*). This simplifies Equation (2.37) into:

$$V(u,v) = \sqrt{\Omega} H(u) \tag{2.42}$$

The differential equation resulting when replacing Equation (2.42) into Equation (2.40) is:

$$\frac{\partial^2 H(u)}{\partial u^2} + \cosh(v)\frac{\partial H(u)}{\partial u} = 0 \tag{2.43}$$

The solution of which is of the form [1]:

$$H(u) = A + B\log\left(\coth\left(\frac{u}{2}\right)\right) \tag{2.44}$$

where *A* and *B* are terms independent from *u* and can be calculated using the boundary conditions of the problem, which are applied on the surface of the electrodes:

$$\begin{aligned} V(u_2,v) &= 0 \\ V(u_1,v) &= V_1 \end{aligned} \tag{2.45}$$

The obtained expressions for *A* and *B* are:

$$A = V_1 \frac{\ln\left(\coth\left(\frac{u_1}{2}\right)\right)}{\ln\left(\frac{\coth\left(\frac{u_2}{2}\right)}{\coth\left(\frac{u_1}{2}\right)}\right)\sqrt{\cosh^2(u_2) - \sin^2(v)}} \tag{2.46}$$

$$B = V_1 \frac{1}{\ln\left(\frac{\coth\left(\frac{u_1}{2}\right)}{\coth\left(\frac{u_2}{2}\right)}\right)\sqrt{\cosh^2(u_2) - \sin^2(v)}} \tag{2.47}$$

From this, the function for the potential can be fully specified:

$$V(u,v)=\frac{V_1}{k_1}\ln\left(k_3\coth\left(\frac{u}{2}\right)\right)\sqrt{\frac{\cosh^2(u)-\sin^2(v)}{k_2^2-\sin^2(v)}} \tag{2.48}$$

where the constants k_1,k_2,k_3 are:

$$k_1=\ln\left(\frac{\coth\left(\frac{u_1}{2}\right)}{\coth\left(\frac{u_2}{2}\right)}\right) \qquad k_2=\cosh(u_1) \qquad k_3=\frac{1}{\coth\left(\frac{u_2}{2}\right)} \tag{2.49}$$

2.8. ELECTROSTATIC FIELD CALCULATION

The electrostatic field $E(u, v, w)$ can be calculated from the potential $V(u, v, w)$:

$$E(u,v,w)=-\nabla V(u,v,w) \tag{2.50}$$

Applying the equation for the gradient in the ISP coordinate system defined by Equation (2.33) to Equation (2.48) leads to:

$$E(u,v,w)=-\frac{\Omega}{a}\left(\frac{1}{\sqrt{\Pi}}\left(\frac{\partial V}{\partial u}\hat{u}+\frac{\partial V}{\partial v}\hat{v}\right)+\frac{\hat{w}}{\sinh(v)\sin(u)}\frac{\partial V}{\partial w}\right) \tag{2.51}$$

The component in direction w vanishes, the other two components in directions u and v read as:

$$E_u(u,v,w)=\frac{V_1\sqrt{\Omega}\left(\ln\left(\frac{\coth(u/2)}{\coth(u_2/2)}\right)\sinh(2u)-2\cosh(u)\coth(u)+2\csc h(u)\sin(v)^2\right)}{ak_1\sqrt{\cosh(2u)-\cos(2v)}\sqrt{\cos(2v)+\cosh(2u_1)}} \tag{2.52}$$

$$E_v(u,v,w)=\frac{V_1\sin(2v)\sqrt{\cos(2v)+\cosh(2u)}\left(\cosh(2u)-\cosh(2u_1)\right)\left(\ln\left(\frac{\coth(u/2)}{\coth(u_2/2)}\right)\right)}{ak_1\sqrt{2}\sqrt{\cosh(2u)-\cos(2v)}\left(\cos(2v)+\cosh(2u_1)\right)^{3/2}} \tag{2.53}$$

The analytical expressions for the electric field and the potential, obtained through equations (2.48), (2.52) and (2.53) can be applied to the profiles calculated in Section 2.5, and presented in Figure 2.5.

Figure 2.6 shows the electrostatic field distribution in u direction, for an applied voltage V_1=1V. The field was calculated along the surface of the electrodes (u=u_2, u=u_1) and the along a constant surface u_3=0.5(u_2+u_1), which corresponds to the midplane between the electrodes.

The Figure includes two horizontal axes: the distance along the electrodes and the parameter v divided by π. Notice the enhancement of the field at $v=0$, and the monotonous decreasing as v increases.

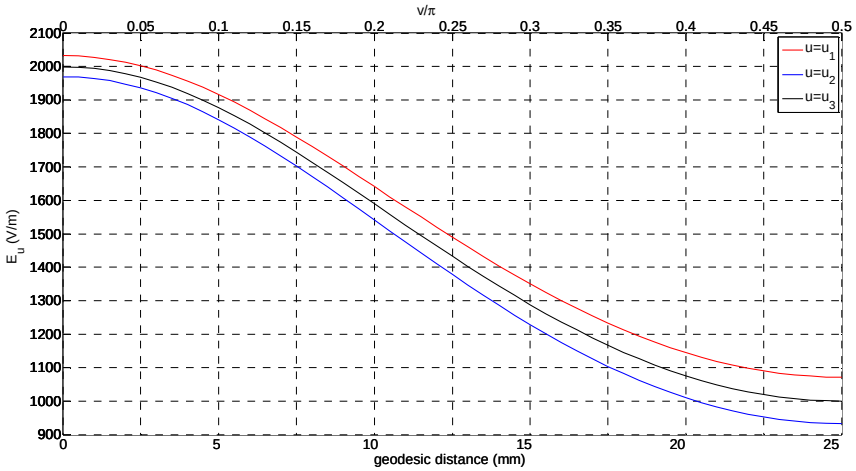

Figure 2.6. Electrostatic field distribution (in V/m) along the internal (red curve) and external (blue curve) electrodes. The black curve shows the electric field along the mid plane between the electrodes. The bottom axis is the distance along the curves, the bottom axis is the v parameter normalized to π

Figure 2.7 shows a contour plot of the electrostatic field distribution in u direction, as a function of the parametric coordinates (u, v). This graph covers the region $u_1<u<u_1$, $0<v<\pi$, therefore it summarizes the electrostatic field distribution in the interlectrodic space. The figure shows that, as expected, the electric field intensification occurs when u tends to u_1, and $v=0$.

A similar graph for the field in v direction ($E_v(u,v)$) is presented in Figure 2.8. It can be seen that the minimum amplitude of E_u is more than 2000 times bigger than the maximum absolute amplitude of E_v. Due to this, it can be said that the influence of the E_v can be considered as negligible.

Figure 2.9 presents the electric field distribution within the interelectrodic space drawn in the x-z plane. Notice that the E-field is maximum on the axis of symmetry. The potential distribution on the (u,v) plane can be seen in Figure 2.10.

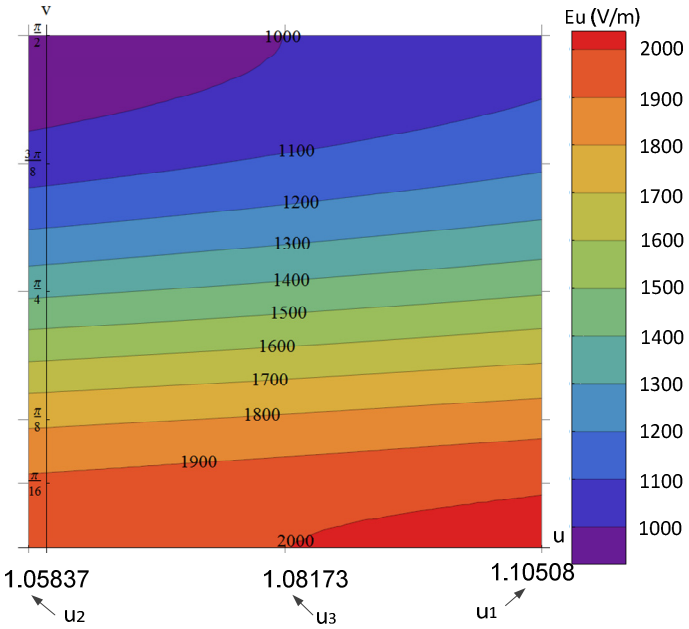

Figure 2.7 Contour plot of the electrostatic field distribution in direction *u* (E_u) vs. the parametric coordinates (*u*,*v*)

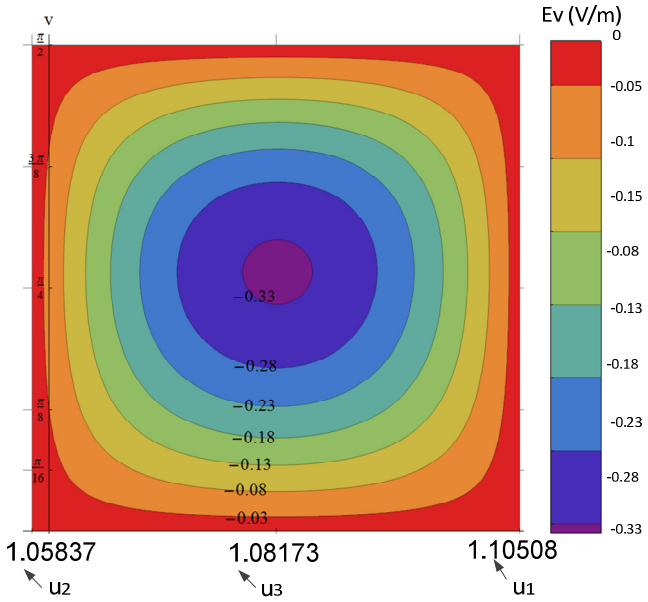

Figure 2.8 Contour plot of the electrostatic field distribution in direction *v* (E_v) vs. the parametric coordinates (*u*,*v*)

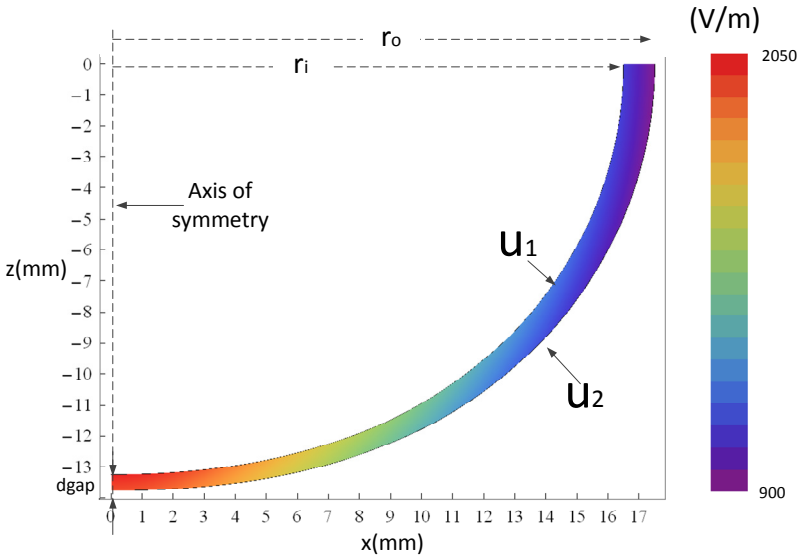

Figure 2.9 Electrostatic field distribution in direction *u* (E_u) in the (*x*,*z*) plane.

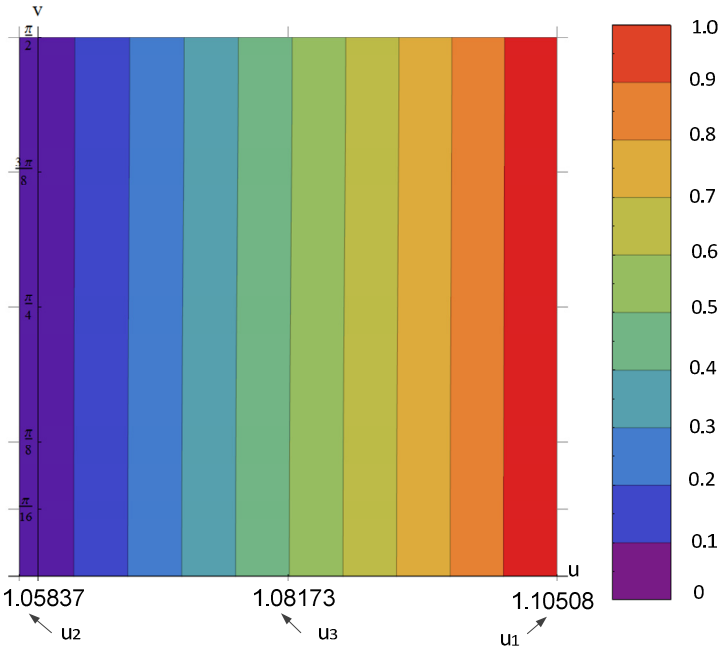

Figure 2.10 Potential distribution vs., parametric coordinates (*u*,*v*)

As a summary of the presented analysis, it can be said that the proposed IPS profile fulfills all the five conditions enunciated in Section 2.3; The most important being that the electric field amplitude maximizes at the axis of symmetry and decreases monotonically in the *v* direction.

2.9. ELECTROSTATIC SIMULATION

A simulation of the calculated profiles, attached to a coaxial transmission line was performed using the 2-D axis symmetrical electrostatic module in Comsol®. A potential difference of 1V was applied between the electrodes and the resulting electrostatic field distribution was computed. The boundary conditions of the geometry are presented in Figure 2.11.

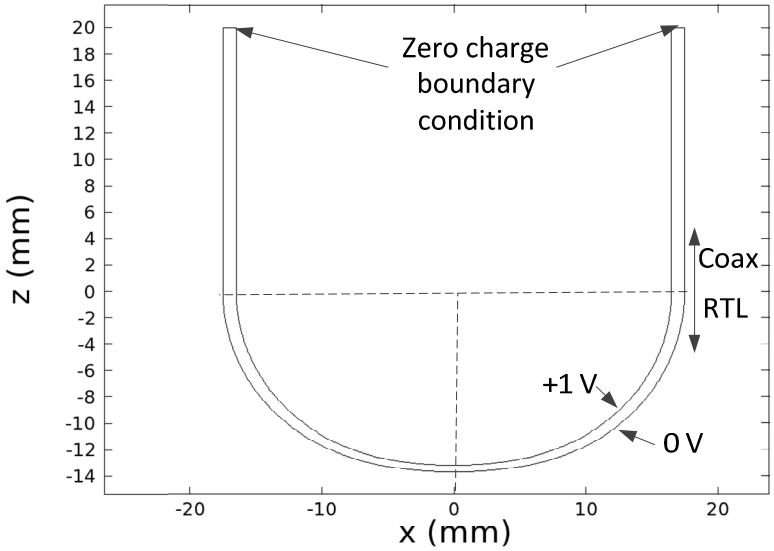

Figure 2.11 Geometry and boundary conditions of the electrostatic simulation.

The resulting electrostatic field distribution is presented in Figure 2.12. This result coincides with the analytical plot, presented in Figure 2.9. No field distortion is observable at the interface between the coaxial and the electrodes. The isopotential lines are plotted in Figure 2.13

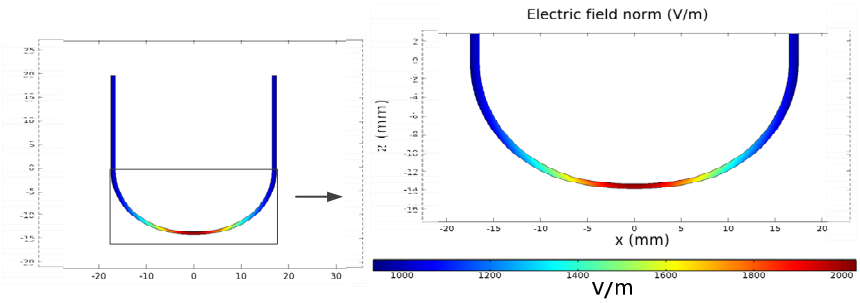

Figure 2.12 Electrostatic field amplitude in the interelectrodic space. The scale is in V/m. notice that the maximum amplitude occurs at the axis of symmetry

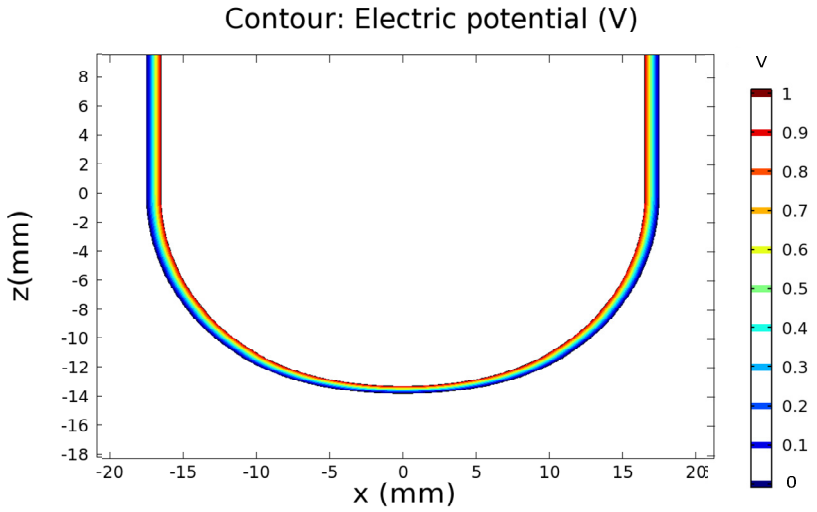

Figure 2.13 Electric potential distribution, in Volts. Notice how the isopotential lines adapt smoothly to the coaxial section.

The isopotential lines (without color scale) and the electric field stream lines are presented in Figure 2.14. As expected, the electric field stream lines are conformal to the *v-set* and the isopotential lines are conformal to the *u-set*. It can be seen that the stream lines are parallel to the *z* axis at the axis of symmetry, and parallel to the *x* axis at the connection point between the coaxial and the RTL.

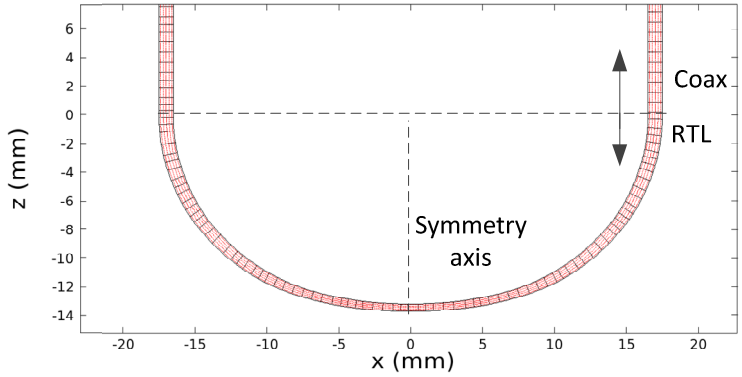

Figure 2.14 Electric field stream lines (blue) and isopotential lines (red). Notice that the direction of the stream lines progressively changes and become radial at the beginning of the coaxial transmission line. The opposite change occurs for the isopotential line, which become progressively adopt the direction z.

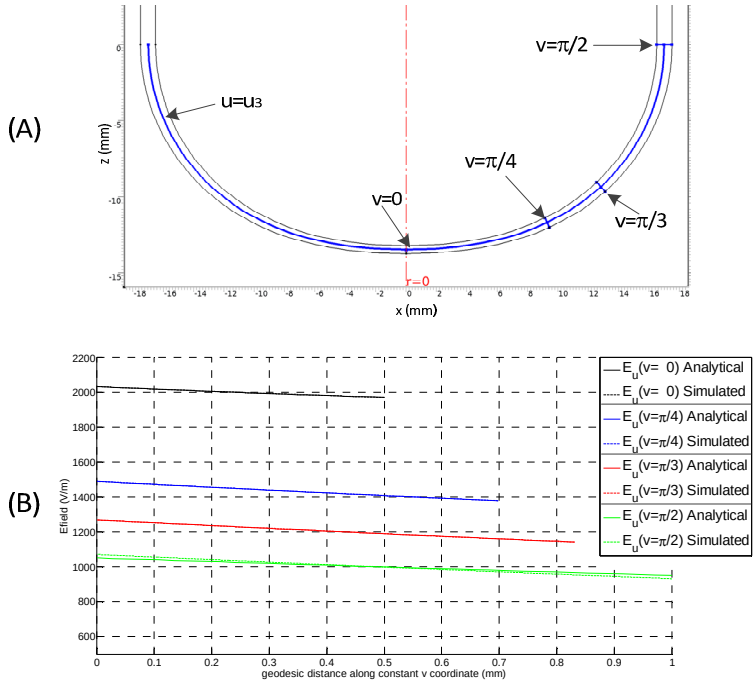

Figure 2.15 Constant $u=u_3$ and v trajectories (A). Simulated and analytical electric field amplitude along lines geodesic distance calculated along *v=constant*. The zero in the horizontal axis corresponds to the internal electrode (B). Simulated and analytical quantities are in excellent agreement.

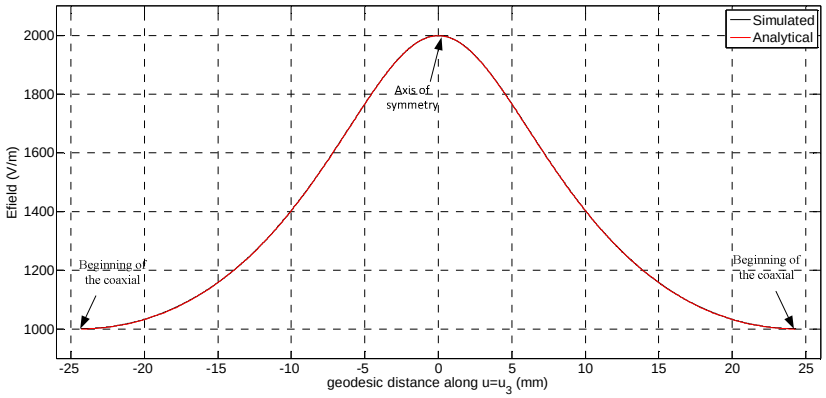

Figure 2.16 Simulated and analytical electric field along a constant *u* line $u_3=0.5(u_1+u_2)$ vs the parameter *v*. Notice the monotonic decrease of the electric field. Both quantities are in excellent agreement.

Figure 2.15 (A) shows different lines *v=constant, u=constant,* along the developed analytical equations for the electric field are compared to numerical simulations. The results on the *v-lines* are shown in Figure 2.15 (B). It can be seen that the analytical solutions are in excellent agreement with numerical simulations.

Figure 2.16 presents the theoretical and simulated electrostatic field amplitude along the midplane between the electrodes (the surface $u_3=0.5(u_1+u_2)$), see Figure 2.15 (A) for details. Both results are in excellent agreement.

2.10. LIMITATIONS OF THE THEORETICAL MODEL

The junction between the electrodes and the coaxial line is one of the critical points of the design. At the junction, the directions of the electric field between the electrodes and inside the coaxial are coincident, as shown in Figure 2.4. However, as we will see later in this section, simulation results show that a slight difference in the amplitude of the electric field exists at this point. A discussion on this point is presented here.

On the *x-z* plane, the junction is located on the line defined between the points:

$$\begin{aligned}(x_i, z_i) &= (r_i, 0)\\ (x_o, z_o) &= (r_o, 0)\end{aligned} \tag{2.54}$$

which correspond to the parametric coordinates:

$$\begin{aligned}(u_i, v_i) &= \left(u_1, \frac{\pi}{2}\right)\\ (u_o, v_o) &= \left(u_1, \frac{\pi}{2}\right)\end{aligned} \tag{2.55}$$

According to Equation (2.52), the electric field on the surface of the electrodes is:

$$E_{i,ISP} = E_u\left(u_1, \frac{\pi}{2}\right) = -V_1 \frac{\operatorname{csch}(u_1)\sinh(u_1)\tanh(u_1)}{a\ \ln\left(\coth\left(\frac{u_1}{2}\right)\tanh\left(\frac{u_1}{2}\right)\right)} \tag{2.56}$$

$$E_{o,ISP} = E_u\left(u_2, \frac{\pi}{2}\right) = -V_1 \frac{\operatorname{csch}(u_2)\sinh(u_2)\tanh(u_2)}{a\ \ln\left(\coth\left(\frac{u_2}{2}\right)\tanh\left(\frac{u_2}{2}\right)\right)} \tag{2.57}$$

The fields on the internal and external conductors of the surface of the coaxial line are:

$$E_{i,Coax} = \frac{-V_1}{r_i \ln\left(\frac{r_o}{r_i}\right)} \tag{2.58}$$

$$E_{o,Coax} = \frac{-V_1}{r_o \ln\left(\frac{r_o}{r_i}\right)} \tag{2.59}$$

Replacing Equations (2.17) and (2.18) into Equations (2.58) and (2.59) leads to:

$$E_{i,Coax} = \frac{-V_1}{\operatorname{csch}(u_1)\ln\left(\frac{\operatorname{csch}(u_2)}{\operatorname{csch}(u_1)}\right)a} \tag{2.60}$$

$$\mathrm{E_{o,Coax}} = \frac{-\mathrm{V_1}}{\operatorname{csch}(\mathrm{u_2})\ln\left(\frac{\operatorname{csch}(\mathrm{u_2})}{\operatorname{csch}(\mathrm{u_1})}\right)\mathrm{a}} \tag{2.61}$$

The difference between the fields at the electrodes and at the coaxial line can be estimated applying an error estimation figure, such as the percent error, to equations (2.60) , (2.56) and Equations (2.61), (2.57).

The percent error of the field on the inner and outer conductors is given, respectively, by:

$$e_{out} = \frac{E_{o,Coax} - E_{o,ISP}}{E_{o,Coax}} 100\% \tag{2.62}$$

$$e_{in} = \frac{E_{i,Coax} - E_{i,ISP}}{E_{i,Coax}} 100\% \tag{2.63}$$

As analytical evaluation of these expressions is demanding, we'll present a numerical evaluation of the error, as a function of u_1, u_2. Notice that a, the scale factor, doesn't intervene in the equations for the percent error.

Contour plots of Equations (2.62) and (2.63) are presented in Figure 2.17 and Figure 2.18, respectively.

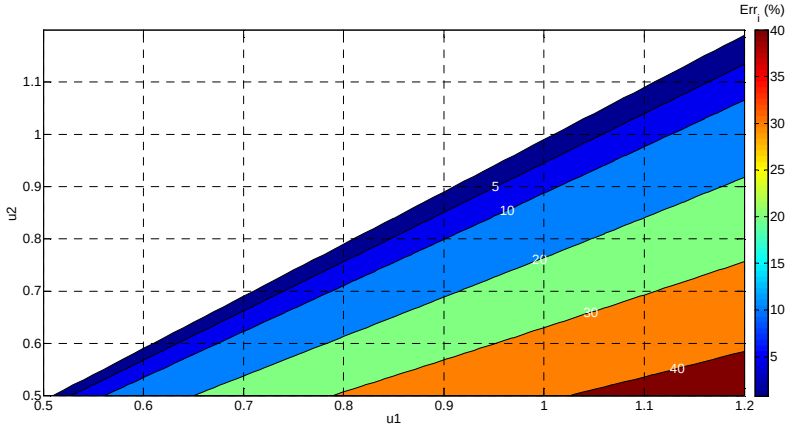

Figure 2.17 percent error of the field on the inner conductor

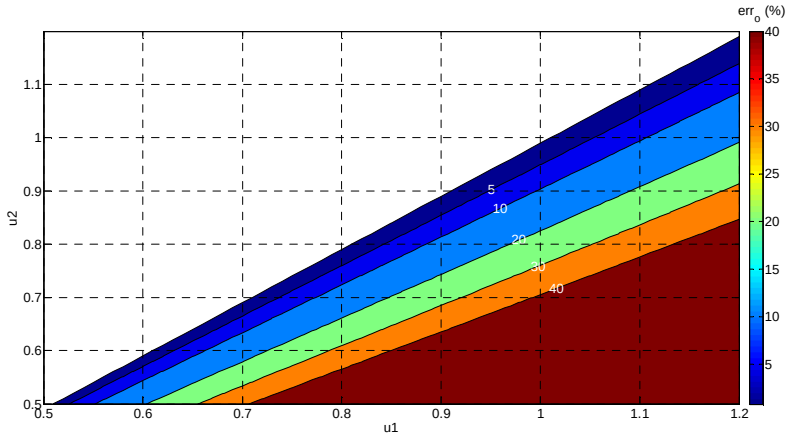

Figure 2.18 percent error of the field on the outer conductor

From the graphs, it can be concluded that the difference of the fields at the junction depends on the difference between u_2 and u_1.

Question arises on the range of geometries that can be generated without exceeding a certain threshold; let's say a maximum percent error of 5%. We can ad-

dress this question by evaluating the range of impedances that can be connected to the electrodes with a low percent error.

Replacing Equations (2.17) and (2.18) into the equation for the impedance of the coaxial leads to:

$$Z_{coax}=60\ln\left(\frac{r_0}{r_i}\right)=60\ln\left(\frac{\operatorname{csch}(u_2)}{\operatorname{csch}(u_1)}\right) \tag{2.64}$$

A graph of the percent error as a function of the impedance is presented in Figure 2.19. From this figure it can be concluded that good continuity between the coaxial transmission line and the corresponding IPS electrodes can be achieved for low values of the impedance of the coaxial line. In particular, it can be noticed that for impedances of 5 Ω or lower, the error is less than 6%.

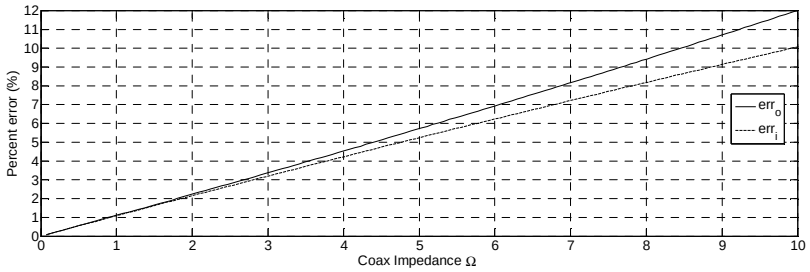

Figure 2.19 Percent error on the inner and outer conductor as a function of the impedance of the coaxial line. Notice that for low-value impedances the percent error is small.

We will illustrate this with two examples. The first one is the set of electrodes shown in Figure 2.20, which have the following characteristics:

- Z_o=4.1 Ω, d_{gap} =0.5 mm, r_i=14 mm, r_o =15 mm.

The constants defining the profiles are:

$$u_1=1.10925, u_2=1.05448, a=18.9158e-3$$

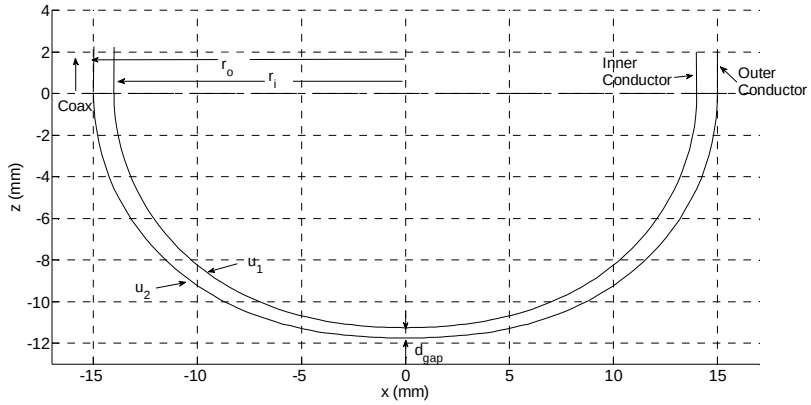

Figure 2.20 Example of IPS electrodes. The coaxial line has Z_o=4.1, Ω, r_i=14 mm, r_o=15 mm. The gap distance is d_{gap}=0.5 mm

Figure 2.21 shows the electric field at the mid plane between the electrodes and the surface electric field, along the electrodes. The results were obtained by simulation in Comsol ®.

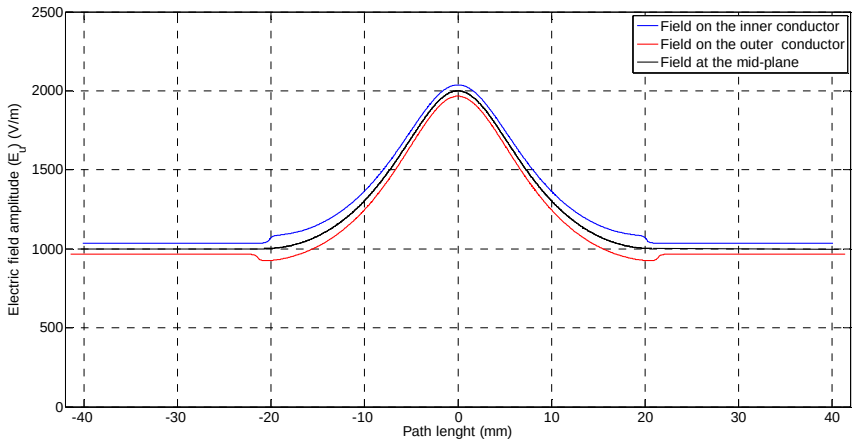

Figure 2.21 Electric field on the inner conductor (blue), outer conductor (red) and middle plane (black) of two IPS electrodes connected to a coaxial with Z_o=4.1 Ω. The gap distance is 0.5 mm. The dimensions of the coaxial line are r_i=14 mm r_o=15 mm. The small bump on the electric field at the connecting point of the coaxial doesn't represent an additional risk of disruption, as no local enhancements of the fields are present.

As comparison, we can refer to the IPS electrodes shown in Figure 2.22, having:

- Z_o=10.9 Ω, d_{gap} =0.5 mm, r_i=12.5 mm, r_o =15 mm.

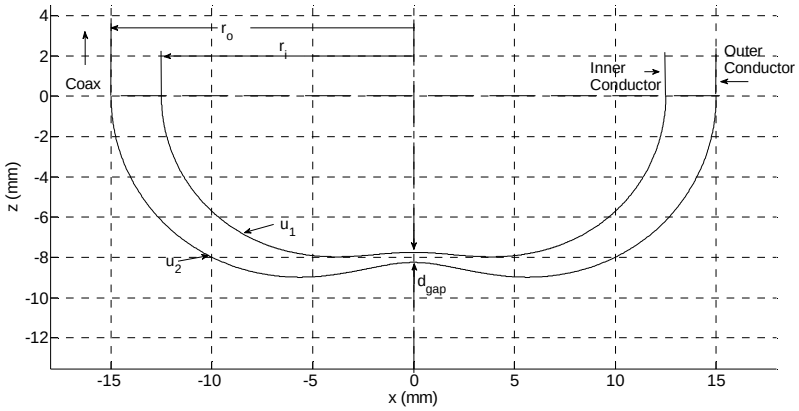

Figure 2.22 Example of IPS electrodes. The coaxial line has Z_o=10.9 Ω, r_i=12.5 mm, r_o=15 mm. The gap distance is d_{gap}=0.5 mm

The electric field computed by simulation is shown in Figure 2.23. As expected, the percent error for this case is larger than in the previous case. On the same graph it can be observed that the electric field is higher on the outer electrode, this is due to the fact that this surface has a higher radius of curvature near the axis of symmetry compared to the inner electrode.

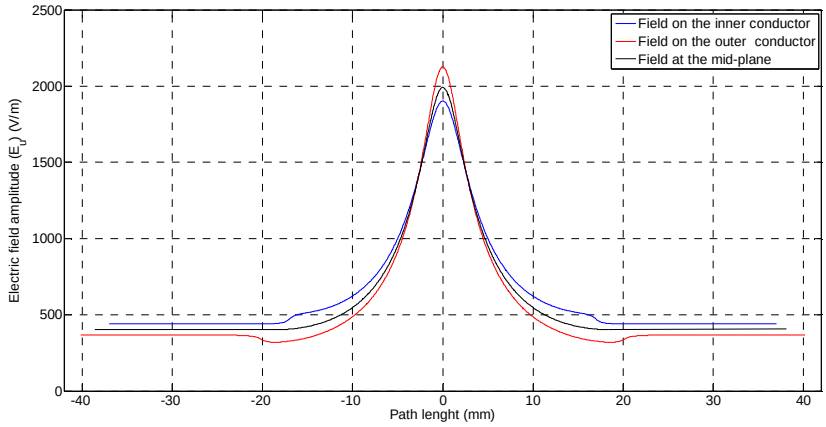

Figure 2.23 Electric field on the inner conductor (blue), outer conductor (red) and middle plane (black) of two IPS electrodes connected to a coaxial with Z_o=10.9 Ω. The gap distance is 0.5 mm. The dimensions of the coaxial line are r_i=12.5 mm r_o =15 mm. Notice the deformation of the electric field at the connecting point of the coaxial. It can be seen that, near the axis of symmetry, the magnitude of the electric field is higher on the outer conductor; this is due to a higher degree curvature of the u_2 profile on this region.

According to these results, the analytical expressions for the IPS should be used only in SWOs having low-impedance coaxial lines. However, this is not a major limitation on the applicability of the model, because most of the SWOs reported in

the literature are of this kind, having impedances in the order of 5 Ω [5, 6, 10, 11]. Low impedance lines have bigger capacitance and can store more electrostatic energy. On the other hand, the lower the impedance of the line the bigger the mismatch with the antenna and therefore the higher the Q factor of the produced signal.

2.11. CONCLUSIONS

A new profile for the electrodes forming the radial transmission line (RTL) of a switched oscillator (SWO) was presented. The profile was formed using a curvilinear space called Inverse Prolate Spheroidal (IPS) coordinate system. We have derived design equations for producing the electrodes starting from the basic geometric requirements of spark gap distance and radii of the coaxial transmission line.

The IPS profile results in an optimal distribution of the electric field, with a peak amplitude occurring at the axis of symmetry of the SWO, and a smooth, monotonic decrease as one moves away from the discharge point towards the coaxial transmission line.

The Laplace equation was solved on this curvilinear space and analytical expressions for the electrostatic field and potential were obtained.

An illustrated example was proposed, for which electrostatic numerical simulations were performed. The resulting distributions of the electric field and potential were presented and discussed.

It was shown that the derived analytical expressions are in very good agreement with numerical simulations, especially for SWOs having a low impedance coaxial line.

REFERENCES

[1] P. Moon and D. E. Spencer, *Field Theory Handbook: Including Coordinate Systems, Differential Equations and Their Solutions* 2ed.: Springer-Verlag, 1971.

[2] W. Rogowski, "Die elektrische Festigkeit am Rande des Plattenkondensators," *Archiv f?r Electrotechnik*, vol. 12, pp. -, 1923.

[3] G. J. Ernst, "Uniform-field electrodes with minimum width," *Optics Communications*, vol. 49, pp. -, 1984.

[4] F. M. Bruce, "Calibration of uniform-field sparkgaps for high-voltage measurement at power frequencies," *Journal of IEE, pt.II*, vol. 94, pp. -, 1947.

[5] D. V. Giri, *et al.*, "Switched Oscillators and Their Integration Into Helical Antennas," *Plasma Science, IEEE Transactions on*, vol. 38, pp. 1411-1426, 2010.

[6] M. Armanious, *et al.*, "Electrostatic field management and electrodynamic modeling of switched quarter-wave oscillators," *Dielectrics and Electrical Insulation, IEEE Transactions on*, vol. 18, pp. 1054-1065, 2011.

[7] F. Vega, *et al.*, "A New Set of Electrodes for the Coaxial Quater Wave Switched Oscillator," *Sensor and Simulation Notes 560,* 2012.

[8] P. Moon and D. E. Spencer, "Cylindrical and Rotational Coordinate Systems," *Journal of Franklin Institute,* vol. 52, p. 327, 1951.

[9] P. M. Morse and H. Feshbach, *Methods of Theoretical Physics, Part I*: McGraw Hill Book Company, 1953.

[10] Baum.C.E, "Switched Oscillators," *Circuit and Electromagnetic System Design Notes,* vol. 45, pp. -, September 2000.

[11] J. W. Burger, *et al.*, "Modular Low Frequency High Power Microwave Generator," presented at the AMEREM, Annapolis M.D, USA, 2002.

CHAPTER 3

CHARACTERISTIC IMPEDANCE OF THE INVERSE PROLATE SPHEROIDAL - RADIAL TRANSMISSION LINE OF THE SWO

3.1. INTRODUCTION

Consider the geometry of the coaxial SWO proposed in Figure 3.1, consisting of a self-breaking spark gap followed by a low-impedance coaxial transmission line, a DC-blocking capacitor, and a frequency dependent antenna (in this case a monopole). Notice that the electrodes forming the spark gap at the bottom-end of the SWO configure a curved transmission line, whose model corresponds to a radial transmission line (RTL) [1].

An equivalent circuit diagram associated to the system under study is presented in Figure 3.2. The circuit comprises an equivalent voltage source associated with the spark gap, connected to three cascaded transmission lines: (i) the non-uniform RTL line, (ii) the coaxial line, and (iii) a secondary transmission coaxial line that can represent the elements installed at the end of the SWO due to mechanical reasons (for instance, dielectric supports, dielectric rings, pressure sealing, etc.).

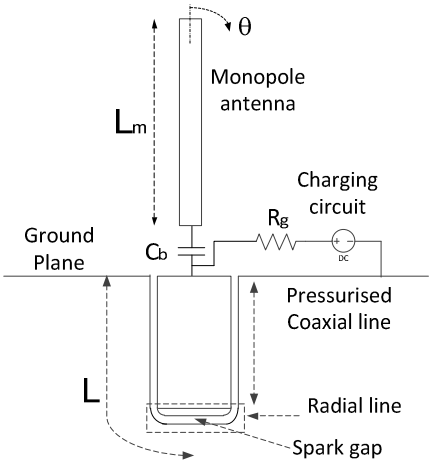

Figure 3.1 A monopole antenna integrated into a SWO

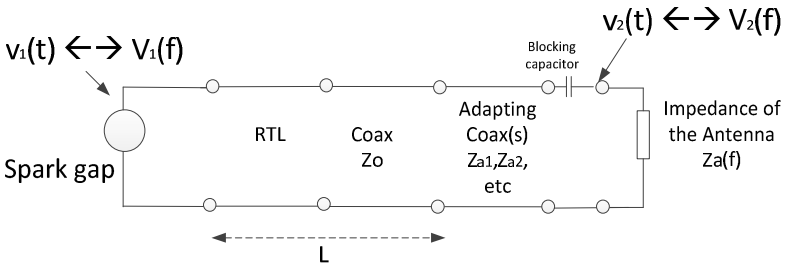

Figure 3.2 Transmission line system representing the SWO. V_1 is the voltage produced by breakdown of the spark gap. V_2 is the voltage at the terminals of the antenna. Adapting coax denotes the adapting transmission line that might be installed at the end of the main coaxial.

In Chapter 4, we will introduce the calculation of the frequency-domain transfer function between the voltage at the spark gap and the voltage at the terminals of the antenna. To do this, it is required to characterize each one of the elements appearing in Figure 3.2. More precisely, it is necessary to know the characteristic impedance of each element.

For the case of the present work, the RTL is formed by the IPS electrodes developed in Chapter 2. Therefore, we will study the behavior of the fields corresponding to this system. Starting from the electrostatic results for the IPS electrodes, analytical expressions for the electric and magnetic fields in the frequency domain will be derived. Afterwards, an expression for the characteristic impedance of this section will be obtained. This procedure follows the classical methodology described by Collin in Section 3.2 of [2].

3.2. REVIEW OF THE IPS COORDINATE SYSTEM

In Chapter 2, we presented a set of electrodes based on the Inverse Prolate Spheroidal coordinate system (IPS), proposed by Moon and Spencer in [3].

We chose this coordinate system because its spheroidal surfaces satisfy the design criteria for the electrostatic distribution.

On the other hand, the Laplace Equation is R-Separable in this coordinate system. This implies that an analytical expression for the electrostatic potential can be found.

For the sake of clarity and self-consistency of this chapter, we present a brief description of the concepts and results concerning the IPS electrodes. More details can be found in Chapter 2.

The surface of IPS electrodes are defined in a three dimensional coordinate system (u,v,w), where the following transformation with the Cartesian coordinates exists:

$$x = a\frac{\sinh(u)\sin(v)\cos(w)}{\cosh^2(u)-\sin^2(v)} \tag{3.1}$$

$$y = a\frac{\sinh(u)\sin(v)\sin(w)}{\cosh^2(u)-\sin^2(v)} \tag{3.2}$$

$$z = a\frac{\cosh(u)\cos(v)}{\cosh^2(u)-\sin^2(v)} \tag{3.3}$$

where $a>0$ is a constant, and

$$0 \le u < +\infty \qquad 0 \le v \le \pi \qquad 0 \le w \le 2\pi \tag{3.4}$$

In this system, the surfaces u=*constant* (called here the *u-set*) form inverted prolate spheroids of revolution, the surfaces v=*constant* (called here the *v-set*)

form inverted double sheet hyperboloids of revolution, and the surfaces *w=constant* form planes. Figure 3.3 shows a 2D cut of the IPS coordinates at *w=0*, corresponding to the Cartesian *x*-*z* plane.

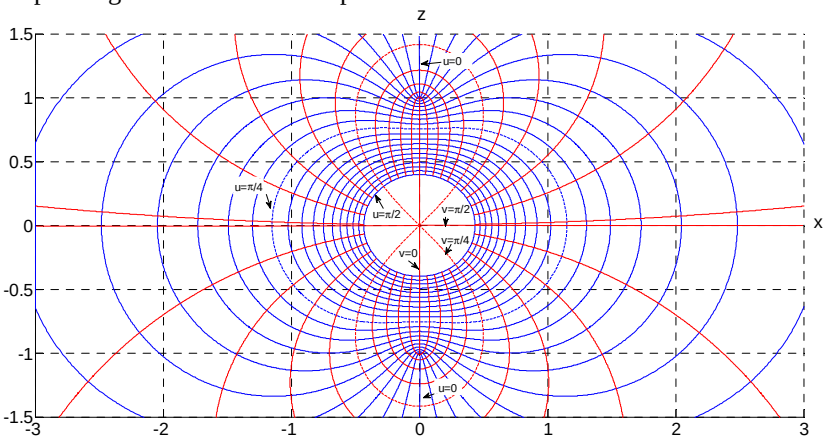

Figure 3.3 2D cut of the IPS coordinates at *w=0*. The *u-set* is colored in blue, the *v-set* is colored in red. In this example, the adopted value for the constant *a* is 1. The electrodes can be formed by rotating two curves belonging to bottom half of the *u-set* around the *z* axis.

The profile of the inner and outer electrodes are formed respectively by the surfaces $S_1=(u_1,v,w)$ and $S_2=(u_2,v,w)$, where $\pi/2<v<3\pi/2$. The constants u_1, u_2 and a are calculated from the 3x3 set of equations:

$$d_{gap} = \frac{a}{\cosh(u_2)} - \frac{a}{\cosh(u_1)} \tag{3.5}$$

$$r_i = a \times \operatorname{csch}(u_1) \tag{3.6}$$

$$r_o = a \times \operatorname{csch}(u_2) \tag{3.7}$$

where: r_i, r_o are the inner and outer radii of the coaxial line and d_{gap} is the distance between the surfaces at the axis of symmetry, the point at which the discharge is supposed to occur.

3.3. IMPEDANCE OF THE RTL AT THE COAXIAL END

Due to various reasons such as the amount of electrostatic energy that can be stored in the SWO and the quality factor *Q* of the voltage at the antenna's input, SWOs use low-impedance coaxial lines, with typical values in the order of 4 to 7 Ohms [1, 4-7]. In the present work, we could define a round limit of 10 Ohms as the maximum impedance of a coaxial line to be connected to an SWO. The range of values u_1, u_2 defining this low-impedance zone can be found as follows:

If the material at the interelectrodic space has permittivity a $\varepsilon_r=1$, the impedance of the coaxial line is:

$$Z_{coax} = 60Log\left(\frac{r_o}{r_i}\right)(\Omega) \tag{3.8}$$

Replacing equations (3.6) and (3.7) into (8) yields

$$Z_{coax} = 60log\left(\frac{csch(u_2)}{csch(u_1)}\right)(\Omega) \tag{3.9}$$

Setting the maximum value of the coaxial impedance to 10 Ω, we can say that the *zone of low-impedance* is defined by the range of values u_1, u_2 satisfying:

$$60log\left(\frac{csch(u_2)}{csch(u_1)}\right) < 10 \tag{3.10}$$

Figure 3.4 shows a parametric graph of the impedance of the RTL at the coaxial end as a function of the parameters u_1, u_2. The diagonal of the graphs correspond to zero impedance (u_1=u_2). As u_1>u_2, we only consider the part of the graph below the diagonal. The other half of the graph is colored in purple, indicating that the function is not defined.

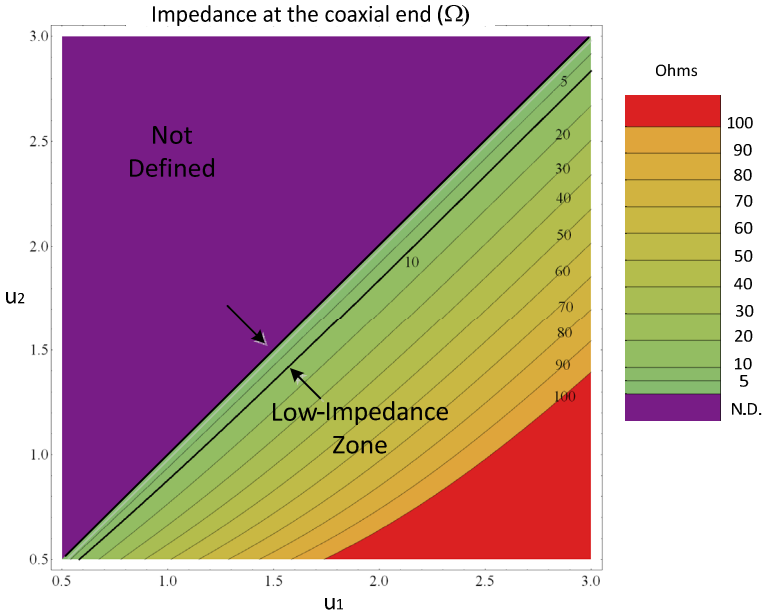

Figure 3.4 Impedance of the RTL at the coaxial end. Notice that the low impedance region is near the diagonal of the graph

The contour line representing the limit of 10 Ohms is in the vicinity of the diagonal; therefore we can say that, if a low impedance is desired at the coaxial end of the RTL, then we should have $u_1 \sim u_2$.

The precise values of the pair u_1, u_2 will depend on the value d_{gap} according to Equation (3.5).

3.4. ELECTRIC FIELD DISTRIBUTION

The discharge produced on the axis of symmetry of the RTL creates a wave that starts propagating in the *v* direction, towards the coaxial line.

If time-harmonic propagation in the *v* direction is assumed, the electric field between the plates can be found as:

$$E(u,v) = -\left(\nabla\Phi(u,v)\right)e^{-jkR(v)} \tag{3.11}$$

where:

- k is the wave number,
- $R(v)$, the geodesic distance, is the length of a path of constant v, measured from the axis of symmetry (v=0) to the point v. $R(v)$ is calculated using the metric coefficients presented in Chapter 2:

$$R(v) = \int_0^v \sqrt{g_{22}}\,dv = \int_0^v a\sqrt{\frac{\sinh(u)^2 + \sin(v)^2}{\cosh(u)^2 - \sin(v)^2}}\,dv \tag{3.12}$$

- $\Phi(u, v)$ is the potential function, corresponding to the solution of the Laplace equation found in Chapter 2 (in [2] this function is called the quasipotential). As discussed in Chapter 2, $\Phi(u, v)$ is of the form [3]:

$$\Phi(u,v) = \frac{V_1}{k_1}\log\left(k_3\coth\left(\frac{u}{2}\right)\right)\sqrt{\frac{\cosh^2(u) - \sin^2(v)}{k_2^2 - \sin^2(v)}} \tag{3.13}$$

where the constants k_1, k_2 and k_3 are function of u_1, u_2, the boundary conditions of the problem. V_1 is the peak voltage applied at the surface u_1. The surface u_2 is grounded.

$$k_1 = \log\left(\frac{\coth\left(\frac{u_1}{2}\right)}{\coth\left(\frac{u_2}{2}\right)}\right) \qquad k_2 = \cosh(u_1) \qquad k_3 = \frac{1}{\coth\left(\frac{u_2}{2}\right)} \tag{3.14}$$

Notice that, due to symmetry, E and Φ are independent from w.

By applying the gradient in the IPS system, it can be found that the electric field has one component in the *u* direction, transversal to the direction of propagation, and another one in the *v* direction, longitudinal to the direction of propagation:

$$E_u(u,v) = -\left(\frac{1}{\sqrt{g_{11}}}\frac{\partial\Phi(u,v)}{\partial u}\right)e^{-jkR(v)} \tag{3.15}$$

$$E_v(u,v) = -\left(\frac{1}{\sqrt{g_{22}}}\frac{\partial\Phi(u,v)}{\partial v}\right)e^{-jkR(v)} \tag{3.16}$$

Inserting the expression for the potential function (3.13) into equations (3.15) and (3.16), we obtain the analytical expressions for the transverse and longitudinal components of the electric fields:

$$E_u(u,v,w) = \\ = \frac{V_1}{a2k_1}\frac{\left(log\left(\frac{coth(u/2)}{coth(u_2/2)}\right)sinh(2u) - 2cosh(u)coth(u) + 2csch(u)sin(v)^2\right)}{\sqrt{cosh(2u)-cos(2v)}}\sqrt{\frac{cosh(2u)+cos(2v)}{cosh(2u_1)+cos(2v)}}e^{-jkR(v)} \tag{3.17}$$

$$E_v(u,v) = \\ = \frac{V_1}{ak_1\sqrt{2}}\frac{sin(2v)}{\sqrt{cosh(2u)-cos(2v)}}\left(log\left(\frac{coth(u/2)}{coth(u_2/2)}\right)\right)\frac{(cosh(2u)-cosh(2u_1))}{(cos(2v)+cosh(2u_1))}\sqrt{\frac{cosh(2u)+cos(2v)}{cosh(2u_1)+cos(2v)}}e^{-jkR(v)} \tag{3.18}$$

Equations (3.17) and (3.18) imply, s*trictu sensu*, that the wave propagating within the RTL is not a pure TEM. However, we can demonstrate that, in practice, the transverse component of the electric field is several orders of magnitude higher than the longitudinal component. Indeed, the ratio between the longitudinal and the transverse components of the electric field (R_T) is:

$$R_T(u,v) = \frac{E_v(u,v)}{E_u(u,v)} = \\ = \frac{sin(2v)\left(log\left(\frac{coth(u/2)}{coth(u_2/2)}\right)\right)\left(\frac{cosh(2u)-cosh(2u_1)}{cos(2v)+cosh(2u_1)}\right)}{\sqrt{2}log\left(\frac{coth(u/2)}{coth(u_2/2)}\right)sinh(2u)-2cosh(u)coth(u)+2csch(u)sin(v)^2} \tag{3.19}$$

This ratio maximizes when $v=\pi/4$:

$$R_T(u,\pi/4) = \frac{E_v(u,\pi/4)}{E_u(u,\pi/4)} = \frac{log\left(\frac{coth(u/2)}{coth(u_2/2)}\right)\left(\frac{cosh(2u)}{cosh(2u_1)}-1\right)}{\sqrt{2}log\left(\frac{coth(u/2)}{coth(u_2/2)}\right)sinh(2u)-cosh(2u)csch(u)} \tag{3.20}$$

At the boundaries u_1, u_2, R_T is zero, therefore it's more relevant to evaluate this quantity at the coordinate $u=u_3=0.5*(u_1+u_2)$, corresponding to the mid plane between the surfaces:

$$R_T(u_3,\pi/4)=\frac{log\left(\frac{coth(u_3/2)}{coth(u_2/2)}\right)\left(\frac{cosh(2u_3)}{cosh(2u_1)}-1\right)}{\sqrt{2}log\left(\frac{coth(u_3/2)}{coth(u_2/2)}\right)sinh(2u_3)-cosh(2u_3)csch(u_3)} \tag{3.21}$$

Figure 3.5 shows a contour plot of the absolute value of R_T at the point (u=u_3, v=π/4), as a function of u_1 and u_2. These graphs show that for values of u_1 and u_2 in the *low-impedance zone* (see Figure 3.4), the longitudinal component is more than 2000 times smaller than the transversal component.

On the other hand, notice that:

$$E_v(u,0)=E_v(u,\pi/2)=0 \tag{3.22}$$

This means that on the axis of symmetry (v=0) and at the beginning of the coaxial transmission line (v=π/2), the longitudinal component of the electric field vanishes. The consequence of this is that, even though a longitudinal component exists at the RTL, it will vanish at the input of the coaxial transmission line, which will be excited with a pure TEM wave.

3.5. ONE-DIMENSIONAL SIMPLIFICATION

In this Section, we derive a simplified and more manageable version for the equations for the electric field.

The complexity of the equations originates mainly from the impossibility to find a one-dimensional solution for the potential function **Φ**, as the Laplace equation is not simple separable in the IPS system.

$$\Phi(u,v)=\frac{V_1}{k_1}log\left(k_3coth\left(\frac{u}{2}\right)\right)\sqrt{\frac{cosh^2(u)-sin^2(v)}{cosh^2(u_1)-sin^2(v)}} \tag{3.23}$$

However, taking a closer look to the v dependent factor in Equation (3.23), it can be concluded that, if u~ u_2, the following approximation applies:

$$\sqrt{\frac{cosh^2(u)-sin^2(v)}{cosh^2(u_2)-sin^2(v)}}\approx\frac{cosh(u)}{cosh(u_2)} \tag{3.24}$$

And the potential could be rewritten as a one-dimensional function:

$$\Phi(u)=\frac{V_1cosh(u)}{k_1k_2}log\left(k_3coth\left(\frac{u}{2}\right)\right) \tag{3.25}$$

Using this approximation, the electric field can be calculated as:

$$E_u(u,v) = -\left(\frac{1}{\sqrt{g_{11}}}\frac{\partial\Phi(u)}{\partial u}\right)e^{-jkR(v)} \tag{3.26}$$

$$E_u(u,v) = \frac{V_1}{ak_1k_2\sqrt{2}}\frac{(\cosh(2u)+\cos(2v))}{\sqrt{\cosh(2u)-\cos(2v)}}\left(\coth(u) - \log\left[k_3\coth\left(\frac{u}{2}\right)\right]\sinh(u)\right)e^{-jkR(v)} \tag{3.27}$$

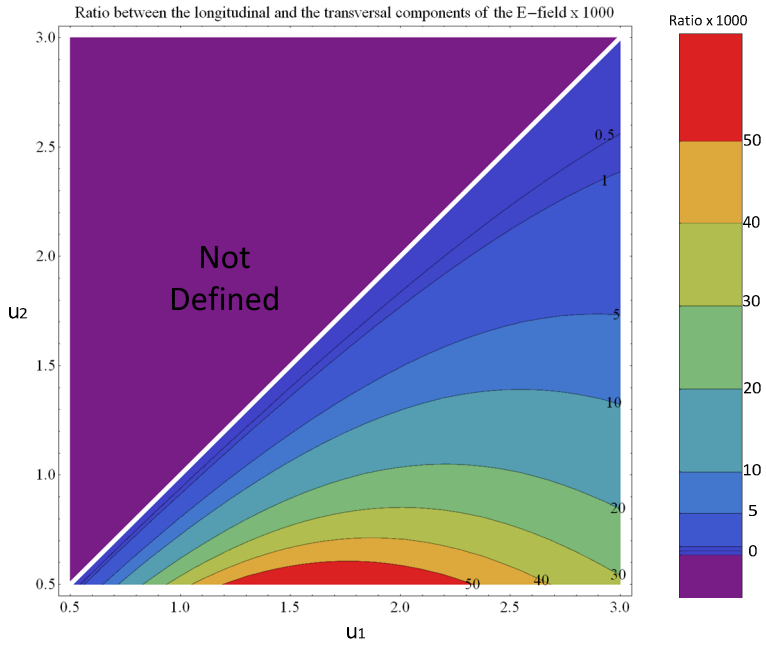

Figure 3.5 Ratio between the longitudinal and the transversal components of the electric field per 1000. Notice that in the zone of interest (low-impedance zone) the transverse component is about 2000 times bigger than the longitudinal component.

The maximum percent error between the complete and the approximated potential functions described by Equations (3.23) and (3.25) respectively, can be calculated by:

$$err = \frac{\Phi(u,v)-\Phi(u)}{\Phi(u,v)}\times 100\% = \frac{\sqrt{\frac{\cosh^2(u_1)-\sin^2(v)}{\cosh^2(u_2)-\sin^2(v)}} - \frac{\cosh(u_1)}{\cosh(u_2)}}{\sqrt{\frac{\cosh^2(u_1)-\sin^2(v)}{\cosh^2(u_2)-\sin^2(v)}}}\times 100\% \tag{3.28}$$

notice that *err* maximizes when $v=\pi/2$:

$$err_{\max} < \frac{\sqrt{\frac{\cosh^2(u_1)-1}{\cosh^2(u_2)-1}} - \frac{\cosh(u_1)}{\cosh(u_2)}}{\sqrt{\frac{\cosh^2(u_1)-1}{\cosh^2(u_2)-1}}} \times 100\% = \left(1 - \tanh(u_2)\coth(u_1)\right) \times 100\% \tag{3.29}$$

Figure 3.6 shows a contour plot of the maximum percent error as a function of u_1 and u_2, calculated using Equation (3.29). Notice that the 5% zone error stretches out as u_1 and u_2 decrease. However, the 5% zone covers the *low-impedance zone* of interest of our study. A similar graph can be obtained if the error between the exact (3.17) and approximated expressions (3.27) for the electric field is computed.

We can conclude that, in an IPS-RTL with a low-impedance at the coaxial end, the longitudinal component of the electric field can be neglected. Furthermore, the potential function can be simplified, providing a more compact expression for the transverse component of the electric field. The percent error produced by the proposed approximation is less than 5%.

3.6. MAGNETIC FIELD DISTRIBUTION

The magnetic field can be derived from the curl of the electric field. We consider the expression for the transverse electric field obtained from the one-dimensional approximation:

$$H(u,v) = -\frac{\nabla \times E}{j\omega\mu} = -\frac{1}{j\omega\mu}\begin{bmatrix} \frac{\hat{u}}{\sqrt{g_{22}g_{33}}} & \frac{\hat{v}}{\sqrt{g_{11}g_{33}}} & \frac{\hat{w}}{\sqrt{g_{11}g_{22}}} \\ \frac{\partial}{\partial u} & \frac{\partial}{\partial v} & \frac{\partial}{\partial w} \\ \sqrt{g_{11}}E_u(u,v) & 0 & 0 \end{bmatrix} = \frac{1}{j\omega\mu}\sqrt{\frac{1}{g_{11}g_{22}}}\frac{\partial}{\partial v}\left(\sqrt{g_{11}}E_u(u,v)\right)\hat{w} \tag{3.30}$$

where $E_u(u,v)$ is given by Equation (3.26)

$$H_w(u,v) = -\frac{1}{j\omega\mu}\sqrt{\frac{1}{g_{11}g_{22}}}\frac{\partial}{\partial v}\left(\frac{\partial \Phi(u)}{\partial u}e^{-jkR(v)}\right) \tag{3.31}$$

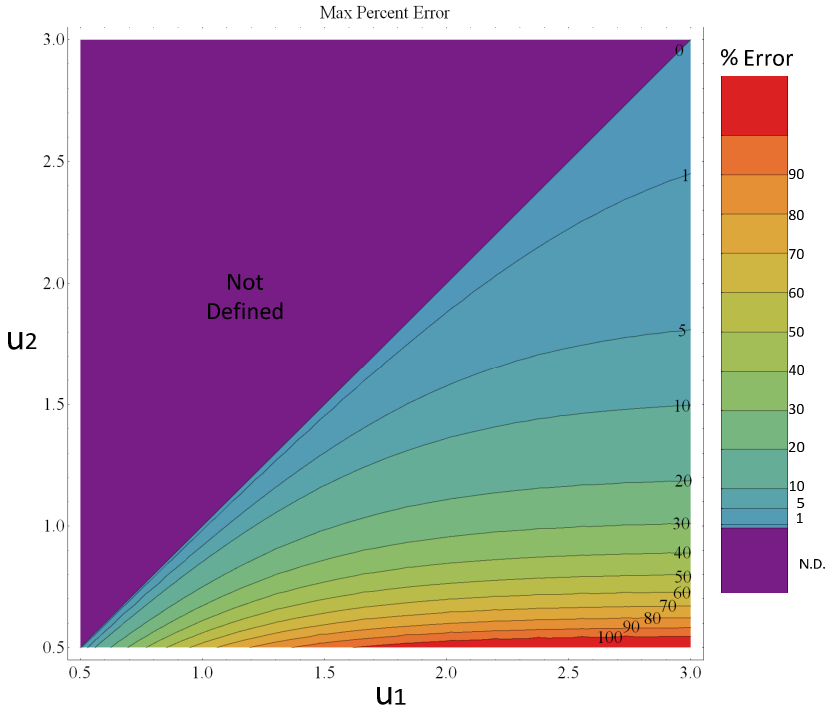

Figure 3.6 Contour Plot of the percent error between approximation and the full model of the potential function, as function of u_1 and u_2. Notice that the 5% zone error stretches as u_1 and u_2 decreases.

The metric coefficient g_{11} and g_{22} being equal, we obtain

$$H_w(u,v) = -\frac{1}{j\omega\mu}\frac{1}{g_{22}}\frac{\partial\Phi(u)}{\partial u}\frac{\partial}{\partial v}\left(e^{-jkR(v)}\right) \tag{3.32}$$

Taking the derivative of the exponential term leads to:

$$H_w(u,v) = \frac{k}{\omega\mu}\frac{1}{g_{22}}\frac{\partial\Phi(u)}{\partial u}\frac{\partial R(v)}{\partial v}e^{-jkR(v)} \tag{3.33}$$

The factor $R(v)$ given by Equation (3.12) is the distance traveled by the wave from the symmetry axis:

$$H_w(u,v) = \frac{k}{\omega\mu}\frac{1}{g_{22}}\frac{\partial\Phi(u)}{\partial u}\sqrt{g_{22}}e^{-jkR(v)} \tag{3.34}$$

$$. H_w(u,v) = \frac{k}{\omega\mu}\frac{1}{\sqrt{g_{22}}}\frac{\partial\Phi(u)}{\partial u}e^{-jkR(v)} . \tag{3.35}$$

Replacing Equation (3.26) into (3.35) yields

$$H_w(u,v) = \sqrt{\frac{\varepsilon}{\mu}} E_u(u,v) \tag{3.36}$$

This equation corresponds to the typical relationship between the electric and magnetic fields in TEM lines. If the interelectrodic space has $\varepsilon_r = \mu_r = 1$, the expression for the magnetic field is given by:

$$H_w(u,v) = \frac{120\pi V_1}{ak_1k_2\sqrt{2}} \frac{\left(cosh(2u)+cos(2v)\right)}{\sqrt{cosh(2u)-cos(2v)}} \left(coth(u) - log\left(k_3 Coth\left(\frac{u}{2}\right)\right) sinh(u) \right) e^{-jkR(v)} \tag{3.37}$$

3.7. CHARACTERISTIC IMPEDANCE

The characteristic impedance of the RTL can be calculated as the ratio between the incident voltage and current waves on the line:

$$Z_0(u,v) = \frac{V_i(u,w)}{I_i(v,w)} \tag{3.38}$$

The voltage can be obtained as the line integral of the electric field between the electrodes. The path of integration can be defined along a curve of constant *v*:

$$V_i(u,w) = \int_{u_2}^{u_1} E_u(u,v).dl_u = \int_{u_2}^{u_1} E_u(u,v)\sqrt{g_{11}}du = \left(\Phi(u_2) - \Phi(u_1)\right) e^{-jkR(v)} = V_1 e^{-jkR(v)} \tag{3.39}$$

While the current wave is obtained by integrating the magnetic field around the inner conductor:

$$I_i(u,w) = \oint_w H.dl_w = \int_0^{2\pi} H_w(u,v)\sqrt{g_{33}}dw = 2\pi H_w(u,v)\sqrt{g_{33}} \tag{3.40}$$

Taking into account the magnetic field defined by Equation (3.35), the expression for the characteristic impedance reads:

$$Z_0(u,v) = \frac{\int_{u_2}^{u_1} E_u\sqrt{g_{11}}du}{\int_0^{2\pi} H_w\sqrt{g_{33}}dw} = \frac{\int_{u_2}^{u_1} E_u\sqrt{g_{11}}du}{\int_0^{2\pi} \sqrt{\frac{\varepsilon}{\mu}} \frac{1}{\sqrt{g_{22}}} \frac{\partial\Phi(u)}{\partial u} e^{-jkR(v)} \sqrt{g_{33}}dw} \tag{3.41}$$

$$Z_0(u,v) = \frac{V_1 e^{-jkR(v)}}{2\pi\sqrt{\frac{\varepsilon}{\mu}} \frac{1}{\sqrt{g_{22}}} \frac{\partial\Phi(u)}{\partial u} \sqrt{g_{33}} e^{-jkR(v)}} \tag{3.42}$$

$$Z_0(u,v) = \frac{1}{2\pi}\sqrt{\frac{\mu}{\varepsilon}}\frac{\sqrt{g_{22}}}{\sqrt{g_{33}}}\frac{V_1}{\frac{\partial \Phi(u)}{\partial u}} \tag{3.43}$$

$$Z_0(u,v) = \frac{1}{2\pi}\sqrt{\frac{\mu}{\varepsilon}}\frac{\sqrt{g_{22}}}{\sqrt{g_{33}}}\frac{k_1 k_2}{\left(log\left(k_3 Coth\left(\frac{u}{2}\right)\right)sinh(u) - coth(u)\right)} \tag{3.44}$$

Notice that the radial distance R, measured from the axis of symmetry to the point (x, y, z) is related to square root of the metric coefficient g_{33}:

$$. R = \sqrt{x^2 + y^2} = \sqrt{2}a\frac{sinh(u)sin(v)}{cosh^2(u) - sin^2(v)} = \sqrt{2}\sqrt{g_{33}} \ . \tag{3.45}$$

Replacing this expression into Equation (3.44) permits to see the radial dependence of the impedance of the transmission line:

$$Z_0(u,v) = 60\frac{\sqrt{g_{22}}}{\sqrt{2}R}\frac{k_1 k_2}{\left(log\left(k_3 coth\left(\frac{u}{2}\right)\right)sinh(u) - coth(u)\right)} \tag{3.46}$$

Finally, the analytical expression for the characteristic impedance of the RTL can be written as:

$$Z_0(u,v) = 60\sqrt{Csc[v]^2 + Csch[u]^2}\frac{k_1 k_2}{\left(Log\left[Coth\left[\frac{u}{2}\right]k_3\right]Sinh[u] - Coth[u]\right)} \tag{3.47}$$

Notice that this expression is independent from the scale factor a.

3.8. EXAMPLE

The derived analytical result is applied to the same example discussed in Chapter 2, for which a set of IPS electrodes was calculated. The inter electrodic space is d_{gap}=0.5 mm and the dimensions of the coaxial transmission line are r_o =16.5 mm and r_i=17.5 mm, which correspond to a characteristic impedance for the coaxial line of Z_{coax}=3.5 Ω.

The constants defining the profiles are:

$$u_1 = 1.10507, u_2 = 1.05837, a = 22.1783e-3$$

The characteristic impedance, calculated along the trajectory u=u_3 is shown in Figure 3.7. Note that Z_0 tends smoothly to the characteristic impedance of the coaxial line.

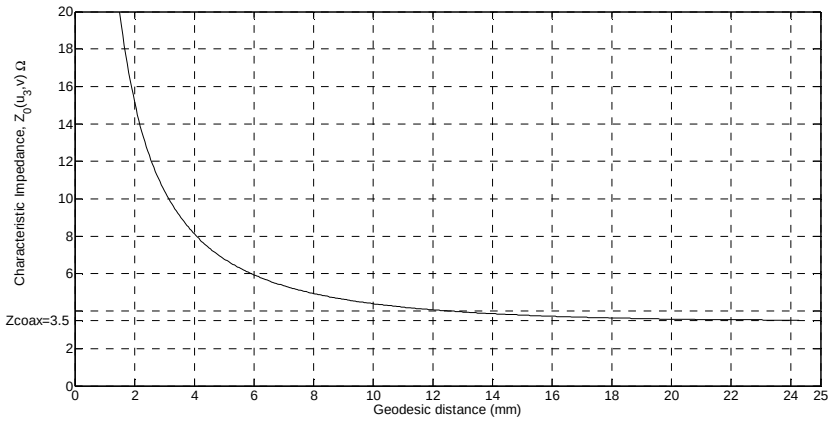

Figure 3.7 Characteristic impedance of the IPS-RTL example vs. geodesic distance ($R(v)$)

3.9. CONCLUSIONS

In this chapter, we derived analytical expressions for the harmonic electric and magnetic fields within the IPS-RTL of the SWO.

A one-dimensional approximation for the potential and the fields was derived. This approximation was shown to be accurate for typical SWOs for which the characteristic impedance of the coaxial line is very low (lower than 5 Ohms or so).

The one-dimensional approximation permits the treatment of the IPS-RTL as a TEM transmission line, whose characteristic impedance was obtained in a closed-form analytical expression.

REFERENCES

[1] D. V. Giri, *et al.*, "Switched Oscillators and Their Integration Into Helical Antennas," *Plasma Science, IEEE Transactions on*, vol. 38, pp. 1411-1426, 2010.

[2] R. E. Collin, *Field theory of guided waves*, 2nd ed. New York: Wiley-Interscience, 1991.

[3] P. Moon and D. E. Spencer, *Field Theory Handbook: Including Coordinate Systems, Differential Equations and Their Solutions* 2ed.: Springer-Verlag, 1971.

[4] M. Armanious, *et al.*, "Electrostatic field management and electrodynamic modeling of switched quarter-wave oscillators," *Dielectrics and Electrical Insulation, IEEE Transactions on*, vol. 18, pp. 1054-1065, 2011.

[5] M. Armanious, *et al.*, "Interaction Between Geometric Parameters and Output Waveforms in High-Power Quarter-Wave Oscillators," *Plasma Science, IEEE Transactions on*, vol. 38, pp. 1124-1131, 2010.

[6] J. W. Burger, *et al.*, "Modular Low Frequency High Power Microwave Generator," presented at the AMEREM, Annapolis M.D, USA, 2002.

[7] F. Santamaria, *et al.*, "Switched Oscillator: Parameter Effects on the Generated Signals," *Plasma Science, IEEE Transactions on,* vol. 40, pp. 3433-3441, 2012.

CHAPTER 4

ELECTRODYNAMIC ANALYSIS OF A SWITCHED OSCILLATOR CONNECTED TO A FREQUENCY DEPENDENT LOAD

4.1. INTRODUCTION

We investigate in this chapter the behavior of a switched oscillator (SWO) connected to an antenna with arbitrary frequency dependent response. The analysis is performed using an approach based on the chain-parameter technique [1][1], proposed by the author in [2].

The SWO is regarded as a frequency dependent two-port network, where the input signal is the transient voltage generated at the spark gap ($V_{SG}(f)$) and the output signal is the voltage at the input of the antenna ($V_A(f)$). The ratio between these two quantities is the voltage transfer function of the SWO:

$$T_{swo}(f) = \frac{V_A(f)}{V_{SG}(f)} \tag{4.1}$$

In this chapter, we will describe the procedure to evaluate the transfer function $T_{SWO}(f)$ starting from the geometry of the system and from the input impedance of the antenna.

The radiated signal can also be calculated using a similar approach. The antenna is considered as a second two-port network, over which the transfer function of the antenna ($T_A(f)$) is calculated as the ratio between the field radiated at certain distance and direction from the antenna ($E_r(f,r,\theta,\phi)$) and the voltage applied at the input of the antenna ($V_A(f)$):

$$T_A(f) = \frac{\vec{E}(f,r,\theta,\phi)}{V_A(f)} \tag{4.2}$$

The total transfer function of the system ($T(f,r,\theta,\phi)$), relating the radiated field and the voltage produced at the spark gap can be therefore calculated as:

$$T(f,r,\theta,\phi) = T_A(f,r,\theta,\phi)T_{SWO}(f) \tag{4.3}$$

4.2. BACKGROUND

Consider the geometry of the SWO proposed in Figure 4.1, consisting of a self-breaking spark gap followed by a low-impedance coaxial transmission line, an (optional) DC-blocking capacitor, and a frequency dependent antenna (in this case a monopole).

An equivalent transmission line circuit diagram of this geometry is presented in Figure 4.2.

[1] Also known as transmission or ABCD parameters.

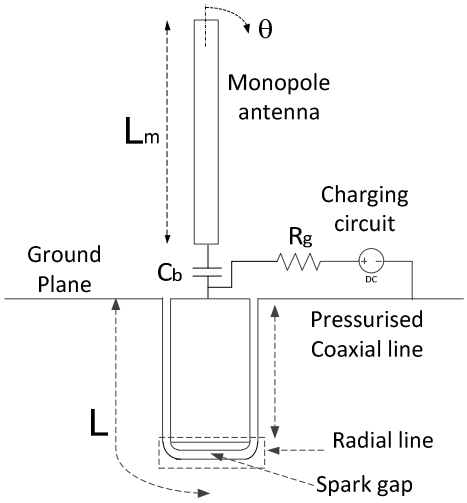

Figure 4.1 A monopole antenna integrated into a SWO

For the case of the present work, the electrodes of the spark gap forming the Radial Transmission Line (RTL) are designed using the Inverse Prolate Spheroid (IPS) coordinate system, described in Chapter 2.

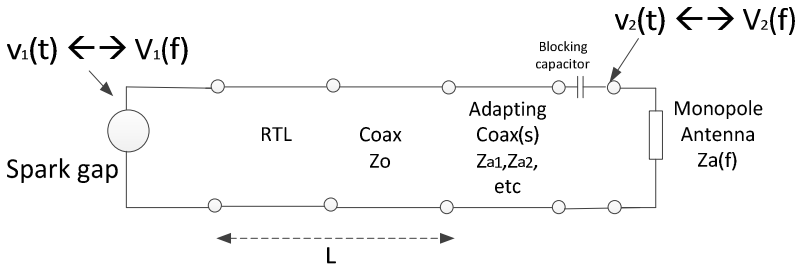

Figure 4.2 Transmission line system representing the SWO

The effects of the RTL formed by the electrodes on the performance of the SWO were considered by Giri *et al.* in [3], where the behavior of a coaxial SWO connected to a helical antenna was presented. In their analysis, the RTL was modeled using a series of cascaded uniform transmission lines. The response of the system was obtained by simulations using traditional circuit codes. The model of Giri *et al.* [3] yielded accurate results in predicting the central frequency and the quality factor *Q* of the SWO. Note that in the analysis of Giri *et al.*, the helical antenna was represented by a constant, real impedance. A similar assumption was also made by Armanious *et al.* in [4], when considering the connection of a monocone antenna to an SWO. It is important to realize that this assumption is only valid for a set of frequencies at which the input impedance of the broadband antenna, such as helices or monocones exhibit a low reactance and an almost con-

stant resistance. However, if a narrowband antenna is connected to an SWO, the accurate simulation of the system requires taking into account the frequency dependence of the input impedance of the antenna. Note that the work of Armanious *et al.* [4] was based on a full-wave analysis in which the frequency dependence of the antenna can in principle be taken into account.

4.3. CHAIN (ABCD) MATRIX REPRESENTATION OF THE SWO

The ABCD parameters of a two-port network can be defined using the diagram presented in Figure 4.3 [1].

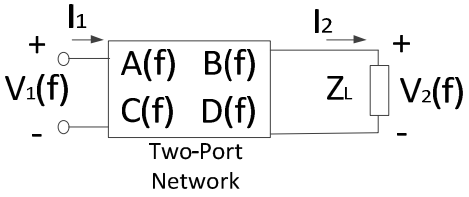

Figure 4.3 ABCD representation of a two-port network. $V_1(f)$, $I_1(f)$ are, respectively, the input voltage and current, $V_2(f)$, $I_2(f)$ are respectively the output voltage and current, $Z_L(f)$ is the load impedance. All the terms are frequency dependent

The input and output parameters of the network are related by the equation:

$$\begin{bmatrix} V_1(f) \\ I_1(f) \end{bmatrix} = \begin{bmatrix} A(f) & B(f) \\ C(f) & D(f) \end{bmatrix} \begin{bmatrix} V_2(f) \\ I_2(f) \end{bmatrix} \tag{4.4}$$

where:
- $V_1(f)$, $I_1(f)$ are, respectively, the input voltage and current,
- $V_2(f)$, $I_2(f)$ are respectively the output voltage and current,
- $Z_L(f)$ is the load impedance.

All the terms are frequency dependent.

The voltage at the output ($V_2(f)$) and the voltage transfer function ($T_{SWO}(f)$) can be obtained as:

$$V_2(f) = T_{SWO}(f) V_1(f) = \frac{Z_L(f) V_1(f)}{Z_L(f) A(f) + B(f)} \tag{4.5}$$

This approach can be advantageously applied to the analysis of the SWO. The system (RTL + coaxial transmission line + antenna) is represented as a cascade of two-port networks, each one characterized by its chain parameters, as illustrated in Figure 4.4. On this diagram, V_{SG} is the voltage produced by the spark gap, Z_g is the spark gap impedance, V_A is the input voltage on the antenna terminals, C_b is a (optional) blocking capacitor, $Z_A(f)$ is the input impedance of the antenna, $R_A(f)$ is the real part of the impedance of the antenna and $X_A(f)$ is the reactance of the antenna.

After calculating the resulting overall ABCD matrix, $T_{SWO}(f)$ and $V_A(f)$ can be obtained from Equation (4.5). The time domain voltage at the entrance of the antenna can then be obtained by an inverse Fourier transformation.

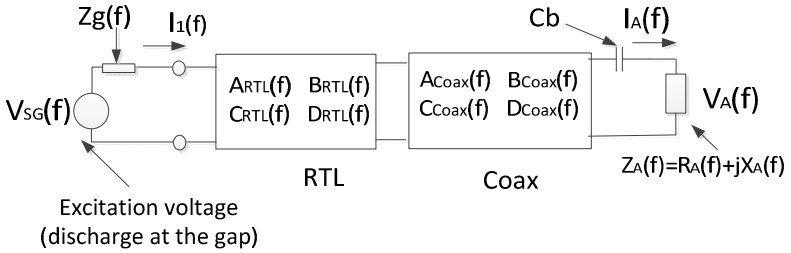

Figure 4.4 Representation of the SWO using the cascade of the two-port networks characterized by their ABCD matrices.

4.3.1. ABCD PARAMETERS OF THE COAXIAL TRANSMISSION LINE

The ABCD matrix of the coaxial transmission line is given by [5]

$$\begin{bmatrix} A_{Coax}(f) & B_{Coax}(f) \\ C_{Coax}(f) & D_{Coax}(f) \end{bmatrix} = \begin{bmatrix} \cosh(j\beta L_{Coax}) & Z_{Coax}\sinh(j\beta L_{Coax}) \\ \dfrac{\sinh(j\beta L_{Coax})}{Z_{Coax}} & \cosh(j\beta L_{Coax}) \end{bmatrix} \tag{4.6}$$

where:
- L_{Coax}, is the length of the coaxial,
- $\beta=2\pi f/v_p$,
- f is the frequency,
- v_p is the propagation velocity.

4.3.2. ABCD PARAMETERS OF THE RTL

As discussed in Chapter 3, the IPS-RTL is a non-uniform transmission line (NUTL), having a characteristic impedance:

$$Z_0(u_3, v) = 60\sqrt{\csc[v]^2 + \csc h[u_3]^2}\,\frac{k_1 k_2}{\left(\ln\left(Coth\left(\frac{u_3}{2}\right)k_3\right)\sinh(u_3) - \coth(u_3)\right)} \tag{4.7}$$

where:
- k_1 ,k_2 and k_3 are constant terms:

$$k_1 = \ln\left(\frac{\coth\left(\frac{u_1}{2}\right)}{\coth\left(\frac{u_2}{2}\right)}\right) \qquad k_2 = \cosh(u_1) \qquad k_3 = \frac{1}{\coth\left(\frac{u_2}{2}\right)} \tag{4.8}$$

- u_1, u_2, are the constants defining the profile of the electrodes,
- v is the angular parameter, see Chapter 2 for details.
- $Z_0(u_3,v)$ is calculated along a *u-curve*, lying in the mid-plane between the electrodes, this corresponds to the *u*-coordinate: $u_3=(u_2+u_1)/2$

In order to calculate its ABCD parameters, the line is sub-divided into *N* segments, the impedance of each segment is considered constant and the overall ABCD matrix is obtained by multiplying the cascaded ABCD matrices of the segments. This is analogous to the procedure for the calculation of NUTL presented by Protonotarios and Wing in [6].

The ABCD matrix of the *n-th* segment of the RTL is given by [1]:

$$\begin{bmatrix} A_n(f) & B_n(f) \\ C_n(f) & D_n(f) \end{bmatrix} = \begin{bmatrix} \cosh(j\beta\Delta L) & Z_{0n}(f)\sinh(j\beta\Delta L) \\ \frac{\sinh(j\beta\Delta L)}{Z_{0n}(f)} & \cosh(j\beta\Delta L) \end{bmatrix} \tag{4.9}$$

where:
-$Z_{0n}(j\beta\Delta L)$ is the characteristic impedance of the segment,
-ΔL is the length of the segment[2].

The resulting ABCD matrix of the RTL is

$$\begin{bmatrix} A_{RTL}(f) & B_{RTL}(f) \\ C_{RTL}(f) & D_{RTL}(f) \end{bmatrix} = \prod_{n=1}^{N} \begin{bmatrix} A_n(f) & B_n(f) \\ C_n(f) & D_n(f) \end{bmatrix} \tag{4.10}$$

where the matrix Π operator is defined as [6]:

$$\prod_{n=1}^{m} \begin{bmatrix} A_n(f) & B_n(f) \\ C_n(f) & D_n(f) \end{bmatrix} = \begin{bmatrix} A_1(f) & B_1(f) \\ C_1(f) & D_1(f) \end{bmatrix} \times \begin{bmatrix} A_2(f) & B_2(f) \\ C_2(f) & D_2(f) \end{bmatrix} \times \ldots \times \begin{bmatrix} A_m(f) & B_m(f) \\ C_m(f) & D_m(f) \end{bmatrix} \tag{4.11}$$

4.4. VOLTAGE TRANSFER FUNCTION OF THE SWO

The total ABCD matrix of the SWO can be calculated as:

$$\begin{bmatrix} A_{Total}(f) & B_{Total}(f) \\ C_{Total}(f) & D_{Total}(f) \end{bmatrix} = \begin{bmatrix} 1 & Z_g(f) \\ 0 & 1 \end{bmatrix} \times \left(\prod_{n=1}^{m} \begin{bmatrix} A_n(f) & B_n(f) \\ C_n(f) & D_n(f) \end{bmatrix} \right) \times \begin{bmatrix} A_{Coax}(f) & B_{Coax}(f) \\ C_{Coax}(f) & D_{Coax}(f) \end{bmatrix} \times \begin{bmatrix} 1 & \frac{1}{j2\pi f C_b} \\ 0 & 1 \end{bmatrix} \tag{4.12}$$

where $Z_g=R_g+jX_g$ is the impedance of the spark gap[3].

---

[2] Note that it is not necessary for the segments to be equal; however, this facilitates the computation of the parameters.

The last matrix corresponds to the blocking capacitor, an optional element inserted between the antenna and the SWO.

The relationship between the input and output voltages and currents can be therefore calculated using:

$$\begin{bmatrix} V_{SG}(f) \\ I_{SG}(f) \end{bmatrix} = \begin{bmatrix} A_{Total}(f) & B_{Total}(f) \\ C_{Total}(f) & D_{Total}(f) \end{bmatrix} \begin{bmatrix} V_A(f) \\ I_A(f) \end{bmatrix} = \begin{bmatrix} A_{Total}(f) & B_{Total}(f) \\ C_{Total}(f) & D_{Total}(f) \end{bmatrix} \begin{bmatrix} V_A(f) \\ \frac{V_A(f)}{Z_A(f)} \end{bmatrix} \tag{4.13}$$

where the resulting ABCD parameters are:

$$A_{Total}(f) = (A_{RTL}(f) + C_{RTL}Z_g)\cosh(j\beta L_{Coax}) + \frac{(B_{RTL}(f) + D_{RTL}(f)Z_g)\sinh(j\beta L_{Coax})}{Z_{coax}} \tag{4.14}$$

$$\begin{aligned} B_{Total}(f) &= \left(B_{RTL}(f) + D_{RTL}(f)Z_g\right)\cosh\left(j\beta L_{Coax}\right) \\ &+ \left(Z_{coax}\left(A_{RTL}(f) + C_{RTL}(f)Z_g\right)\right)\sinh\left(j\beta L_{Coax}\right) + Z_{BC}A_{Total}(f) \end{aligned} \tag{4.15}$$

$$C_{Total}(f) = C_{RTL}(f)\cosh(j\beta L_{Coax}) + \frac{D_{RTL}(f)\sinh(j\beta L_{Coax})}{Z_{coax}} \tag{4.16}$$

$$D_{Total}(f) = (Z_{BC}C_{RTL} + D_{RTL})\cosh(j\beta L_{Coax}) + \left(\frac{Z_{BC}D_{RTL}}{Z_{coax}} + C_{RTL}Z_{coax}\right)\sinh(j\beta L_{Coax}) \tag{4.17}$$

The voltage on the antenna can be determined as:

$$V_A(f) = \frac{Z_A(f)V_{SG}(f)}{Z_A(f)A_{Total}(f) + B_{Total}(f)} \tag{4.18}$$

The voltage transfer function of the SWO is defined by:

$$T_{SWO}(f) = \frac{V_A(f)}{V_{SG}(f)} = \frac{Z_A(f)}{Z_A(f)A_{Total}(f) + B_{Total}(f)} \tag{4.19}$$

4.5. EIGENFREQUENCIES OF THE SWO

In [6], Protonotarios and Wing showed that the eigenfrequencies of a NUTL are related to the zeros of its ABCD parameters. Note that we are referring to the natural frequencies, or eigenfrequencies of the SWO, which are intrinsic properties of the device itself and are independent of the loads connected at the ends of

[3] It is worth noting that nonlinear effects were disregarded in the analysis. In Appendix 1, a time-domain model is presented in which such effects are included.

the device (which in this case correspond to the antenna and the impedance of the gap).

In particular, the eigenfrequencies of a NUTL terminated at one end by a short circuit and at the other end by an open circuit, are the frequencies (f_0, f_1, f_2,…. ,f_N) where the parameter $A(f)$ vanishes.

At these frequencies we have:

$$A_{Total}(f_N)=0= \\ \left(A_{RTL}(f_N)+C_{RTL}(f_N)Z_g\right)\cosh\left(j\frac{2\pi f_N L_{Coax}}{v_p}\right)+\frac{\left(B_{RTL}(f_N)+D_{RTL}(f_N)Z_g\right)}{Z_{coax}}\sinh\left(j\frac{2\pi f_N L_{Coax}}{v_p}\right) \tag{4.20}$$

From which the eigenfrequencies can be calculated as the roots of the equation:

$$j\tan\left(\frac{2\pi f_N L_{Coax}}{v_p}\right)+Z_{coax}\frac{A_{RTL}(f_N)+C_{RTL}(f_N)Z_g}{B_{RTL}(f_N)+D_{RTL}(f_N)Z_g}=0 \tag{4.21}$$

If $Z_g = 0$ we have:

$$f_N=\frac{v_p}{2\pi L_{Coax}}\arctan\left[jZ_{Coax}\frac{A_{RTL}(f_N)}{B_{RTL}(f_N)}\right]+N\pi \tag{4.22}$$

where N is an integer.

If the losses in the system are negligible, the term $B_r(f)$ is an imaginary term and Equation (4.22) results in a real number.

For a given first resonance frequency f_0, the length of the coaxial line can be calculated

$$L_{Coax}=\frac{v_p}{2\pi f_o}\arctan\left[jZ_{Coax}\frac{A_{RTL}(f_0)}{B_{RTL}(f_0)}\right] \tag{4.23}$$

This equation permits an initial dimensioning of L_{Coax} during the design phase, having in mind that the obtained value is an approximation and further adjustment of the length of the coaxial line might be necessary.

If Z_g is different from zero, the roots of Equation (4.21) are complex and the eigenfrequencies are complex, indicating than a dumping factor exists in the SWO, even if ideal load conditions are considered.

Note that the natural frequency is not affected by the blocking capacitor.

It is worth noting that in the original idea presented by Baum in [7], the RTL was considered to be infinitely short ($A_r(f)=D_r(f)=1$, $B_r(f)=C_r(f)=0$) and Z_g was considered to be zero. In that context, the SWO was considered as a quarter-wave device:

$$L_{Coax} = \lim_{Br(f_0)\to 0} \frac{\lambda}{2\pi} \arctan\left[Z_{Coax} \frac{1}{B_r(f_0)} \right] = \frac{\lambda}{4} \tag{4.24}$$

4.6. SOURCE REPRESENTATION

As we mentioned in Section 4.5, the impedance of the spark gap influences the resonance frequency and voltage transfer function of the SWO. However, the integration of a full electro-dynamic model of the spark into the ABCD equivalent model requires taking into account the time-dependent spark gap resistance and inductance, which is a non-trivial task (see e.g.[8]).

In this chapter, we use the source model proposed in [9], which consists of a single source ($V_{SG}(f)$) placed at the spark gap end of the SWO. The waveform of $V_{SG}(f)$ presents a long risetime (hundreds of *ns* long) simulating the charging phase of the SWO, followed by a fast decay time (hundreds of *ps*) representing the closing of the switch (see Figure 4.5 for details).

The source is connected in series to a constant resistance R_g and a constant inductance L_g corresponding to the losses in the spark gap. The values of these parameters depend on the length of the gap, the electric field previous to the discharge, the type of gas, and the pressure. We use here the values proposed by Martin in [10].

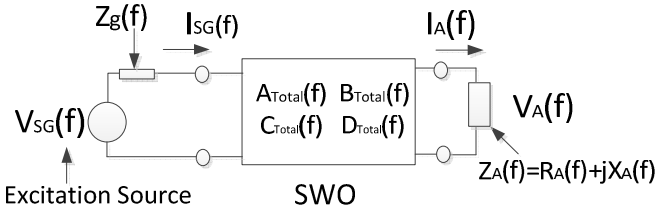

Figure 4.5 Excitation source model

The waveform representing $V_{SG}(f)$ was generated using a modified version of the function presented by Giri in [11]:

$$V_{SG}(f) = \left[\frac{V_o t_d}{(\beta + j2\pi f t_d)} e^{\frac{(\beta + j2\pi f t_d)^2}{4\pi}} \right]^* e^{-j2\pi t_s} \tag{4.25}$$

where:
- V_0 is the peak voltage,
- t_d is the closing time of the spark gap,
- $-\beta$ is a constant related to the charging time,
- t_s is the time at which the switch closes,
- f is the frequency,

and * is the conjugate operator.

Differently from other representations of double exponential signals, the time domain equivalent of Equation (4.25) is continuous for all time *t*.

As an example, Figure 4.6 presents the frequency-domain and time-domain representations of a wave with the following parameters:

β = *60e-3,* t_d*=1 ps,* V_o*= 40 kV,* t_s*=2000 ns*

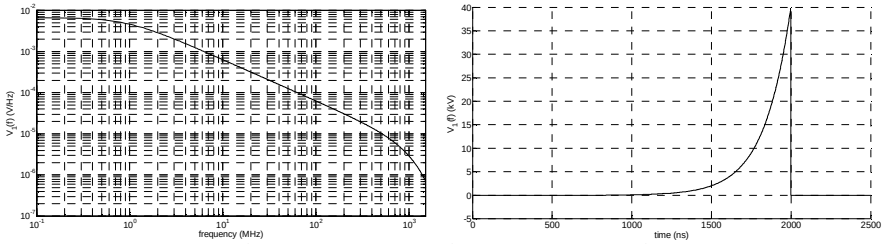

Figure 4.6 Example of excitation voltage in frequency domain (left) and time domain (right)

4.7. ANTENNA MODELING

We are interested in knowing the field radiated by the antenna at a certain distance and direction ($E(r,\phi,\theta)$). Using numerical simulation, it's possible to establish the transfer function of the antenna ($T_A(r, \phi, \theta, f)$), defined as the ratio between the radiated electric field and the voltage applied at the input of the antenna:

$$T_A(r,\theta,\phi,f) = \frac{E(r,\theta,\phi,f)}{V_{AX}(f)} \tag{4.26}$$

where $V_{AX}(f)$ is an arbitrary voltage at the input of the antenna. Notice that the radiated field in Equation (26) is not necessary the far field.

The field radiated by the antenna when connected to the SWO can then be calculated as:

$$E_{SWO}(r,\theta,\phi,f) = T_A(r,\theta,\phi,f)V_A(f) = T_A(r,\theta,\phi,f)V_{SG}(f)T(f) \tag{4.27}$$

$$E_{SWO}(r,\theta,\phi,f) = T_A(r,\theta,\phi,f)V_{SG}(f)\frac{Z_A(f)}{A(f)Z_A(f)+B(f)} \tag{4.28}$$

where: $V_A(f)$ is calculated using Equation (4.18) and $Z_A(f)$ is the input impedance of the antenna.

4.8. APPLICATION EXAMPLE

4.8.1. ABCD PARAMETERS

In this section we will illustrate the implementation of the proposed modeling approach to the design of an SWO that uses the RTL formed by the IPS electrodes derived in previous chapter.

The details of the design are:

- Intended resonance frequency: f_o=433 MHz
- Inter electrodic space: d_{gap}=0.5 mm
- Coaxial impedance: Z_{coax}=*3.5 Ω.*
- Radiuses of the Coaxial transmission line: r_o =16.5 mm and r_i=17.5 mm

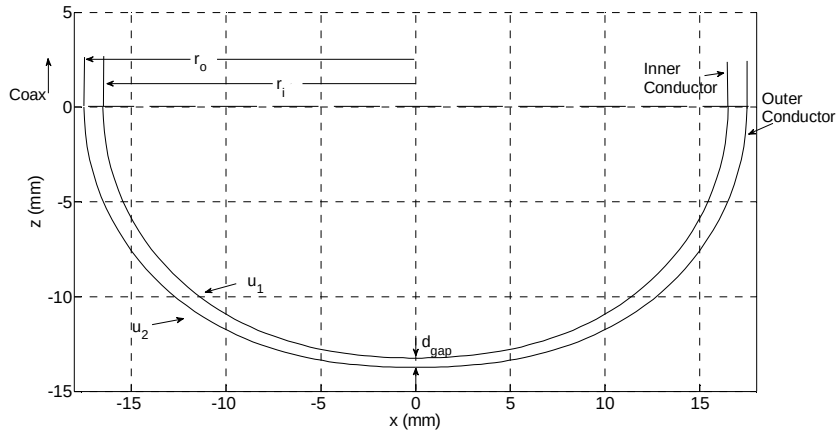

Figure 4.7 Profile of the electrodes proposed as example

The constants defining the profiles are:

$$u_1 = 1.10507, u_2 = 1.05837, a = 22.1783e-3$$

The profile of the electrodes corresponding to this design are presented in Figure 4.7

The length of the coaxial transmission line can be calculated from Equation (4.23). However, it is first necessary to segment the line and calculate the ABCD parameters of the resulting IPS-RTL.

The segmentation of the line implies finding the points v_s =(v_1,...., v_{N-1}), dividing the total length of the line into *N* segments of equal length ΔL.

The length of a segment of a *u-curve*, between the points v_A and v_B is:

$$R(u_3, v_A, v_B) = \int_{v_A}^{v_B} \sqrt{g_{22}}\, dv = \int_{v_A}^{v_B} a \sqrt{\frac{\sinh(u)^2 + \sin(v)^2}{\cosh(u)^2 - \sin(v)^2}}\, dv \tag{4.29}$$

The total length of the *u-curve* of the example is:

$$R\left(u_{3,0}, \frac{\pi}{3}\right) = \int_0^{\pi/2} \sqrt{\frac{\sinh(u)^2 + \sin(v)^2}{\cosh(u)^2 - \sin(v)^2}}\, dv = 24.33(mm) \tag{4.30}$$

The line was segmented into *N=50*, segments, the length of each one being:

$$\Delta L = 0.4866(mm) \tag{4.31}$$

This segmentation is done numerically, as the integral (4.29) does not possess analytical solution.

The segmented IPS-RTL can be seen in Figure 4.8.

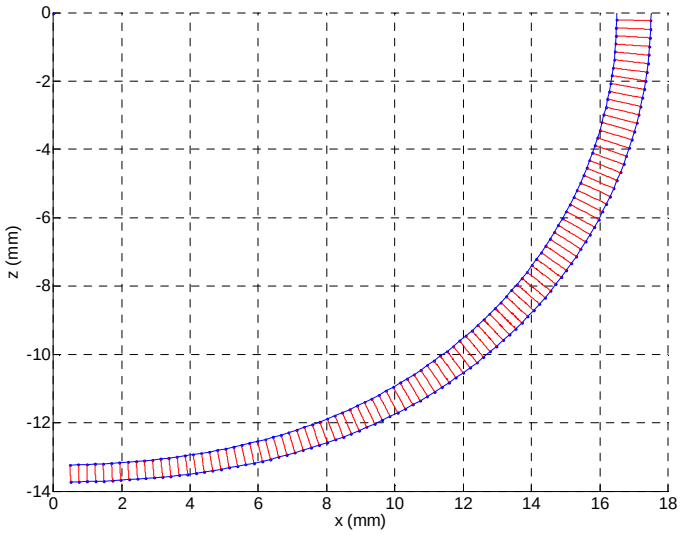

Figure 4.8 Segmented IPS-RTL

The variation of the impedance against the geodesic distance can be seen in Figure 4.9.

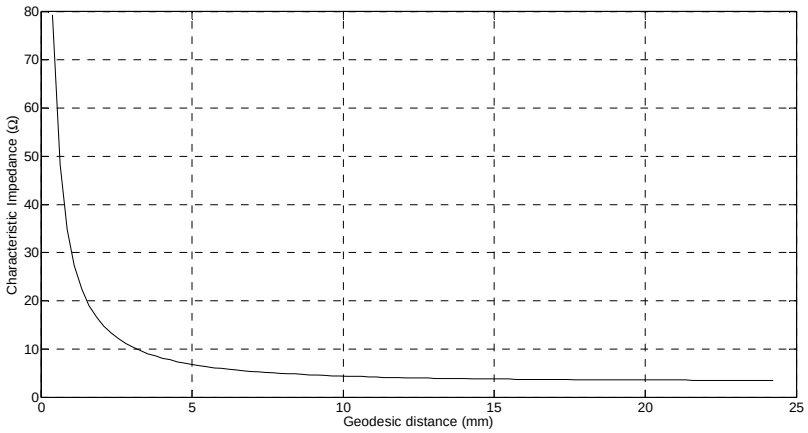

Figure 4.9 Characteristic impedance vs geodesic distance from the axis of symmetry

The A_{RTL}(f) and B_{RTL}(f) parameters of the IPS RTL vs. frequency can be seen in Figure 4.10.

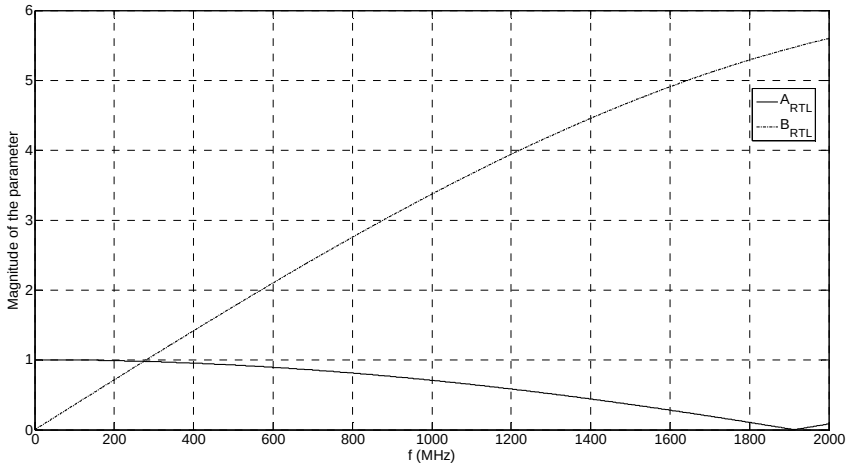

Figure 4.10 Magnitude of the A and B parameters of the IPS-RTL

Replacing the results obtained for the $A_{RTL}(f)$ and $B_{RTL}(f)$ parameters in Equation (4.22), the length of the coaxial line can be obtained:

$$L_{Coax} = 123.4(mm) \tag{4.32}$$

The resulting ABCD parameters of the ensemble RTL + coaxial line can be seen in Figure 4.11.

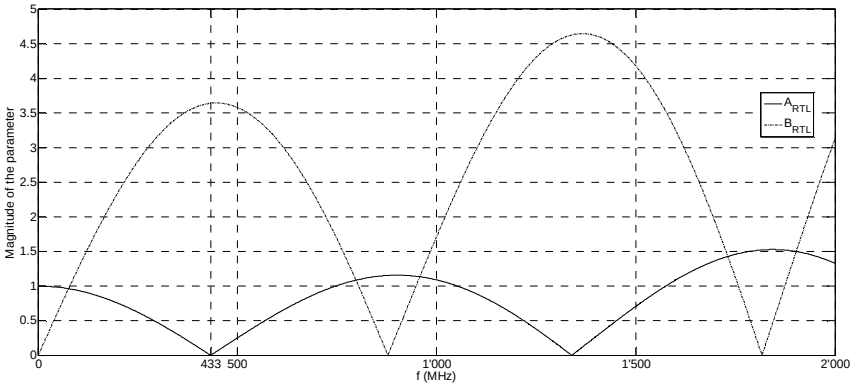

Figure 4.11 ABCD parameters of the RTL+coaxial line. notice the resonance frequency at 433 MHz.

4.8.2.Monopole Antenna

As explained in the introduction of this Chapter, the objective is to explore the response of an SWO connected to a frequency dependent antenna. We consider here the case of a monopole over a finite ground plane, as described in Figure 4.12. The monopole was dimensioned to be resonant at f_0, the resonance frequency of the SWO. The dimensions of the antenna for this case are: L_A=159 mm, D_A=5 mm, R_p=200 mm.

An electromagnetic simulation was performed in CST Microwave Studio®. A coaxial transmission line was connected at the entrance of the coaxial port of the antenna and a coaxial port was defined at the entrance of this line.

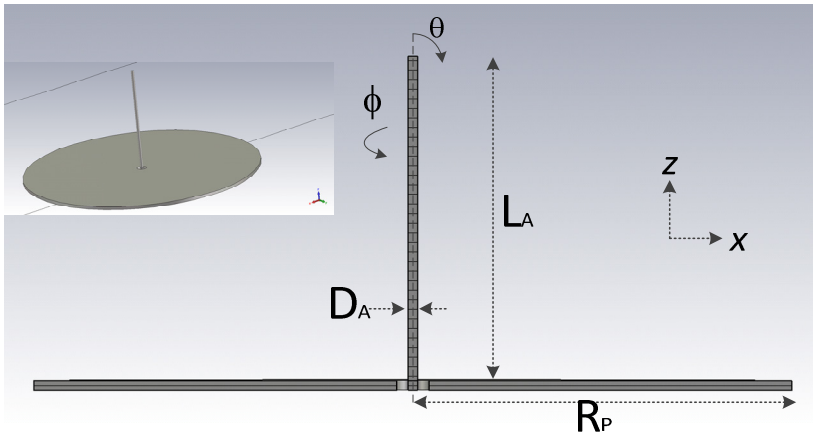

Figure 4.12 Model of the monopole over finite ground plane antenna simulated in CST. The dimensions of the antenna L_A=159 mm, D_A=5 mm, R_p=200 mm.

The impedance measured at the coaxial port was calculated and multiplied by the de-embedding factor of the transmission line, obtaining the value of the input impedance of the monopole, shown in Figure 4.13.

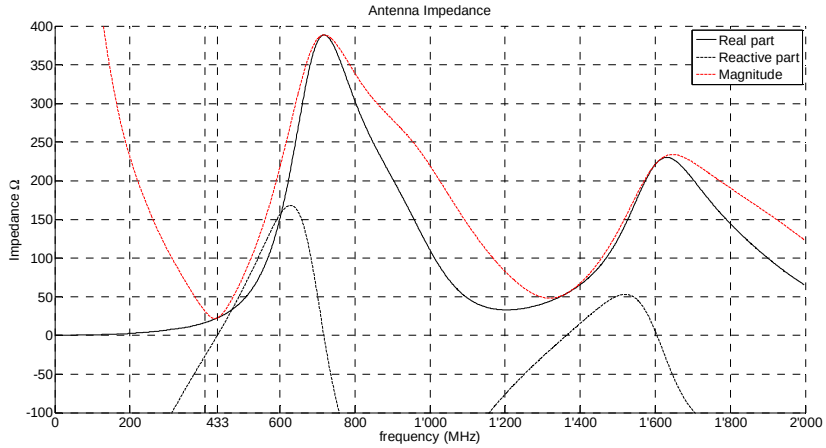

Figure 4.13 Input impedance of the monopole. Real part (black), imaginary part (dashed), absolute value (red). Notice the resonance frequency at 433 MHz.

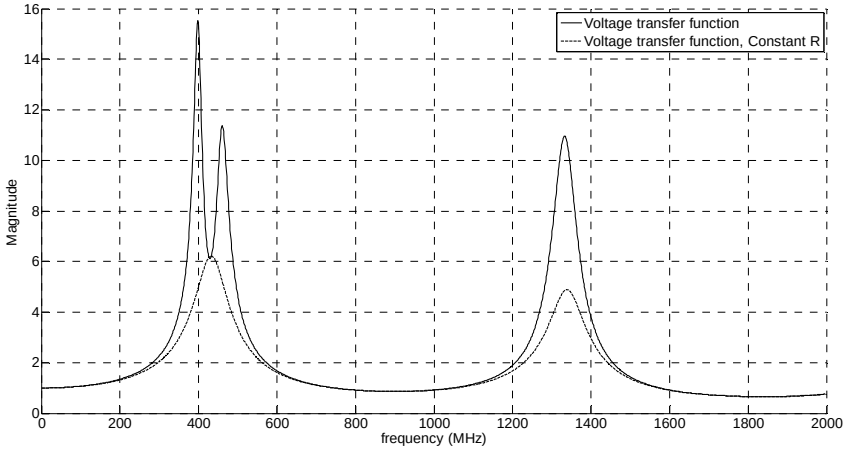

Figure 4.14 Voltage transfer function of the SWO using the monopole antenna shown in Figure 4.12 (solid line). Voltage transfer function using a constant load of 36 Ohms (dashed line).

The voltage transfer function ($T_{swo}(f)$), calculated according to Equation (4.19) is plotted in Figure 4.14. As it can be seen from the figure, the resonance frequency is not the intended frequency. Indeed, there is a dip at the exact frequency of resonance. As comparison, the voltage transfer function was calculated considering a real, constant load corresponding to the value of the input impedance of the monopole at the resonance frequency. This is shown in the same figure (Figure

4.14) where it can be seen a clear resonance at 433 MHz. Notice that both functions are equal at the resonance frequency. Note also the occurrence of a resonance at the second harmonic of the intended frequency.

A double exponential voltage wave with slow-rise and fast-decay time was applied as excitation, as explained in Section 4.6. The peak voltage is 10 kV. The rise time is 100 ns and the decay time is 500 ps. In a first attempt, the losses at the spark gap were considered to be zero. The source voltage in frequency domain ($V_{SG}(f)$) can be seen in Figure 4.15 . On the same figure, the output voltage at the antenna is also shown. The resulting time-domain voltage on the antenna is plotted in Figure 4.16.

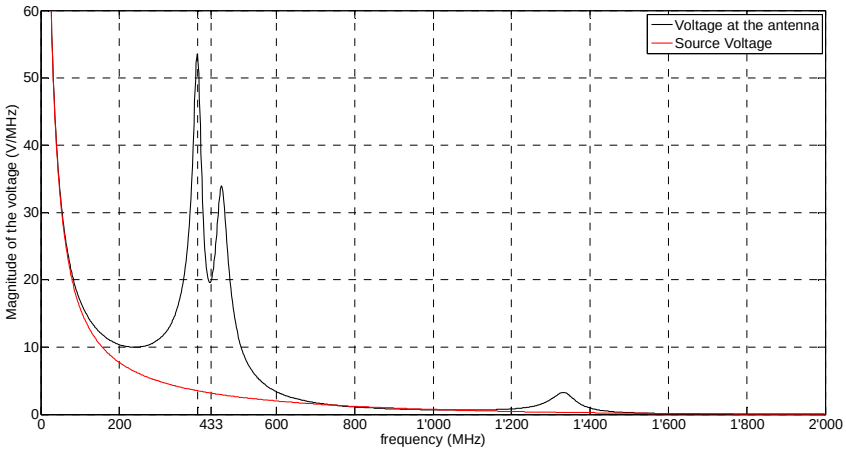

Figure 4.15 Voltage on the antenna (black) and source voltage (red)

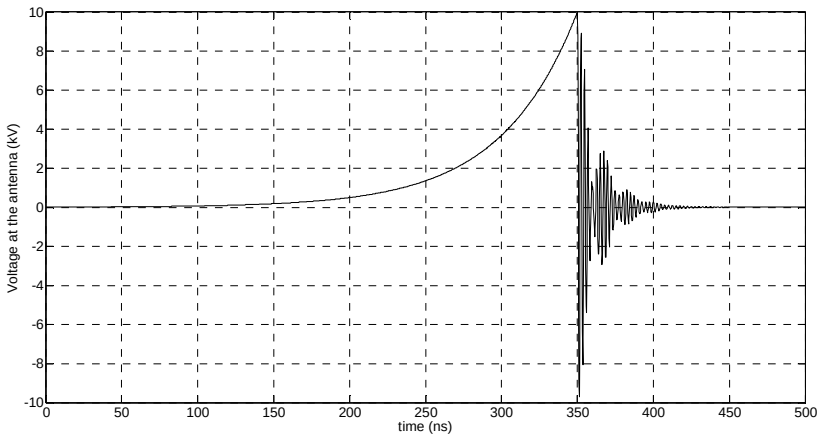

Figure 4.16 Voltage on the antenna in time domain

The dip at the resonance frequency (f_0) can be explained as follows: $X_A(f)$ is zero at the resonance frequency, however it grows (and hence $Z_a(f)$ grows) rapidly as

we move either above or below the resonance frequency. As a consequence, the mismatch between the antenna and the SWO at f_0 will be smaller than the mismatch at neighboring frequencies.

4.8.3. Energy balance

The validity of the model can be tested at this point by calculating the energy balance of the system, as follows. Before the discharge, the SWO can be assumed as a capacitance that gets charged by the source and acquires an amount of electrostatic energy (U_{DC}) given by:

$$U_{DC} = \frac{V_{SG_Peak}^2}{2C_{SWO}} \tag{4.33}$$

where:
V_{SG_Peak} is the maximum voltage at which the SWO is charged
C_{SWO} is the capacitance of the SWO

After the discharge, all this energy is dissipated by the antenna, if the losses in the spark-gap are zero.

The total capacitance of the SWO was calculated in Comsol® 2D-axis-symetric module:

$$C_{SWO} = 134\,pF \tag{4.34}$$

The electrostatic energy stored on the SWO previous to the discharge is:

$$U_{SWO} = \frac{V_{SG_Peak}^2 C_{SWO}}{2} = 6.7\,mJ \tag{4.35}$$

From *t > 350* ns the antenna starts radiating and, assuming that the spark is assumed lossless, all the radiated energy can be obtained as follows:

$$\begin{aligned} U_{Radiated} &= 2\int_0^\infty P_{AD}(f)\,df \\ U_{Radiated} &= \int_0^\infty \frac{V_{AD}(f)\overline{V}_{AD}(f)}{R_A(f)}\,df \end{aligned} \tag{4.36}$$

where $V_{AD}(f)$ is the Fourier transform of the voltage on the antenna after the discharge, in our case *t > 350 ns*, $\overline{V}_{AD}(f)$ is the complex conjugate of $V_{AD}(f)$ and $P_{AD}(f)$ is the power on the antenna after the discharge. $V_{AD}(f)$ and $P_{AD}(f)$ are shown in Figure 4.17.

The result of the evaluation of the integral shown in Equation (4.36) is:

$$U_{Radiated} = 6.1\ mJ \tag{4.37}$$

which is in agreement with Equation (4.35). From this result it can be said that, from the point of view of the energy balance, the method presented for the calculation of the voltage on the antenna is valid.

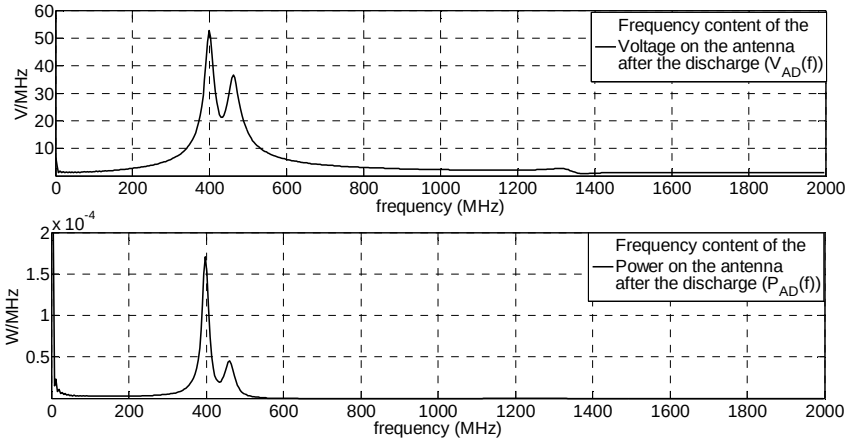

Figure 4.17 Voltage on the antenna after the discharge (top) and power on the antenna after of the discharge (bottom) vs. frequency. Notice that most of the frequency content is near the resonance.

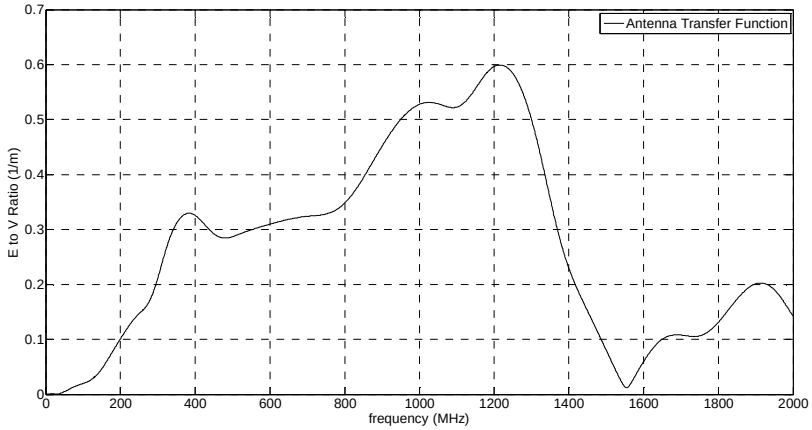

Figure 4.18 Antenna transfer function $T_A(f)$. Relationship between the vertical component of the far field and the voltage applied to the antenna. The field was computed at coordinates (ϕ=0°, θ=90°, r=1 m). See Figure 4.12 for reference.

4.8.4.Radiated field

The vertical component of the far field radiated by the antenna was calculated in CST Microwave Studio and the transfer function of the antenna ($T_A(f)$) was es-

tablished as the ratio between the far field and the voltage applied to the entrance of the antenna. The far field component was calculated at coordinates (*ϕ=0°, θ=90°, r=1 m*), see Figure 4.12 for reference. The resulting transfer function is shown in Figure 4.18.

The radiated field in the frequency domain and in the time domain are presented in Figure 4.19 and Figure 4.20 respectively.

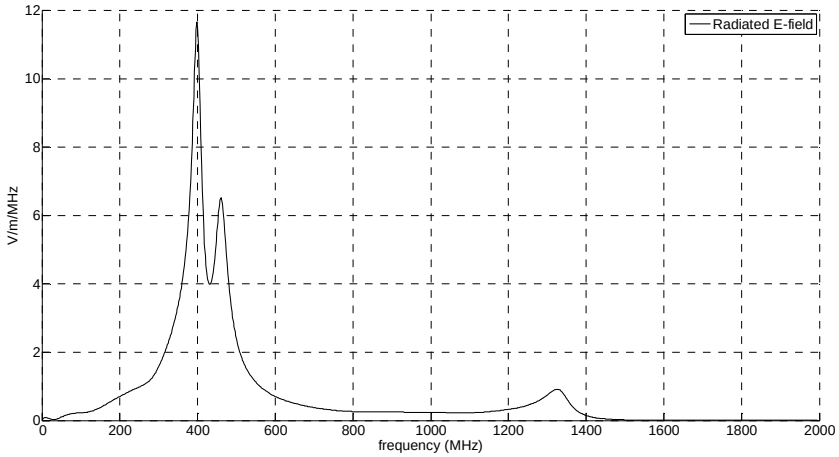

Figure 4.19 Radiated Electric field in the frequency domain at ϕ=0°, θ=90°, r=1 m. The spark gap is supposed to be lossless. Notice a vestigial resonance at the second harmonic of the fundamental frequency

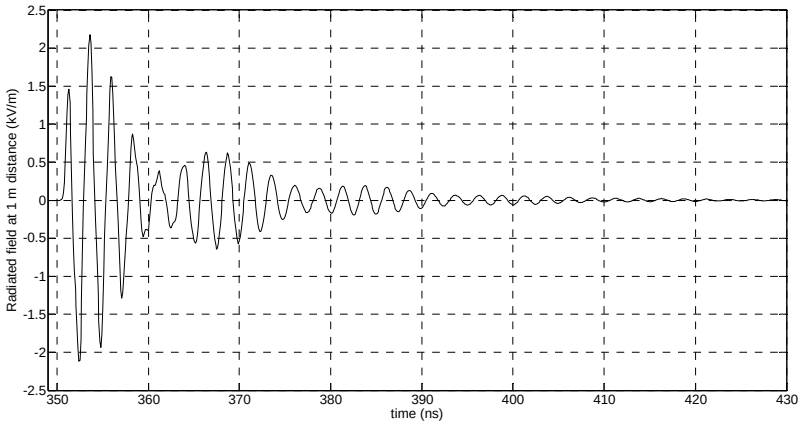

Figure 4.20 Radiated field in the time domain at coordinates ϕ=0°, θ=90°, r=1 m. The spark gap is supposed to be lossless.

The methodology presented in this chapter permits to study the effects of the impedance of the spark gap on the radiated signal. For the case of the present example, the spark gap resistance was varied between 0 and 0.5 Ohms and the resulting electric field was calculated in both frequency and time domains.

The results in the frequency domain are presented in Figure 4.21. As it can be seen, the peak amplitude of the radiated signal reduces greatly as R_g increases.

The results in the time domain are presented in Figure 4.22. The amplitude of the first peak is almost identical for all the considered values of R_g. However, due to the losses in the switch the amplitude of the subsequent signal reduces with the increasing of R_g. The number of cycles also reduces with the increasing of R_g.

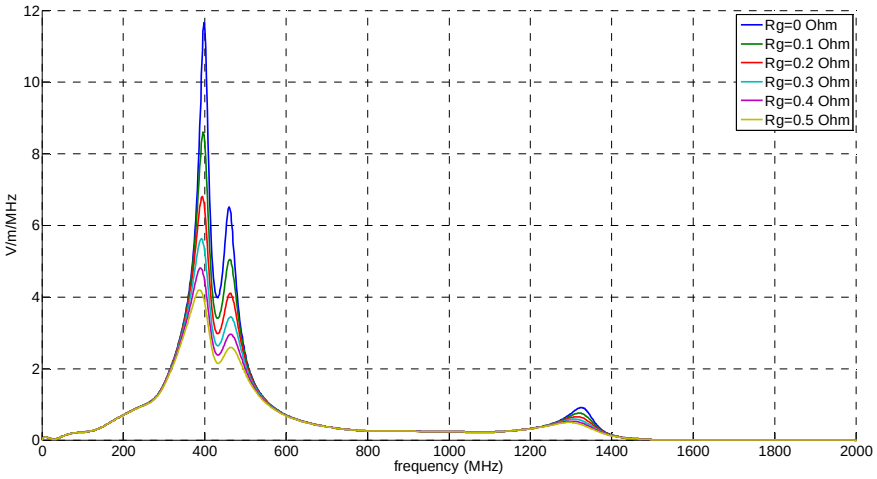

Figure 4.21 Radiated Electric field in frequency domain for different values of the spark gap resistance

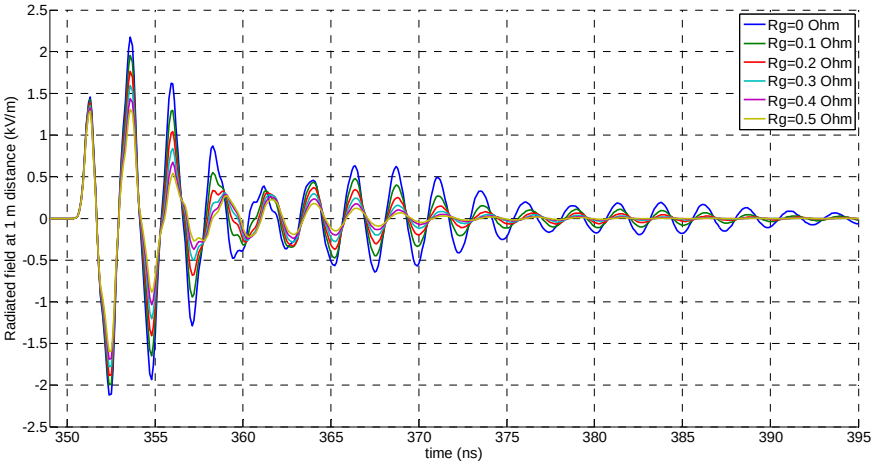

Figure 4.22 Radiated field at coordinates ϕ=0°, θ=90°, r=1 m, for different values of the spark gap resistance.

The model here presented only takes into account the static behavior of the spark gap. In order to include the dynamic variation of the impedance of the arc,

i.e. the closing time and the changes in the residual resistance, a time domain model might be preferable. In Appendix 1, we derive time domain equations for the calculation of an SWO connected to a spark gap at one end and to a frequency domain antenna at the other end.

4.9. CONCLUSIONS

We have presented in this chapter a methodology permitting the analysis and modeling of an SWO. The methodology permits the estimation of the response of the SWO, the resonance frequency, bandwidth and amplitude of the radiated signal connected to an antenna of arbitrary behavior in the frequency domain.

The proposed methodology was applied to the design of an SWO connected to a monopole antenna.

The voltage at the output of the SWO was calculated using as load the input impedance of a monopole antenna whose reactive part was zero at the intended resonance frequency of the SWO. For comparison, the same calculation was repeated using as load a pure resistor of the same value of the antenna at the intended resonance frequency. In the case of the resistive load, it was found that the system was resonant at the eigenfrequency of the SWO, namely the intended frequency.

The methodology here presented permitted to show that, in the case of the monopole antenna, the resonance frequency of the produced voltage was different from the intended resonance frequency, this in spite the fact that both the SWO and the monopole antenna were resonant at the same frequency.

The influence of the losses of the spark gap on the radiated signal was studied and discussed. It was shown that small changes in the resistance of the spark gap can reduce the amplitude of the radiated signal as well as the number of cycles.

REFERENCES

[1] D. M. Pozar, *Microwave Engineering*, 3 ed.: Wiley, 2004.

[2] F. Vega, *et al.*, "Design and optimization of mesoband radiators using chain parameters," in *Electromagnetics in Advanced Applications (ICEAA), 2011 International Conference on*, 2011, pp. 1310-1313.

[3] D. V. Giri, *et al.*, "Switched Oscillators and Their Integration Into Helical Antennas," *Plasma Science, IEEE Transactions on*, vol. 38, pp. 1411-1426, 2010.

[4] M. Armanious, *et al.*, "Interaction Between Geometric Parameters and Output Waveforms in High-Power Quarter-Wave Oscillators," *Plasma Science, IEEE Transactions on*, vol. 38, pp. 1124-1131, 2010.

[5] F. Tesche, M., *et al.*, *EMC Analysis Methods and Computational Models*: John Wiley & Sons Inc 1997.

[6] E. N. Protonotarios and O. Wing, "Analysis and Intrinsic Properties of the General Nonuniform Transmission Line," *Microwave Theory and Techniques, IEEE Transactions on*, vol. 15, pp. 142-150, 1967.

[7] Baum.C.E, "Switched Oscillators," *Circuit and Electromagnetic System Design Notes,* vol. 45, pp. -, September 2000.

[8] T. Liu and F. Tesche, "Analysis of antennas and scatterers with nonlinear loads," *Antennas and Propagation, IEEE Transactions on,* vol. 24, pp. 131-139, 1976.

[9] J. H. Ryu, "Eletromagnetic simulation of initially charged structures with a discharge source," *Progress In Electromagnetics Research M,* vol. 16, pp. 95-104, 2011.

[10] T. H. Martin, *et al.*, *J.C. Martin on Pulsed Power*: Springer, 1996.

[11] D. Giri, *et al.*, "Intermediate and far fields of a reflector antenna energized by a hydrogen spark-gap switched pulser," *IEEE Transactions on Plasma Science*, pp. 1631-1636, 1999.

CHAPTER 5

DESIGN, REALIZATION AND EXPERIMENTAL CHARACTERIZATION OF A COAXIAL SWITCHED OSCILLATOR

5.1. INTRODUCTION

We present in this chapter the design and realization of a coaxial Switched Oscillator (SWO).

The design is based on the developments presented in Chapters 2 through 4, including the proposed profile for the electrodes (IPS - Inverse Prolate Spheroidal).

The performance of the realized SWO has been experimentally characterized and the experimental data are used to test the theoretical models presented in the previous chapters.

The chapter is organized as follows. In Sections 5.2 and 5.3, we describe the mechanical design of the prototype. The experimental setup is described in Section 5.4. Section 5.5 presents the experimental characterization, which comprises the breakdown voltage of the SWO and the radiated electric fields for different types of connected antennas, which are compared with simulation results. In Section 5.6, we present a time-frequency analysis of the radiated signals using wavelets. Conclusions and discussion are presented in Section 5.7.

5.2. MECHANICAL DESIGN

The target frequency of the prototype is f_0= 433 MHz, which is the central frequency of one of the Industrial, Scientific and Medical (ISM) radio bands, used for several services, for instance Short-Range Device radio (SRD), Remote Keyless Entry Systems (RKE), among others.

The dimensions of the design are the same as the example presented in Chapter 4. We present here a short summary of the requirements of the design.

- Inter electrodic space: d_{gap}=0.5 mm
- Radiuses of the coaxial transmission line: outer radius, r_{o} =16.5 mm, inner radius, r_{i}=17.5 mm
- Coaxial line impedance: Z_{coax}=*3.5* Ω.

The electrodes of the SWO were fabricated using the IPS profile, proposed in Chapter 2. The gap distance on the axis is half of the distance between the inner and outer conductor of the coaxial. This means that the discharge is more likely to occur on the symmetry axis rather than between the conductors of the coaxial. A way of quantify this is using the safety factor *S*, defined in [1] as the ratio between the electric field on the gap and the maximum electric field on the coaxial:

$$S = \frac{E_{gap}}{E_{coax}} \tag{5.1}$$

Using the results of Chapter 2,

$$S = \frac{E_{gap}}{E_{Coax}} = \frac{\frac{V}{d}}{\frac{V}{r_i Log\left(\frac{r_0}{r_i}\right)}} = \frac{r_i}{d} Log\left(\frac{r_0}{r_i}\right) = 1.94 \tag{5.2}$$

A smaller value of *d* increases the factor *S*. However a value *d=0.5* mm, is the minimum distance that the EPFL mechanical workshop can fabricate with an acceptable tolerance.

The profile of the electrodes was obtained using the Inverse of Prolate Spheroidal system and is presented in Figure 5.1.

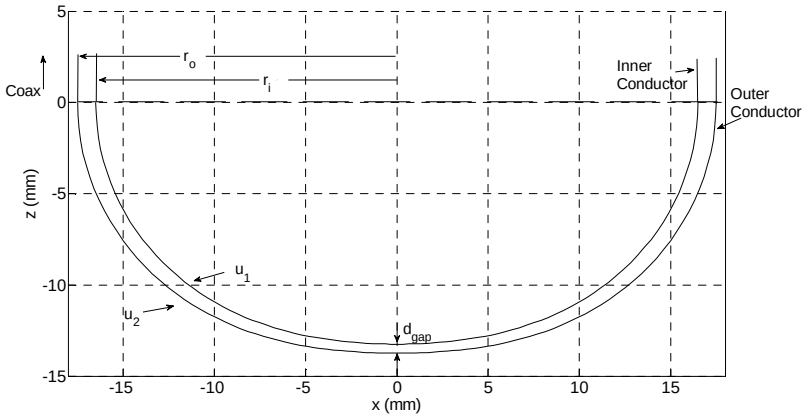

Figure 5.1 Profile of the electrodes

The calculated length of the coaxial line is:

$$L_{Coax} = 123.4(mm) \tag{5.3}$$

The IPS profiles were calculated in Matlab® and imported in Solidworks®. The resulting curves were loaded into a CNC machine and the electrodes were fabricated in stainless steel. A second version of the electrodes with Copper-Tungsten (80%-20%) alloy is planned for manufacturing.

The inner and outer conductors of the main coaxial section were custom machined in aluminum using a CNC lathe. The gas inlets were installed on the walls of the outer conductor.

In order to support the inner and outer conductors in a proper place, a dielectric ring made of Ultem ® (amorphous thermoplastic polyetherimide PEI) was inserted at the end of the main coaxial line. This section constitutes a secondary coaxial

section inserted between the SWO and the antenna. We will show in the next section how to evaluate the effects of this section in the output signal.

A 2-D view of the SWO detailing all its parts is presented in Figure 5.2. A similar 2-D view, indicating the sizes of the parts can be seen in Figure 5.3. A view of the SWO with the monopole and the ground plane is shown in Figure 5.4. Pictures of the finished prototype can be seen in Figure 5.5, Figure 5.6 and Figure 5.7

The mechanical design and specification of each one the parts of the SWO and the antenna were performed by the author of this work. The parts were manufactured at the ISIC mechanical workshop at EPFL.

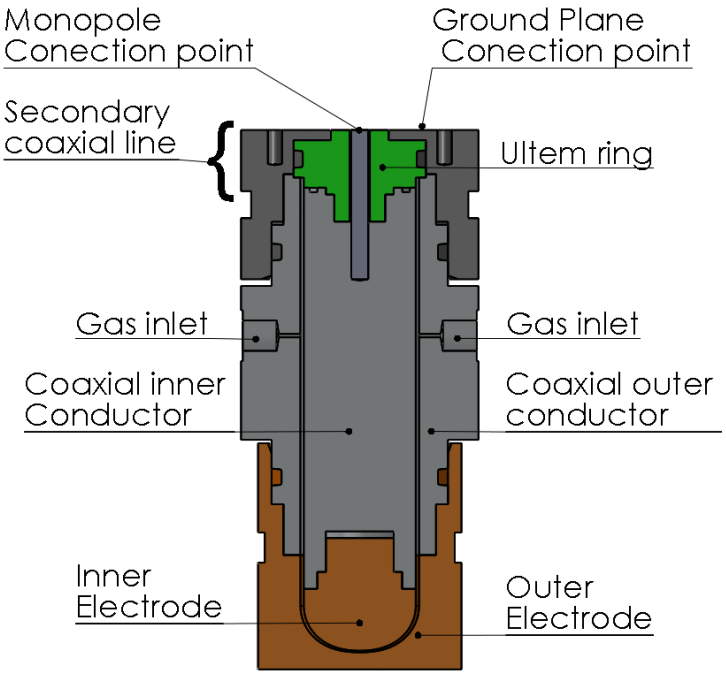

Figure 5.2 2-D cut view of the SWO. Notice the electrodes, the main coaxial line and the secondary coaxial sections.

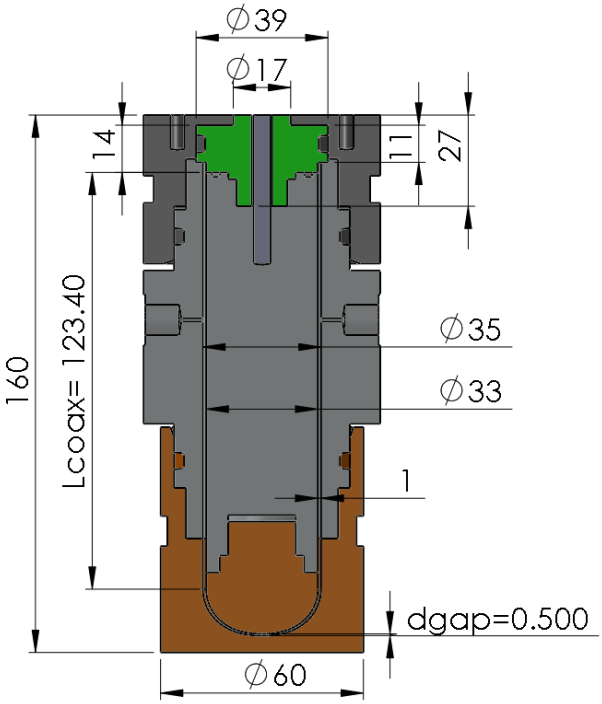

Figure 5.3 2-D cut view of the SWO. The units are in mm.

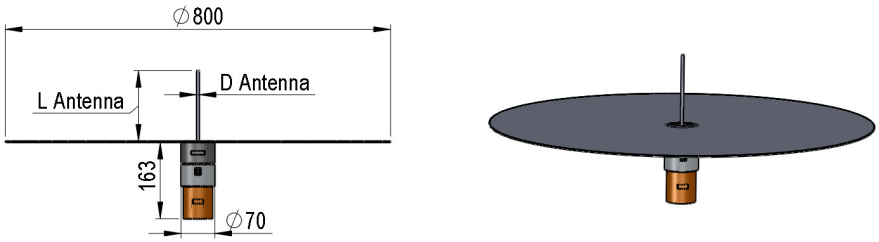

Figure 5.4 Side view of the SWO with the ground plane and the monopole antenna (left). Isometric view (right). Units are in mm.

Figure 5.5 The realized prototype with the external electrode removed. Notice the inner electrode and part of the inner conductor of the main coaxial line. Notice also the sealing O-ring and the supports for the gas inlets in the wall of the coaxial line.

Figure 5.6 The assembled SWO. Notice the outer electrode, the outer coaxial conductor with the two gas inlets and the outer conductor of the secondary coaxial line.

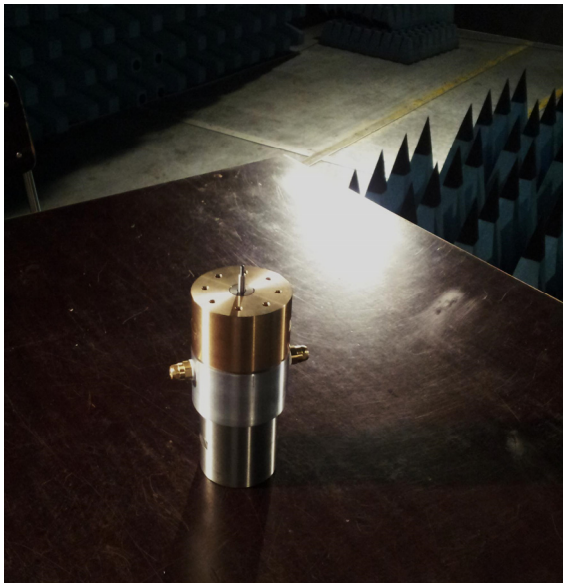

Figure 5.7 View of the SWO. Notice the point of connection of the monopole antenna. Additional insulation was added after manufacturing, in order to prevent flashover from the inner conductor to the ground plane

5.3. GAS TYPE

The experiments here reported were performed using SF6 as insulating gas. SF6 is used regularly in high voltage facilities and equipment and in pulse power applications. This gas presents one of the highest dielectric strengths among the gases available in the market.

The realized SWO was tested to a maximum pressure of 40 bars with no detectable leakage of gas.

The breakdown voltage in a gap pressurized in SF6 depends on the pressure, the gap distance and the electric field in the interelectrodic space. If the field is uniform, the breakdown voltage (V_{bd}) is [2]:

$$V_{bd} = 0.65 + 8.85 p d_{gap} \text{ (kV)} \tag{5.4}$$

where:
p is the SF6 pressure in bar
d_{gap} is the inter-electrode distance in mm

We saw in Chapter 2 that the field distribution is not uniform between the electrodes, having a maximum on the axis of symmetry, which is the most likely location for the discharge to occur. However, on the axis of symmetry the electric field is almost constant and its value coincides with the value of the electric field

on a uniform gap; therefore we consider valid the value of Equation (5.4) in our case.

It's worth noticing that SF6 is a greenhouse effect gas. It has been estimated that SF6 has a Global Warming Potential (GWP) 22600 times higher than that of CO2 [3]. It also has been mentioned that toxic byproducts are produced when high energy discharges occurs in SF6 [4].

5.4. EXPERIMENTAL SETUP

The experimental setup is described in Figure 5.8. The SWO is charged using a constant-current, high-voltage source Model HCE 35. This source, conceived originally as a capacitor charger, can deliver up to 10 mA of current and a maximum voltage of 35 kV. In order to prevent high frequency signals transmitted to the source, a blocking coil was placed between the SWO and the source. The source was controlled using an external trigger generator. A picture of the setup is presented in Figure 5.9.

The gas was connected to the SWO using a dielectric, rigid pipe; this means that there is not galvanic connection between the SWO, the gas bottle and the ground. The gas bottle was installed horizontally on the floor of the anechoic chamber, in to prevent unwanted reflections of the signals.

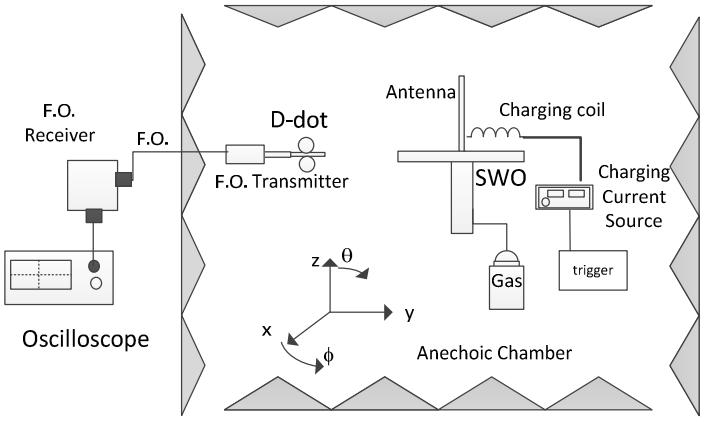

Figure 5.8 Experimental setup. The SWO was installed inside an anechoic chamber. A constant current source charges the SWO. The radiated field was measured with a D-dot sensor. The radiated signal was relayed to the oscilloscope outside the chamber using a fiber optic link.

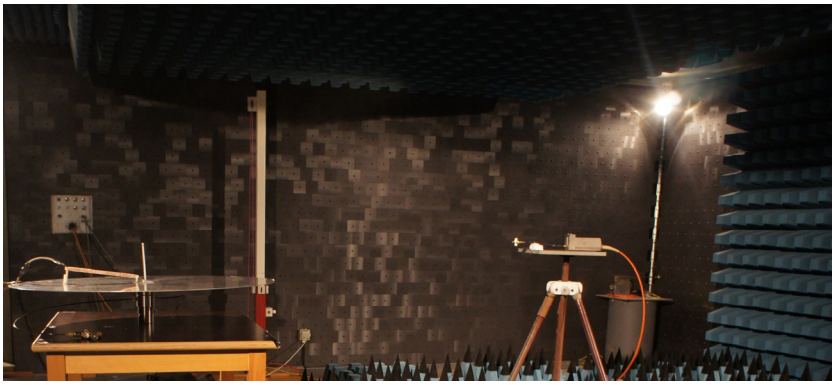

Figure 5.9 Experimental setup. Notice the SWO on the left and the D-dot connected to the fiber optic transducer on the right. On this picture the sensor is 1.2 m above the ground floor, which is 20 cm higher than the actual height of the sensor during the measurements.

The signal was measured using a Thales-Melopée D-dot E-1602 sensor. The signal measured by the D-dot sensor was integrated by an analog integrator and relayed outside the chamber using a fiber optic link. The receiver of the fiber optic link was connected to a 1.5 GHz, 10 GS/s Lecroy-9362 oscilloscope.

The SWO and the D-dot sensor were mounted on dielectric supports. The distance between the ground plane of the monopole antenna and the floor of the chamber was 1 m. The D-dot sensor was placed at a distance of 1.5 m from the monopole antenna and 1 m height above the ground floor of the chamber.

5.5. MEASUREMENTS

5.5.1. BREAKDOWN VOLTAGE

The breakdown voltage of the SWO versus the applied pressure of SF6 was measured using a P6015A Tektronix high voltage probe, for voltages up to 20 kV. For voltages higher than 20 kV, the meter of the current source was used. Figure 5.10 presents the measured values vs. theoretical values predicted by Equation (5.4). For each value of the pressure, three measurements were carried out and the breakdown voltage was measured. As it can be seen, additional to the typical variation of the breakdown voltage in a spark gap, the results suggest that the actual inter-electrodic gap distance is smaller than the expected value. A linear regression on the measured values indicates that the actual gap distance is d_{gap}=0.47 mm, instead of 0.5 mm.

Figure 5.11 shows the state of the electrodes after being in use. The marks produced on the metallic surface of the electrode by the discharges are visible on the picture. As it can be seen, most of the erosion is concentrated around the axis of the electrode. However, a few traces appear off axis, indicating that misfire occurs. However, this happened only in the region near axis and never in the regions near the coaxial section.

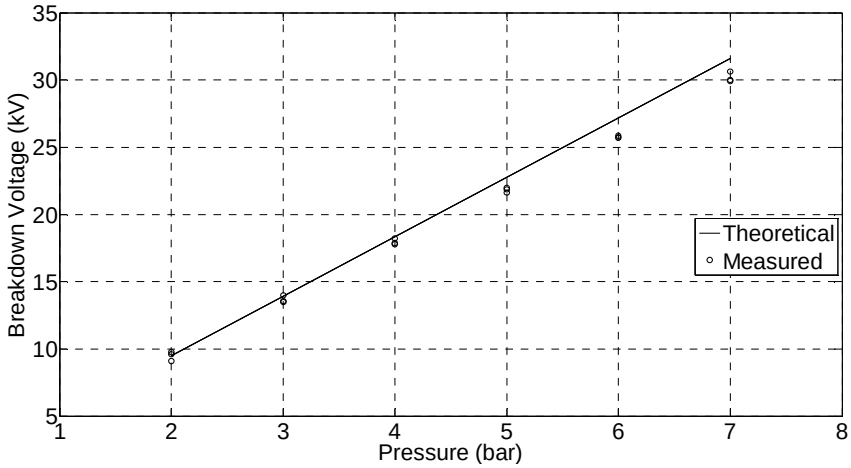

Figure 5.10 Theoretical breakdown voltage (continuous line), measured breakdown voltage (dots). Three values of the breakdown voltage per applied pressure were taken.

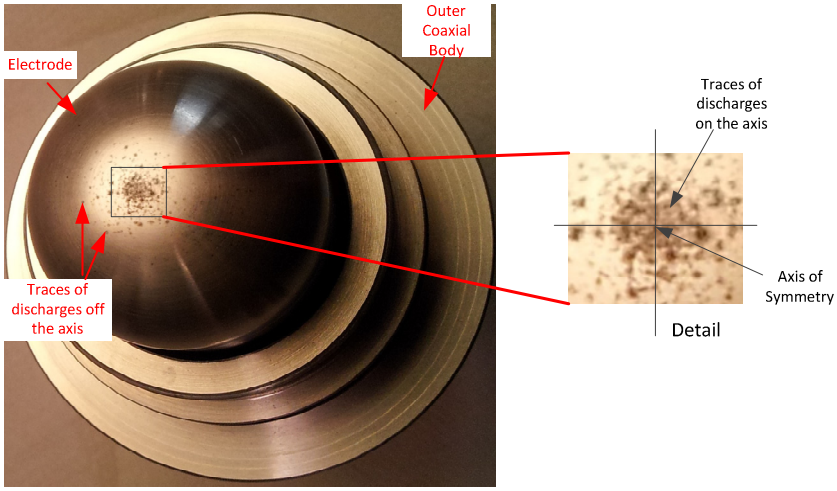

Figure 5.11 IPS electrode after being in use. Notice a high percentage the traces of the discharges near the center of the electrode. A small percentage of off-axis traces are visible.

5.5.2. Ultem Gasket Section

In chapter 4, the SWO was represented using the system depicted in Figure 5.12.

The equation relating the radiated electric field at specific coordinates of the space ($E(f,r,\theta,\phi)$) and the voltage applied at the discharge point $V_{SG}(f)$ was established as:

$$E(r,\theta,\phi,f) = T_A(r,\theta,\phi,f)V_{SG}(f)\frac{Z_A(f)}{A(f)Z_A(f)+B(f)} \tag{5.5}$$

where:

$Z_A(f)$ is the impedance of the antenna

$V_{sg}(f)$ is the excitation voltage at the spark gap

$A(f)$ and $B(f)$ are the total A and B parameters of the SWO

$V_A(f)$ is the voltage at the input of the antenna

$T_A(f)$ is the electric field to applied voltage transfer function of the antenna, calculated as:

$$T_A(f) = \frac{E(f,r,\theta,\phi)}{V_A(f)} \tag{5.6}$$

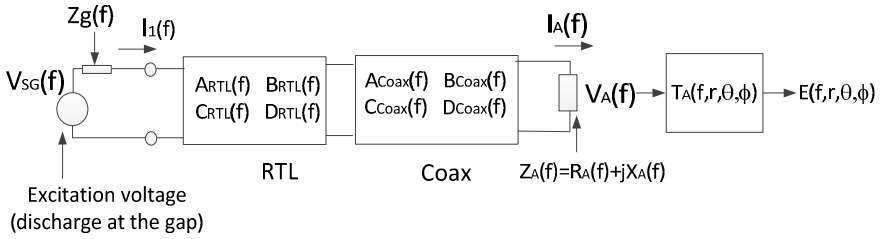

Figure 5.12 Representation of the SWO using a cascaded two-port networks characterized by their ABCD matrices (see Chapter 4).

The actual geometry of the realized SWO, however, has an additional transmission line between the main coaxial line and the antenna, corresponding to the region where the Ultem ring is inserted (see Figure 5.3). Figure 5.13 presents a modified version of the system presented in Figure 5.12.

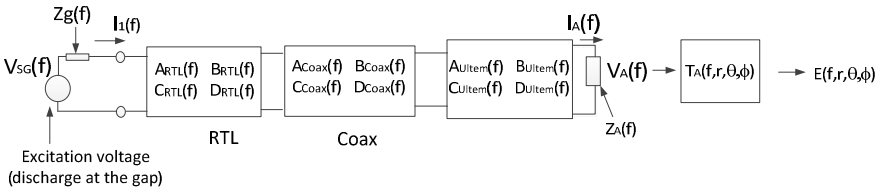

Figure 5.13 Modified version of the model presented in Chapter 4. Now the SWO sees a load impedance composed by the Ultem line terminated on the radiating antenna.

The ABCD parameters of the Ultem line were calculated via numerical simulation and included in the model in order to obtain a new set of ABCD parameters

for the SWO. The new $A(f)$ and $B(f)$ parameters can be included in Equation (5.5) and the resulting E field can be calculated.

5.5.3. Monopole Antennas

The SWO was connected to two different monopole antennas. The dimensions of the monopoles are presented in Table I. Note that the resonance frequency of the first antenna coincides that of the SWO. The input impedance and the antennas are presented respectively in Figure 5.14(a) and Figure 5.15(a). The transfer function of each monopoles at coordinates (r=1.5 m, θ= 90°, ϕ= 0°) are presented respectively in Figure 5.14(b) and Figure 5.15(b). All these results were obtained by numerical simulations (for the configuration shown in Figure 5.8).

Table 1 Dimensions of the monopoles.

Antenna	Diameter	Length	Ground Plane Diameter	1st Resonance frequency (Computed in CST)
I	8 mm	159 mm	800 mm	433 MHz
II	8 mm	260 mm	800 mm	262 MHz

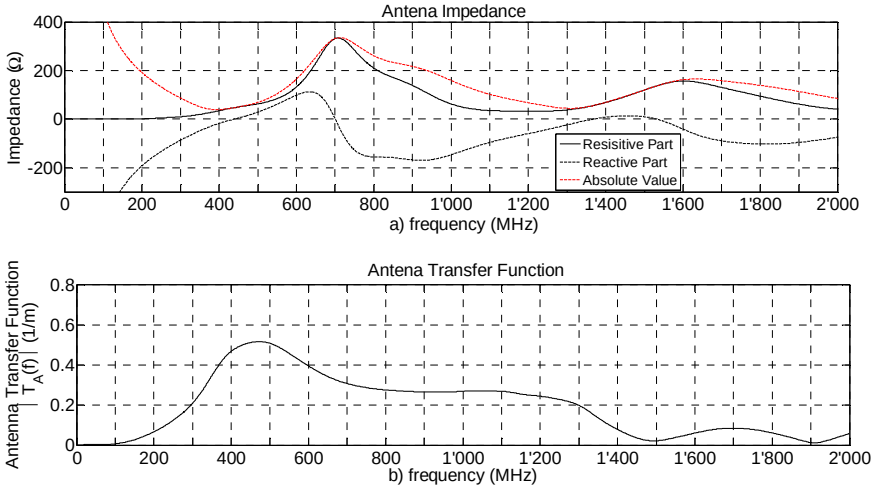

Figure 5.14 (a) Impedance of Antenna I. Notice the first resonance frequency at f=433 MHz. (b) Magnitude of the Transfer function of Antenna I at coordinates r=1.5 m, θ= 90°, ϕ= 0°. Notice the peak at 433 MHz. The dimensions of the antenna are L_A=159 mm, d_A= 8 mm. Both results were obtained by simulation.

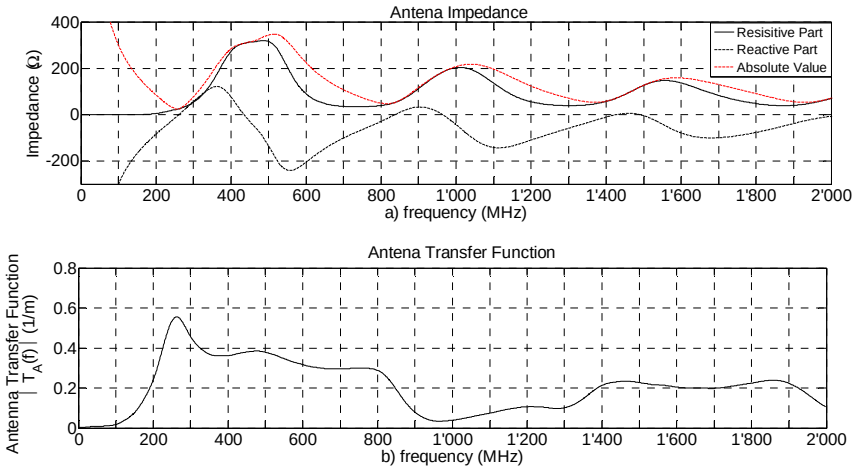

Figure 5.15 (a) Simulated impedance of Antenna II. Notice the first resonance frequency at f=262 MHz. (b) Magnitude of the Transfer function of Antenna II at coordinates r=1.5 m, θ= 90°, ϕ= 0°. Notice the peak at 262 MHz. The dimensions of the antenna are L_A=260 mm, d_A= 8 mm. Both results were obtained by simulation.

5.5.3.1. Field radiated by Antenna I

The electric field measured with the D-dot sensor (after integration) is presented in Figure 5.16 (a). The signal exhibits a modulated Gaussian waveform, followed by a series of residual ripples. The measured peak amplitude is E_{peak}=10 kV/m. The corresponding signal obtained by the proposed theoretical approach is shown in the same figure (lower panel). Notice that most of the energy of the signal is contained in the time interval between t = 5 ns to t = 16 ns, in which there is a very good agreement between the measured and the computed signals.

The Power Spectrum Densities (PSD) of the measured and computed signals are plotted in Figure 5.17. The PSDs were evaluated using the Yule-Walker's method [5]. As it can be seen from the graphs, the resonance frequency is 370 MHz. The maximum amplitude of the PSD of the theoretical signal is 10% higher than that of the measured signal. Nevertheless, the proposed theoretical model is able to reproduce reasonably well the measured results.

It is interesting to observe that the resonance frequency of the radiated field is different from the intended resonance frequency (433 MHz), despite the fact that both the SWO and the monopole antenna were resonant at this same frequency.

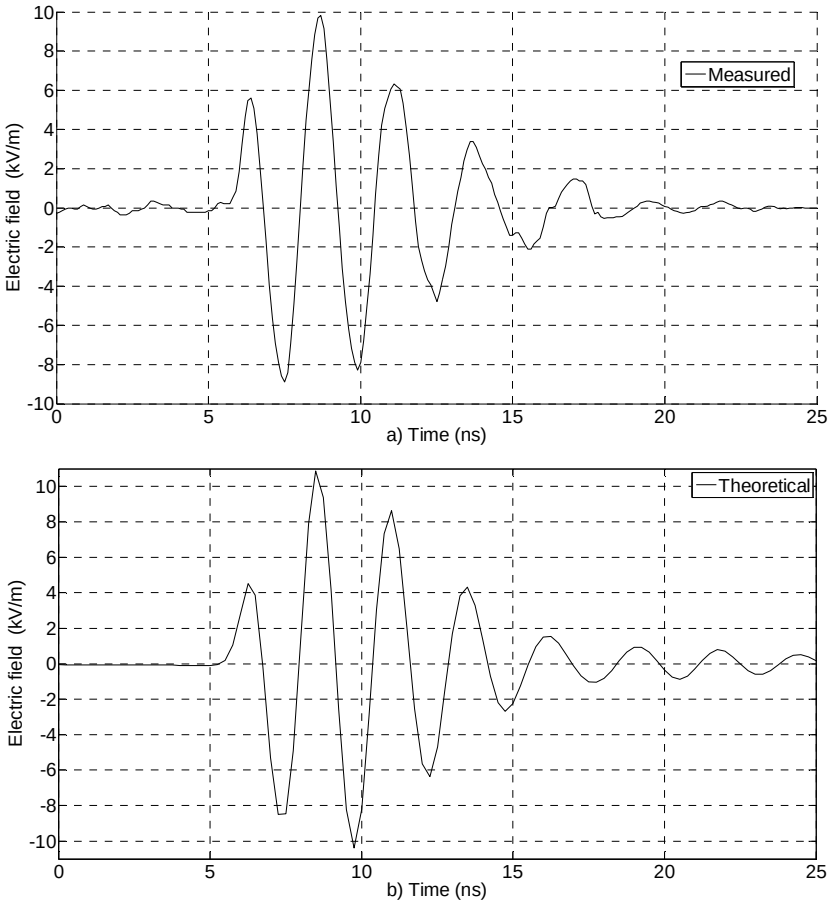

Figure 5.16Measured (a) and computed (b) electric field radiated by the SWO connected to Antenna I, at 1.5 m distance. The applied pressure is 7 bar of SF6. The peak amplitude is 10 kV/m. Notice the presence of some reflections on the measurement after 15 ns. The time *t*=0 corresponds to the closing of the switch in the SWO.

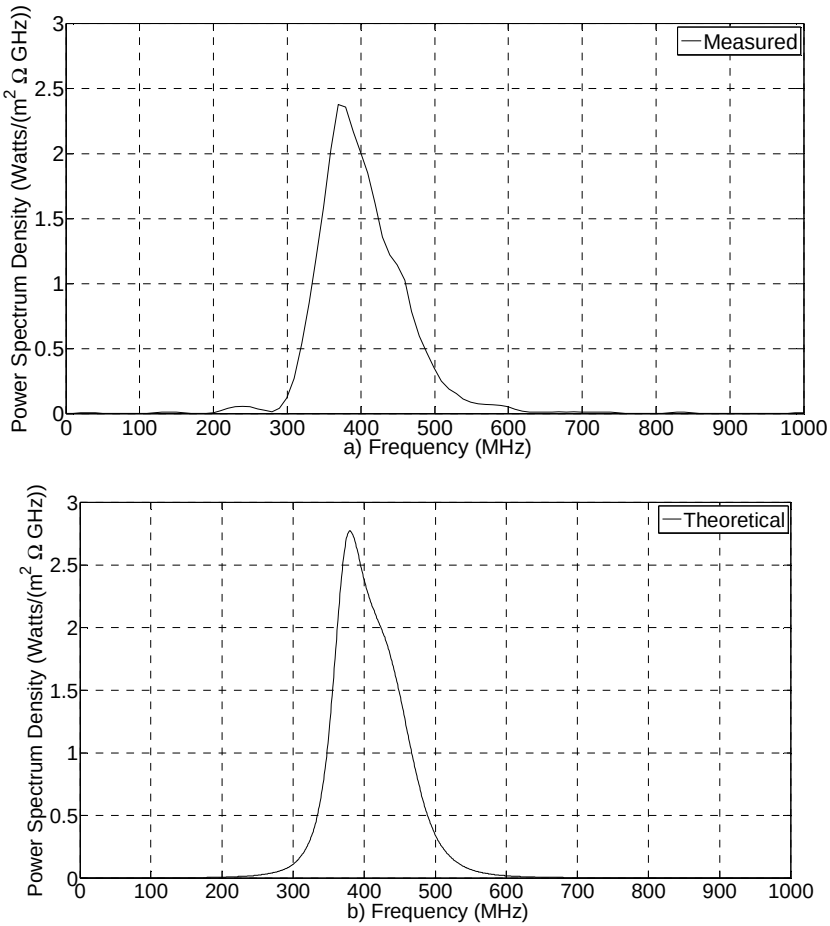

Figure 5.17 Power Spectrum Density (PSD) of the measured electric field (a) and that of the computed electric field (b). Field radiated by the SWO connected to Antenna I, at 1.5 m distance. The applied pressure is 7 bar of SF6. The resonance frequency is 370 MHz.

5.5.3.2. Field radiated by Antenna II

The dimensions of this antenna are: d_a= 5 (mm), L_a=260 (mm). The diameter of the ground plane is d_g=800 (mm).

The measured electric field at 1.5 m distance and an applied pressure of 7 bars of SF6 is shown in Figure 5.18. As it can be seen, the peak amplitude is almost -6 kV/m. It can also be noticed that the late-time response of the measured field (beyond about 23 ns) suffers a faster attenuation than the theoretical one.

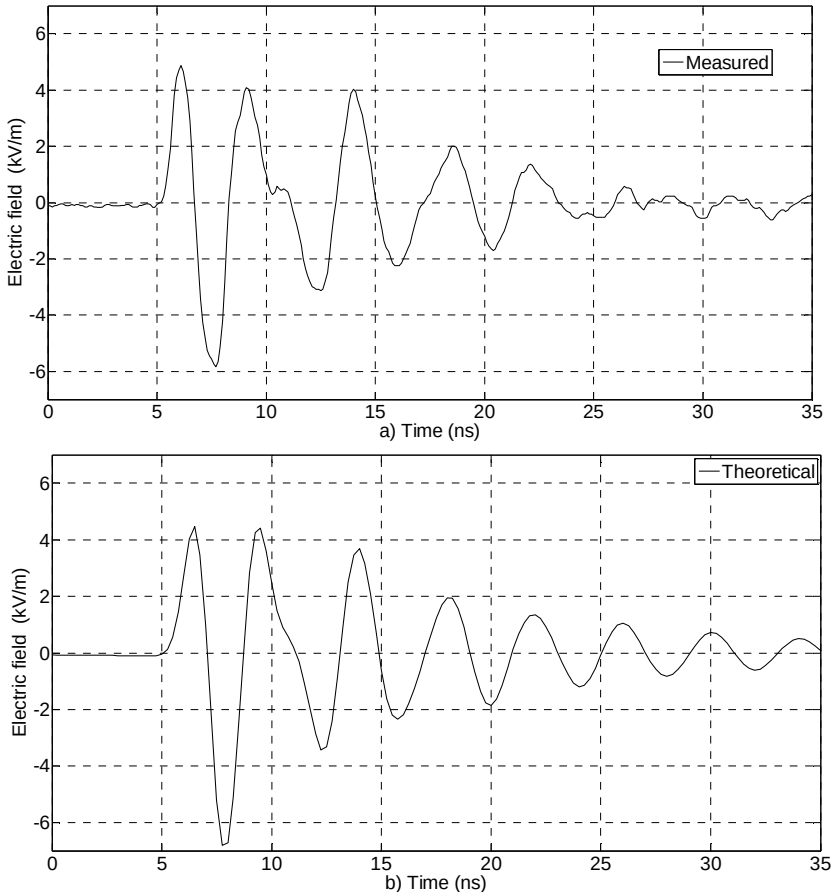

Figure 5.18 Radiated electric field at 1.5 m distance by the SWO connected to Antenna II. The applied pressure is 7 bar of SF6. The peak amplitude is -6 kV/m. Notice that beyond 23 ns, the measured signal attenuates faster than the theoretical wave. The time t=0 corresponds to the closing of the switch in the SWO.

An estimation of the PSD of the signal, evaluated using the Yule-Walker method is presented in Figure 5.19. Two resonance frequencies can be distinguished, the first one at 240 MHz and the second one at 400 MHz. The two frequencies are clearly discernible in both, measured and theoretical signals. Note that the first resonance frequency is close to the resonance frequency of the antenna, while the second resonance frequency is close to the resonance frequency of the SWO.

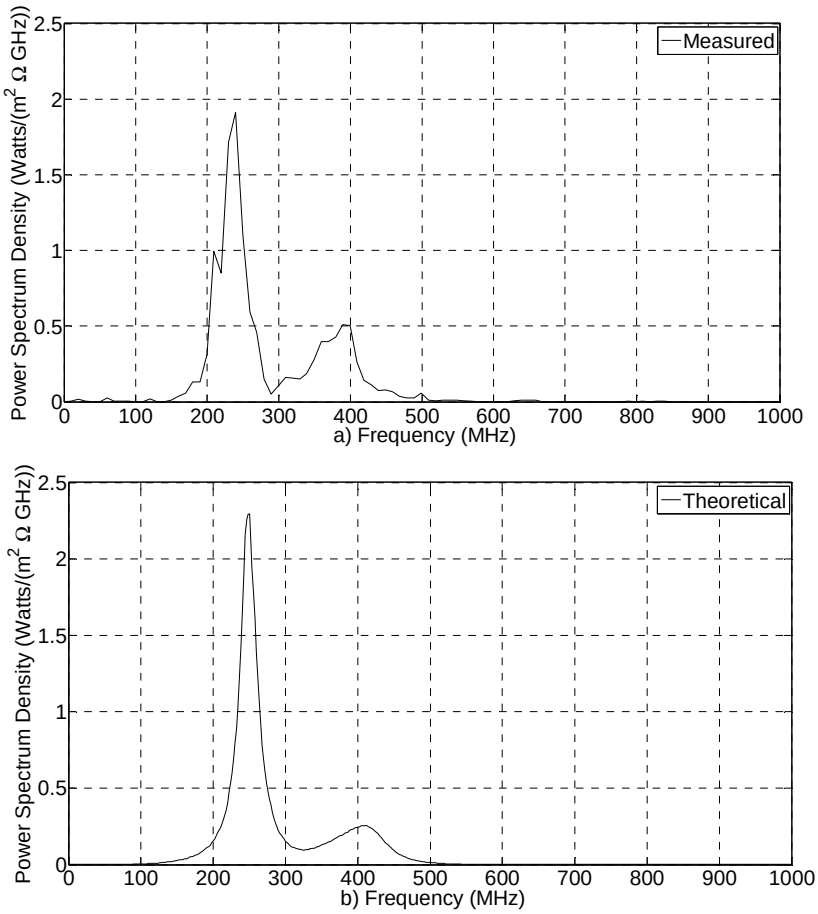

Figure 5.19 Power Spectrum Density estimation of the electric field radiated at 1.5 m distance by the SWO connected to Antenna II. Notice a first resonance of the signal at 240 MHz and a second resonance near 400 MHz

5.6. TIME-FREQUENCY ANALYSIS OF THE RADIATED SIGNAL

In this section, the time evolution of the frequency content of the radiated wave will be analyzed. Instead of classical algorithms such as the Short Fourier Transform (SFT), a more efficient [6] approach based on Wavelets will be applied.

The coefficients of the Continuous Wavelet Transform (CWT) of the radiated field $E(t)$ can be calculated as [7]:

$$CWT(a,b;E(t),\Psi(t)) = \int_{-\infty}^{\infty} \frac{1}{\sqrt{a}} E(t) conj\left(\Psi\left(\frac{t-b}{a}\right)\right) dt \tag{5.7}$$

where:

a >0 is the scale parameter,

b is the translational value,

Ψ(t) is the mother wavelet, in this case a fourth-order Gaussian wavelet.

conj( ) is the conjugate operator

The frequency at which the magnitude of the spectrum of the wavelet maximizes is called f_c. The pseudo-frequencies of the wavelet (f_a) are then defined as:

$$f_a = \frac{f_c}{a f_s} \tag{5.8}$$

where f_s is the sampling frequency of the signal *E(t)*

Using these definitions, we can re-write Equation (5.7) and express CWT in terms of its pseudo-frequencies:

$$CWTF\left(f_a,b;E(t),\Psi(t)\right) = \sqrt{\frac{f_a}{f_0}} \int_{-\infty}^{\infty} E(t) conj\left(\Psi\left(\frac{f_a}{f_0}(t-b)\right)\right) dt \tag{5.9}$$

Using Equation (5.9), a 2-D time-frequency diagram of the *CWTF* can be drawn. The horizontal axis is the time (t), the vertical axis is the pseudo-frequency axis (f_a). A color-coded scale represents the normalized amplitude of the coefficients of the CWTF.

Figure 5.20 shows the CWTF applied to the electric field radiated by Antenna I. Figure 5.21 presents the same analysis applied to the simulated signal. As it can be seen, the CWTF graphs show that most of the energy content of the signal is in the region originally intended, 433 MHz. The result of the CWTF applied to the signal calculated with the theoretical model coincides to a great extent to the result of the CWTF applied to the measured signal.

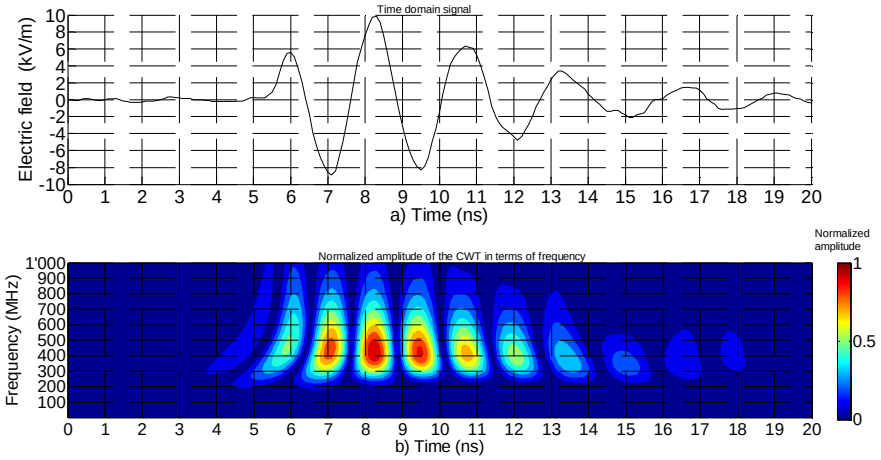

Figure 5.20 (a) Time domain signal radiated by Antenna I. (b) Normalized Continuous Wavelet Transform in terms of Frequency. The CWTF shows that most of the energy of the signal is concentrated around the second positive peak and has frequency components between 400-500 MHz. The ripples afterwards contain energy in the 350-400 MHz region.

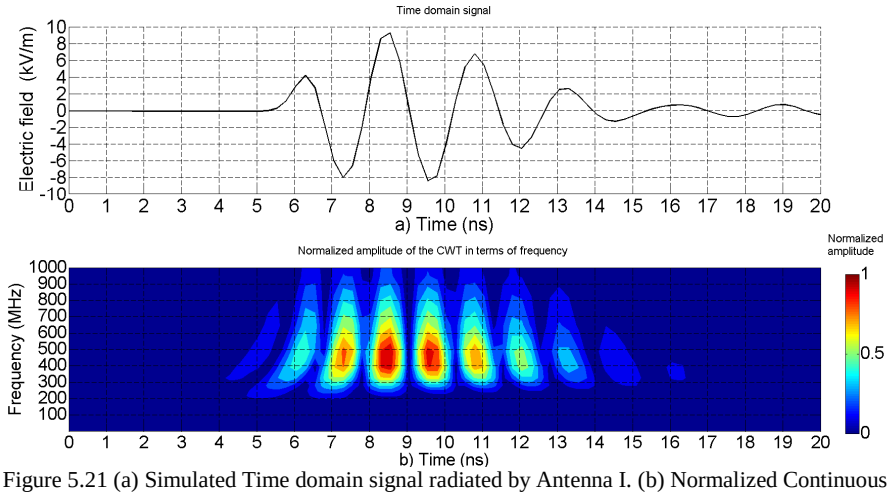

Figure 5.21 (a) Simulated Time domain signal radiated by Antenna I. (b) Normalized Continuous Wavelet Transform in terms of Frequency. The computed CWTF agrees quite well with the experimental results shown in Figure 5.20

Figure 5.22 shows the CWTF applied to the electric field radiated by Antenna II. Figure 5.23 presents the same analysis applied to the simulated signal. As it can be seen, the CWTF graph shows that most of the energy content of the signal is concentrated between 250-400 MHz. The result of the CWTF applied to the signal calculated with the theoretical model agrees to a great extent to the result of the CWTF applied to the measured signal.

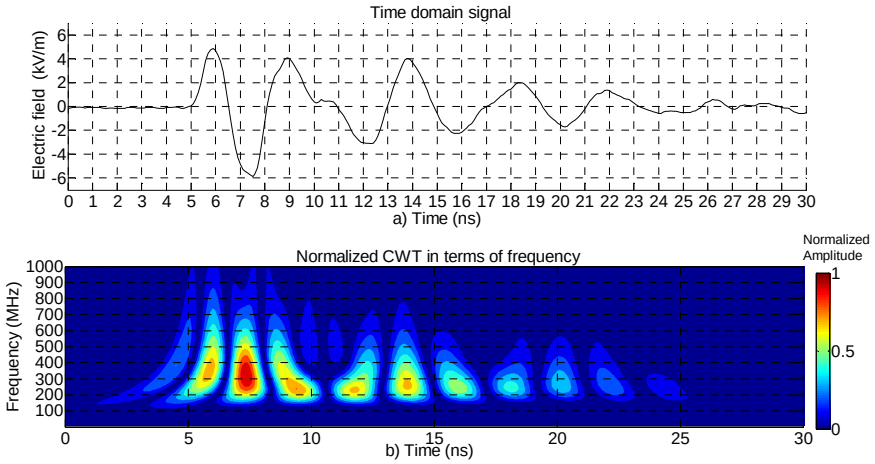

Figure 5.22 (a) Time domain signal radiated by Antenna II. (b) Normalized Continuous Wavelet Transform in terms of Frequency. The CWTF shows that most of the energy of the signal is concentrated around the first negative peak and has frequency components between 250 – 400 MHz. The ripples afterwards contain energy in the 250 MHz region, in agreement with Figure 5.19 (a)

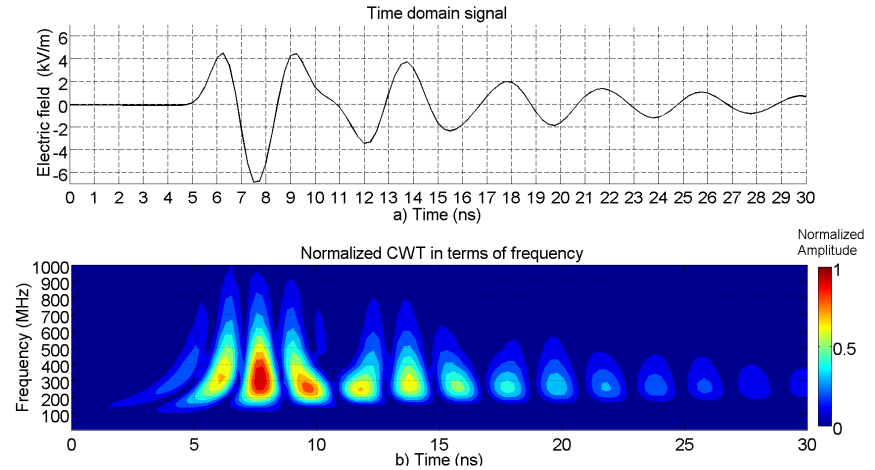

Figure 5.23 (a) Simulated Time domain signal radiated by Antenna II. (b) Normalized Continuous Wavelet Transform in terms of Frequency. The computed CWTF agrees well with the experimental results shown in Figure 5.21.

The presented analysis using wavelet transform permitted to characterize the time evolution of the frequency content of the radiated wave.

The measured and theoretical signals present some differences in their late time. However, it was shown that the frequency content of the most energetic parts of the measured and theoretical signals are in good agreement.

5.7. CONCLUSIONS

We reported in this chapter on the construction and test of a prototype coaxial quarter-wave switched oscillator.

The SWO integrates electrodes fabricated using the Inverse of Prolate Spheroidal profile presented in Chapters 2 and 3. The erosion produced on the surface of the electrodes by the discharges showed that a high percentage of the discharges occur near the axis of symmetry. This validates the design of the electrode, in spite the fact that a minor percentage of the traces appears off axis.

The breakdown voltage of the SWO was measured and compared with the theoretical values. It was concluded that the actual interelectrodic distance is 4.7 mm instead of the intended 5 mm.

The prototype was used for testing the validity of the model for the analysis of SWOs connected to frequency dependent antennas, proposed in Chapter 4. In particular, monopole antennas were connected to the SWO and the radiated field was measured and compared with theoretical calculations.

It was shown that the theoretical model was able to reproduce with an acceptable accuracy the behavior of the SWO connected to a frequency dependent load.

A continuous wavelet transform analysis was carried out on the measured and simulated signals, showing that the frequency content of the most energetic parts of the measured and simulated signals are in agreement.

The methodology permitted to show that, in the case of a monopole antenna, the resonance frequency of the radiated field is different from the intended resonance frequency, despite the fact that both the SWO and the monopole antenna were resonant at the same intended frequency.

Even though only monopole antennas were considered in this study, it is worth noting that the realized prototype can be used in conjunction with other types of antennas, such as directive antennas. Preliminary work for connecting a Half Impulse Radiating Antenna to the SWO has already been carried out by the author.

Finally, the base design of the prototype can easily be modified, in order to reach higher breakdown voltages. The resulting prototype can be used for producing high power, resonant, illuminating fields in IEMI testing.

REFERENCES

[1] M. Armanious, *et al.*, "Interaction Between Geometric Parameters and Output Waveforms in High-Power Quarter-Wave Oscillators," *Plasma Science, IEEE Transactions on*, vol. 38, pp. 1124-1131, 2010.

[2] E. Kupfel and W. S. Zaengl, *High Voltage Engineering* vol. 2, 2000.

[3] J. Olivier. and J. Bakker, *Good Practice Guidance and Uncertainty Management in National Greenhouse Gas Inventories*: IPCC, 2001.

[4] B. Daout and F. Vega, "SF6 for High Voltage Pulse Generators an Ecological Analysis," presented at the European Electromagnetics, EUROEM, Toulouse, France, 2012.

[5] S. M. Kay, *Modern Spectral Estimation*. Englewood Cliffs, NJ, 1988.
[6] L. Debnath, *Wavelet Transformation and their Applications*: Birkhäuser Boston, 2002.
[7] D. L. Fugal, *Conceptual Wavelets in Digital Signal Processing*. San Diego, California: Space and Signals Technical Publishing, 2009.

CHAPTER 6
CONCLUSIONS

The research work presented in this thesis was devoted to the design and analysis of coaxial quarter-wave Switched Oscillators (SWO). This chapter highlights the main original contributions and conclusions of this work.

6.1 ELECTROSTATIC DESIGN OF SWOs

The main requirements for the electrostatic design of a Switched Oscillator (SWO) were presented. A new profile for the electrodes of the SWO was proposed. The profile is based on a curvilinear coordinate system called Inverse Prolate Spheroidal (IPS) coordinate system. Design equations were derived for producing the electrodes, starting from the basic geometric requirements of spark gap distance and radii of the coaxial transmission line. It was shown that the proposed IPS profile results in an optimal distribution of the electric field, with a peak amplitude occurring on the axis of symmetry of the SWO, and a smooth, monotonic decrease as one moves away from the discharge point towards the coaxial transmission line. The Laplace equation was solved on this curvilinear space and analytical expressions for the electrostatic field and potential were obtained.

Electrostatic numerical simulations were performed for an illustrative example. The resulting distributions of the electric field and potential were presented and discussed. It was shown that the derived analytical expressions are in excellent agreement with finite-element numerical simulations, especially for SWOs having a low impedance coaxial line.

6.2 ELECTRODYNAMIC DESIGN OF SWOs

Analytical expressions for the electric and magnetic fields within the radial transmission line formed by the IPS electrodes were derived. A one-dimensional approximation for the potential and the fields was proposed. This approximation was shown to be accurate for typical SWOs for which the characteristic impedance of the coaxial line is very low (lower than 5 Ohms or so).

It was analytically demonstrated that the radial transmission line (RTL) of an SWO can be treated as a non-uniform transmission line. For the first time, an analytical expression for the characteristic impedance of the RTL of SWOs was derived.

An original approach based on the chain matrix parameters was developed for the analysis and modeling of an SWO connected to a frequency dependent antenna. The developed methodology permits the estimation of the electric field radiated by an SWO connected to an antenna of arbitrary behavior in the frequency domain.

The presented approach permitted to explain why in the case of a monopole antenna, the resonance frequency of the produced wave is different from the intended resonance frequency, in spite the fact that both the SWO and the monopole antenna were resonant at the same frequency.

The influence of the losses of the spark gap on the radiated signal was studied and discussed. It was shown that small changes in the resistance of the spark gap can reduce the amplitude of the radiated signal as well as the number of cycles.

The general principles for developing a time domain model for the SWO were also presented and developed.

6.3 APPLICATION OF THE PROPOSED DESIGN METHODOLOGY

The developed models were used to design a prototype of a 433 MHz coaxial, quarter-wave SWO. The SWO integrates electrodes fabricated using the proposed IPS (Inverse of Prolate Spheroidal) profile. The erosion produced on the surface of the electrodes by the discharges showed that the majority of the discharges occur near the axis of symmetry, validating the electrostatic considerations developed in this work.

The prototype was used for testing the validity of the electrodynamic model for the analysis of SWOs connected to frequency dependent antennas. Different monopole antennas were connected to the SWO and the radiated fields were measured and compared with theoretical calculations.

It was shown that the theoretical model was able to reproduce, with an acceptable accuracy, the behavior of the SWO connected to a frequency dependent antenna.

It is worth noting that the designed SWO can be connected in a straightforward way to more directive antennas. Preliminary work for connecting a Half Impulse Radiating Antenna (HIRA) to the SWO has already been performed by the author.

The base design of the prototype can easily be modified, in order to reach higher breakdown voltages.

The prototype realized in the framework of this research study and the resulting modified prototype will be used for producing illuminating fields for IEMI testing and assessments. Furthermore, they are also applied to research activities related to humanitarian demining and clearance operations in Colombia, carried out within the framework of an international collaboration involving the EMC laboratory of EPFL and the EMC group of the National University of Colombia and co-funded by the EPFL Centre Cooperation & Development (CODEV) ant the Swiss Agency for Development and Cooperation (SDC).

APPENDIX 1
A TIME DOMAIN MODEL OF THE SWO

The dynamic behavior of the spark gap discharge and its effects on the SWO cannot be fully characterized by the linear model presented in Chapter 4. We present in this Appendix the basis of a time domain model for the analysis of SWOs.

In [1] Santamaría et. al. presented a model for the calculation of the SWO using a time domain simulation in Alternative Transients Program (ATP). However the code works only for constant impedance antennas. The model we present on this section includes frequency dependent antennas.

The starting point of the proposed approach is the two-port network model discussed in Chapter 4 and presented in Figure 1.

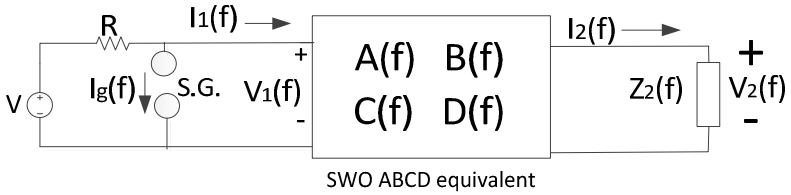

Figure 1 Two-port representation of the SWO

In this figure, V is the charging voltage, R is the high impedance charging resistor, SG is the spark gap, and $Z_L(f)$ is the input impedance of the antenna.

Notice that in this model we placed the charging voltage (V) on the left side of the two port network. This topology, even though not corresponding to the real situation in the SWO, can be considered as equivalent from a modeling point of view.

We can calculate the input impedance of the two-port network seen by the SG, namely the impedance seen at the input of the ABCD two-port network.

By definition:

$$\begin{bmatrix} V_1(f) \\ I_1(f) \end{bmatrix} = \begin{bmatrix} A(f) & B(f) \\ C(f) & D(f) \end{bmatrix} \begin{bmatrix} V_2(f) \\ I_2(f) \end{bmatrix} \tag{1}$$

From which the input impedance can be calculated as:

$$Z_1(f) = \frac{V_1}{I_1} = \frac{A + \frac{B}{Z_2}}{C + \frac{D}{Z_2}} \tag{2}$$

The equivalent circuit of Figure 1 can therefore be reduced to the one shown in Figure 2.

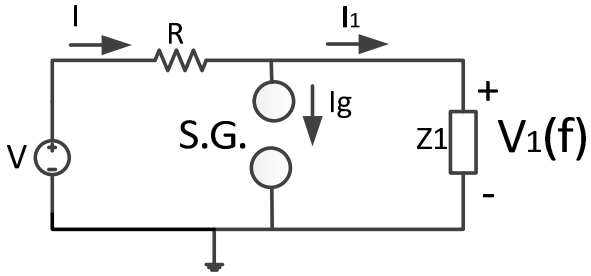

Figure 2 Equivalent circuit seen by the spark gap

Notice that *V* and *R* are assumed to be constant in time and independent of frequency.

This circuit can be transformed into a time domain equivalent circuit where the spark gap is represented by a time-varying resistor (see Figure 3**)**.

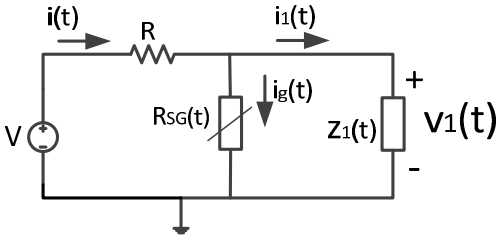

Figure 4 Time domain equivalent of the circuit at the spark gap

In this figure, $z_1(t)$ is the inverse Fourier transform of the impedance $Z_1(f)$ and $R_{SG}(t)$ is the time varying impedance of the spark gap.

Several equivalent models for the behavior of the spark gap exists [2]. As an example we will the Toepler model [3], according to which the impedance of the spark gap is:

$$R_{SG}(t) = \begin{cases} k\dfrac{i_g(t)}{\int_0^t i_g(t)dt} & if \quad V_{SG} \geq V_{th} \\ R_{gOff} & if \quad V_{SG} < V_{th} \end{cases} \tag{3}$$

where V_{th} is a threshold voltage, k is a constant and R_{gOff} is the open circuit resistance of the spark gap, typically in the order of several Giga-Ohms.

With these elements, the following equations can be established for the circuit of Figure 2:

$$V = Ri(t) + i_1(t) * z_1(t) \tag{4}$$

This can be transformed into:

$$V = Ri_g(t) + Ri_1(t) + i_1(t) * z_1(t) \tag{5}$$

where * denotes the convolution operator
The second equation is simply:

$$v_1(t) = i_1(t) * z_1(t) = v_g(t) \tag{6}$$

If $v_1(t) < V_{th}$, Equation (6) can be written as:

.. (7)

If $v_1(t) > V_{th}$, Equation (6) can be written as:

$$i_1(t) * z_1(t) = k_0 \frac{i_g(t)}{\int_0^t i_g(t)dt} \tag{8}$$

Equations (5) and (7)-(8) can be solved for $i_1(t)$, from which $v_1(t)$ can be obtained and the output of the two-port network can be obtained either convolving $v_1(t)$ with the time-domain transfer function of the SWO or by Fourier transforming $v_1(t)$ into frequency domain and multiplying it by the frequency domain transfer function of the SWO.

The equations can be discretized and solved as follows:
The discrete convolution operator is defined as:

$$x(t_i) * y(t_i) \approx \Delta t \sum_{k=0}^{i} x(t_k) y(t_{i-k}) \tag{9}$$

The integral appearing in Equation (8) can be discretized as:

$$\int_0^t i_g(t)dt \approx \Delta t \sum_{k=0}^{i} i_g(t_k) \tag{10}$$

The system is calculated at discrete times $t_i = 0, \Delta t, 2\Delta t, \ldots, i\Delta t$.

During times t_i , $i=2n$, where n is a positive integer, $i_g(t_i)$ is considered to be constant and $i_1(t_i)$ is calculated,

During times $t_{i,}$ $i=2n+1$, where n is a positive integer, $i_1(t_i)$ is considered to be constant and $i_g(t_i)$ is calculated, as follows:

At times $t_{i=2n}$, where n is a positive integer, we can calculate $i_1(t_i)$ assuming that $i_g(t_i) = i_g(t_{i-1})$:

$$V = Ri_g(t_i) + Ri_1(t_i) + \Delta t\sum_{k=0}^{i} i_1(t_k)\, z_1(t_{i-k}) \tag{11}$$

This equation can be solved using the *time marching* approach proposed by Tesche in [4]

$$V = Ri_g(t_i) + Ri_1(t_i) + \Delta t\sum_{k=0}^{i-1} i_1(t_k) z_1(t_{i-k}) + \Delta t i_1(t_i) z_1(t_0) \tag{12}$$

and $i_1(t_i)$ can be calculated as:

$$i_1(t_i) = \frac{V - Ri_g(t_i) - \Delta t\sum_{k=0}^{i-1} i_1(t_k)\, z_1(t_{i-k})}{\Delta t z_1(t_0) + R} \tag{13}$$

At times $t_{i=2(n+1)}$, where n is a positive integer, it can be assumed that $i_1(t_i) = i_1(t_{i-1})$, and $i_g(t)$ can be calculated:

If $v_g(t) < V_{th}$

$$i_g(t_i) = \frac{\Delta t\sum_{k=0}^{i} i_1(t_k)\, z_1(t_{i-k})}{R_{goff}} \tag{14}$$

If $v_g(t) > V_{th}$

$$i_g(t_i) = \Delta t\sum_{k=0}^{i} i_1(t_k)\, z_1(t_{i-k})\, k_0 \Delta t\sum_{k=0}^{i} i_g(t_k) \tag{15}$$

Equation (15) can be solved using:

$$i_g(t_i) = k_0 \Delta t\sum_{k=0}^{i} i_1(t_k)\, z_1(t_{i-k})\, \Delta t\left(\sum_{k=0}^{i-1} i_g(t_k) + i_g(t_i)\right) \tag{16}$$

$$i_g(t_i) = k_0 \Delta t\sum_{k=0}^{i} i_1(t_k)\, z_1(t_{i-k})\, \Delta t\sum_{k=0}^{i-1} i_g(t_k) + i_g(t_i)\, k_0 \Delta t\sum_{k=0}^{i} i_1(t_k)\, z_1(t_{i-k}) \tag{17}$$

$$i_g(t_i) = \frac{k_0 \Delta t^2 \sum_{k=0}^{i} i_1(t_k)\, z_1(t_{i-k}) \sum_{k=0}^{i-1} i_g(t_k)}{1 - k_0 \Delta t\sum_{k=0}^{i} i_1(t_k)\, z_1(t_{i-k})} \tag{18}$$

The procedure can be repeated iteratively.

SINGULARITIES INTRODUCED BY CAPACITIVE LOADS

If the load of the SWO, $Z_2(f)$, is an open circuit at $f=0$ (for example if the antenna is a dipole or a monopole), the impedance $Z_1(f)$ will also be singular at $f=0$. This will be proven in what follows.

The total ABCD parameters of the SWO (including only the RTL and the coaxial line) are calculated as the chain product of the ABCD parameters of multiple ABCD matrices:

$$\begin{bmatrix} A_{Total}(f) & B_{Total}(f) \\ C_{Total}(f) & D_{Total}(f) \end{bmatrix} = \left(\prod_{n=1}^{m} \begin{bmatrix} A_n(f) & B_n(f) \\ C_n(f) & D_n(f) \end{bmatrix} \right) \times \begin{bmatrix} A_{Coax}(f) & B_{Coax}(f) \\ C_{Coax}(f) & D_{Coax}(f) \end{bmatrix} \tag{19}$$

where $A_n(f)$, $B_n(f)$, $C_n(f)$, and $D_n(f)$ are the ABCD parameters of the *nth* segment of the RTL and $A_{Coax}(f)$, $B_{Coax}(f)$, $C_{Coax}(f)$, $D_{Coax}(f)$ are the ABCD parameters of the coaxial line.

By definition, the ABCD parameters of a lossless transmission line of length L and characteristic impedance Z_o are:

$$\begin{bmatrix} A(f) & B(f) \\ C(f) & D(f) \end{bmatrix} = \begin{bmatrix} \cosh(j\beta\Delta L) & Z_0 \sinh(j\beta\Delta L) \\ \dfrac{\sinh(j\beta\Delta L)}{Z_0} & \cosh(j\beta\Delta L) \end{bmatrix} \tag{20}$$

At frequency $f=0$:

$$\begin{bmatrix} A(0) & B(0) \\ C(0) & D(0) \end{bmatrix} = \begin{bmatrix} 1 & 0 \\ 0 & 1 \end{bmatrix} \tag{21}$$

And Equation (19) becomes:

$$\begin{bmatrix} A_{Total}(0) & B_{Total}(0) \\ C_{Total}(0) & D_{Total}(0) \end{bmatrix} = \begin{bmatrix} 1 & 0 \\ 0 & 1 \end{bmatrix} \tag{22}$$

From Equation (2) and knowing that $\lim_{f \to 0} Z_2(f) = \infty$, we have

$$\lim_{f \to 0} Z_1(f) = \lim_{f \to 0} \frac{A(f) + \dfrac{B(f)}{Z_2(f)}}{C(f) + \dfrac{D(f)}{Z_2(f)}} = \lim_{f \to 0} \frac{A(f)}{C(f)} = \infty \tag{23}$$

This singularity forbids the direct computation of the inverse Fourier transform of $Z_1(f)$. This discontinuity can be avoided using the following approach:

If the singularity is of the type $1/f$, we can express the input impedance as:

$$Z_1(f) = \frac{1}{j2\pi f} Z_{1A}(f) \tag{24}$$

leading to:

$$z_1(t) = \mathbb{F}^{-1}[Z_1(f)] = \mathbb{F}^{-1}\left[\frac{1}{j2\pi f} Z_{1A}(f)\right] \tag{25}$$

where $\mathbb{F}^{-1}[\ ]$ is the inverse Fourier transform operator

$$z_1(t) = \int_0^t \mathbb{F}^{-1}[Z_{1A}(f)]dt = \int_0^t z_{1A}(t)dt \tag{26}$$

Therefore, Equation (5) becomes:

$$V = Ri_1(t) + Ri_g(t) + i_1(t) * \int_0^t z_{1A}(t)dt \tag{27}$$

which can be transformed into:

$$V = Ri_1(t) + Ri_g(t) + \int_0^t i_1(t) * z_{1A}(t)dt \tag{28}$$

Taking the first derivative at both sides:

$$V\delta(t) = R\frac{di_1(t)}{dt} + R\frac{di_g(t)}{dt} + i_1(t) * z_{1A}(t) \tag{29}$$

Equation (6) becomes:

$$v_1(t) = v_g(t) \tag{30}$$

If $v_g(t) < V_{th}$ we have

$$\int_0^t (i_1(t) * z_{1A}(t))dt = i_g(t)R_{gOff} \tag{31}$$

If $v_g(t) > V_{th}$

$$\int_0^t (i_1(t) * z_{1A}(t))dt = k\frac{i_g(t)}{\int_0^t i_g(t)dt} \tag{32}$$

Equations (29), (30) can be solved iteratively, using the procedure presented in the previous section.

Using the discrete time definition for the convolution, Equation (29) becomes:

$$V\delta(t_i) = R\frac{\left(i_1(t_i) - i_1(t_{i-1})\right)}{\Delta t} + R\frac{\left(i_g(t_i) - i_g(t_{i-1})\right)}{\Delta t} + \Delta t\sum_{k=0}^{i} i_1(t_k) z_{1A}(t_{i-k}) \tag{33}$$

The convolution sum can be split to give

$$V\delta(t_i) = R\frac{\left(i_1(t_i) - i_1(t_{i-1})\right)}{\Delta t} + R\frac{\left(i_g(t_i) - i_g(t_{i-1})\right)}{\Delta t} + \Delta t\sum_{k=0}^{i-1} i_1(t_k) z_{1A}(t_{i-k}) + \Delta t i_1(t_i) z_{1A}(t_0) \tag{34}$$

Therefore, for times $t_{i=2n}$, the current $i_1(t)$ can be calculated as:

$$i_1(t_i) = \frac{V\delta(t_i) + R\frac{i_1(t_{i-1})}{\Delta t} - \Delta t\sum_{k=0}^{i-1} i_1(t_k) z_{1A}(t_{i-k}) - R_g\frac{\left(i_g(t_i) - i_g(t_{i-1})\right)}{\Delta t}}{\frac{R}{\Delta t} + \Delta t z_{1A}(t_0)} \tag{35}$$

For $i=2n$.

$$i_1(t_i) = i_1(t_{i-1}) \tag{36}$$

For $i=2n+1$

The current $i_g(t)$ can be calculated using:
If $v_g(t) < V_{th}$

$$i_g(t_i) = \frac{\Delta t^2\sum_{k=0}^{i} i_1(t_k) z_{1A}(t_{i-k})}{R_{gOff}} + i_g(t_{i-1}) \tag{37}$$

If $v_g(t) > V_{th}$

$$\int_0^t \left(i_1(t) * z_{1A}(t)\right)dt = k\frac{i_g(t_i)}{\int_{th}^{t_i} i_g(t)dt} \tag{38}$$

$$k\frac{i_g(t_i)}{\Delta t\sum_{n=h}^{i} i_g(t_n)} = \Delta t\sum_{j=0}^{i}\Delta t\sum_{k=0}^{j} i_1(t_k) z_{1A}(t_{j-k}) \tag{39}$$

$$k\frac{i_g(t_i)}{\Delta t\sum_{n=h}^{i-1} i_g(t_n) + \Delta t i_g(t_i)} = \Delta t\sum_{j=0}^{i}\Delta t\sum_{k=0}^{j} i_1(t_k) z_{1A}(t_{j-k}) \tag{40}$$

$$i_g(t_i) = \frac{\Delta t^3 \sum_{j=0}^{i} \left(\sum_{k=0}^{j} i_1(t_k) z_{1A}(t_{j-k}) \right) \sum_{n=h}^{i-1} i_g(t_n)}{k - \Delta t^3 \sum_{j=0}^{i} \sum_{k=0}^{j} i_1(t_k) z_{1A}(t_{j-k})} \tag{41}$$

Equations (35) and (41) can be solved for $i_1(t)$, from which $v_1(t)$ can be obtained. The output of the two-port network can be obtained either by convolving $v_1(t)$ with the time-domain transfer function of the SWO or by Fourier transforming $v_1(t)$ into the frequency domain

REFERENCES

[1] F. Santamaria, *et al.*, "Switched Oscillator: Parameter Effects on the Generated Signals," *Plasma Science, IEEE Transactions on*, vol. 40, pp. 3433-3441, 2012.

[2] T. G. Engel, *et al.*, "The pulsed discharge arc resistance and its functional behavior," *Plasma Science, IEEE Transactions on*, vol. 17, pp. 323-329, 1989.

[3] M. Toepler, "Zur Bestimmung der Funkenkonstante," *Archiv fur Elektrotechnik*, vol. XVIII, 1927.

[4] F. M. Tesche, "Development and Use of the BLT Equation in the Time Domain as Applied to a Coaxial Cable," *Electromagnetic Compatibility, IEEE Transactions on*, vol. 49, pp. 3-11, 2007.

Curriculum Vitae

Name : Jose Felix Vega Stavro
Born on February 22nd 1974
Email : felix.vega@gmail.com

Education

2013	Ph.D. in Electrical Engineering, Ecole Polytechnique Fédérale de Lausanne (EPFL), Switzerland
2003	M.Sc. Telecommunications. Universidad Distrital, Bogota Colombia
1998	B.Sc. in Electronics Engineering. Universidad Distrital, Bogota Colombia

Professional Experience

2004-present	Assistant professor, National University of Colombia, Bogota, Colombia
2011-2012	Consultant, Montena Technology, Rossens, Switzerland

Distinctions and Awards

2012	Best Applied Paper Award, Note Series 2010-2012, SUMMA Foundation
2011	Frank Gunther Award, Radio Club of America (RCA)
2008	Young Scientist Award, URSI
2007	Best presentation award, International course on High Power Electromagnetics, SUMMA Foundation
2007-2009:	Swiss Confederation Scholarship for Foreign Students

Publications:

Journal Papers

- 2013. F. Vega., F. Rachidi, D. Giri. "A New Set of Electrodes for the Coaxial Quarter Wave Switched Oscillator." Transactions on Plasma Science (Submitted)
- 2013. F. Vega, F. Rachidi, N. Mora, N. Pena and F. Roman. Design, Realization, and Experimental Test of a Coaxial Exponential Transmission Line Adaptor for a Half-Impulse Radiating Antenna, IEEE Transactions on Plasma Science, vol. 41, num. 1, p. 173-181, 2013.
- 2013. F. Vega, F. Rachidi, N. Mora, B. Daout and N. Peña et al. A Method for the Analysis and Design of Switched Oscillators using Chain Parameters, in Sensor and Simulation Notes, num. SSN 561, 2013.
- 2012. A. Shoory, F. Vega, P. Yutthagowith, F. Rachidi and M. Rubinstein et al. On the Mechanism of Current Pulse Propagation Along Conical Structures: Application to Tall Towers Struck by Lightning, IEEE Transactions on Electromagnetic Compatibility, vol. 54, num. 2, p. 332-342, 2012.
- 2013. Pantoja, J. J, Pena N, Rachidi F, Mora N, Vega F, Roman, F. "On the Electromagnetic Susceptibility of Hot Wire-Based Electro-explosive Devices to RF Sources.", IEEE Transactions on Electromagnetic Compatibility, in press, 2013.

Book Chapters :

- 2013. Vega, F., F. Rachidi, N. Pena. F. Roman "A New Set of Electrodes for the Coaxial Quarter Wave Switched Oscillator based on the Logarithmic-Tangent transformation." Ultra-Wideband, Short Pulse Electromagnetics 10 (Accepted). Springer.
- 2013. Daout, B. and F. Vega. SF6 for High Voltage Pulse Generators an Ecological Analysis. Ultra-Wideband, Short Pulse Electromagnetics 10 (Accepted). Springer

Conference Papers

- 2013. Vega, F., N. Mora, F. Rachidi, N. Pena. F. Roman. Design of a Switched Oscillator for IEMI Susceptibility Testing. IEEE EMC Symposium Denver, USA. (Accepted)
- 2011. Vega, F., F. Rachidi, et al. Design and optimization of mesoband radiators using chain parameters. Electromagnetics in Advanced Applications (ICEAA), 2011 International Conference on.
- 2010. F. Vega, N. Mora, F. Rachidi, N. Peña and F. Roman. Design, Construction and Test of a Half Impulse Radiating Antenna (HIRA).Canada. . 2010 American Electromagnetics International Symposium AMEREM, Ottawa, Canada, July 5-9, 2010.
- 2009. Vega, F., F. Rachidi, et al. Design and Simulation of an Electromagnetic Lens for a Half Impulse Radiating Antenna. International Conference on Electromagnetics in Advanced Applications, Torino, Italy.
- 2009. N. Mora, F. Vega, F. Roman, N. Peña and F. Rachidi. Corona Charged subnanosecond impulse generator. Proceedings of the 20th International Zurich Symposium on Electromagnetic Compatibility, Zurich, Switzerland, January 12-16, 2009.
- 2009. N. Mora, F. Vega, F. Roman, N. Peña and F. Rachidi. Corona Charged subnanosecond impulse generator. Proceedings of the 20th International Zurich Symposium on Electromagnetic Compatibility, Zurich, Switzerland, January 12-16, 2009.
- 2008. F. Vega, F. Rachidi, N. Pena and F. Roman. A Design of a Mesoband High Power Electromagnetic Radiator Using a Switched Oscillator and a Corona Current Generator. 2008 URSI General Assembly, Chicago, USA, August 2008.